



# UNIVERSITÀ DEGLI STUDI DI MILANO

Facoltà di Scienze e Tecnologie  
Laurea Triennale in Fisica

## Optimisation of the event selection for the single top quark production in association with a $Z$ boson at the ATLAS detector

Relatore:

**Dott.ssa Lidia Dell'Asta**

Correlatore:

**Prof. Marcello Fanti**

Tesi di Laurea Triennale di:

**Alberto Plebani**

**Matricola: 931621**

Codice PACS: 14.65.-q

Anno Accademico 2020/2021



## Abstract

The unprecedented amount of data collected by the ATLAS Experiment at the Large Hadron Collider at CERN has made it possible to measure rare processes, foreseen by the Standard Model (SM), that have never been observed before. The study of the top quark is of primary importance for the ATLAS physics program. Being the heaviest particle of the SM, with a coupling to the Higgs boson close to one, the top quark can help shedding light over the electroweak symmetry breaking mechanism. The production of a single top quark in association with a Z boson ( $tZq$ ) has recently been observed by the ATLAS Experiment. The cross section of this process, predicted by the SM to be 102 fb, has been measured with an uncertainty of 15%. In this thesis, the proton-proton collision data collected by the ATLAS Experiment during Run2 will be analysed to improve the measurement of the  $tZq$  cross-section. In particular, the aim is to refine the selection of the events to enhance the signal acceptance and to improve the rejection of the backgrounds by using the most recent object reconstruction algorithms available. In the first two chapters I am going to give a brief description of the Standard Model and the top quark physics. In the third chapter I will describe how the ATLAS Experiment works. In the fourth chapter I will present my optimisation studies and their results.



# Contents

<b>1</b>	<b>The Standard Model</b>	<b>1</b>
1.1	The structure of the Standard Model . . . . .	1
1.2	Fundamental interactions . . . . .	3
1.2.1	Electromagnetism . . . . .	3
1.2.2	Weak interaction . . . . .	3
1.2.3	Electroweak unification . . . . .	5
1.2.4	Strong nuclear interaction . . . . .	5
1.3	The Lagrangian of the Standard Model . . . . .	6
1.4	The Higgs Mechanism . . . . .	7
1.5	The proton . . . . .	9
1.6	Beyond the Standard Model . . . . .	10
<b>2</b>	<b>Top Quark physics</b>	<b>13</b>
2.1	Top quark properties and decay . . . . .	13
2.2	Top quark production at the LHC . . . . .	14
2.2.1	Pair production . . . . .	14
2.2.2	Single top production . . . . .	15
2.2.3	Top quark and $Z$ boson associated productions . . . . .	15
2.2.4	$tZq$ . . . . .	16
<b>3</b>	<b>LHC and the ATLAS Experiment</b>	<b>19</b>
3.1	The Large Hadron Collider . . . . .	19
3.1.1	Properties . . . . .	20
3.2	The ATLAS experiment . . . . .	22
3.2.1	The magnets . . . . .	24
3.2.2	The Inner Detector . . . . .	25
3.2.3	The calorimeter system . . . . .	27
3.2.4	The Muon Spectrometer . . . . .	28
3.2.5	Trigger system . . . . .	29
3.2.6	Forward detectors . . . . .	30

<b>4 Optimisation of the event selection for tZq</b>	<b>31</b>
4.1 Data Samples . . . . .	31
4.2 Monte Carlo samples . . . . .	32
4.2.1 Signal sample . . . . .	32
4.2.2 Background samples . . . . .	33
4.3 Object reconstruction . . . . .	36
4.4 Event selection . . . . .	42
4.5 State of the art . . . . .	42
4.6 Event selection optimisation . . . . .	43
4.6.1 Lepton isolation requirements . . . . .	44
4.6.2 Lepton $p_T$ requirements . . . . .	55
4.6.3 $b$ -tagging analysis . . . . .	65
4.6.4 High jet multiplicity signal region . . . . .	69
4.7 Conclusions . . . . .	71
4.8 Data . . . . .	72
<b>5 Summary and conclusions</b>	<b>77</b>
<b>A Description of Monte Carlo datasets</b>	<b>79</b>

# Chapter 1

## The Standard Model

The Standard Model (SM) is a quantum-relativistic theory for the elementary particles. It describes three of the four fundamental interactions, which are the electromagnetic, the strong nuclear and the weak nuclear. The fourth, gravity, is still not included in the Standard Model.

### 1.1 The structure of the Standard Model

The Standard Model is a gauge theory built on a  $U(1) \times SU(2) \times SU(3)$  symmetry. The  $U(1)$  symmetry refers to *hypercharge*,  $SU(2)$  is the *weak isospin* symmetry while  $SU(3)$  is the *colour charge* symmetry. In the SM for high energies the weak nuclear interaction and the electromagnetic interaction are unified into the electroweak interaction, with a  $U(1) \times SU(2)$  symmetry. Due to the Higgs Mechanism, the electroweak symmetry is spontaneously broken. Therefore, three gauge fields  $W^+$ ,  $W^-$  and  $Z$  acquire mass while the  $A$  field, describing the photon, remains massless.

The elementary particles described in the SM are represented in Figure 1.1. There are two types of particles, *fermions* and *bosons*. Fermions have half-integer spin (in the SM  $S = 1/2$ ) and obey Fermi-Dirac statistics, so two identical fermions have an anti-symmetric wavefunction. Bosons instead have integer spin (in the SM  $S = 0, 1$ ) and obey Bose-Einstein statistics, resulting in two identical bosons having a symmetric wavefunction.

Fermions in the SM appear as leptons and quarks. Leptons are grouped into three families, each containing a negatively (-1 in unity of the electric charge) charged massive particle and its corresponding neutral neutrino. The three families are the electron family ( $e$  and  $\nu_e$ ), the muon family ( $\mu$  and  $\nu_\mu$ ) and the tau family ( $\tau$  and  $\nu_\tau$ ). In each family the left-handed chiral component is a weak isospin doublet differing only in their masses [1]. Quarks are also grouped in three families according to mass eigenstates. The three families are the up family (up, down), the charm family (charm, strange) and the top family (top, bottom). They have fractional charge (2/3 for u,c and t and -1/3 for d,s and b) and very different values of masses [1], with the up quark

being the lightest ( $m_u \simeq 2$  MeV) and the top quark being the heaviest ( $m_t \simeq 173$  GeV). All the quarks have baryon number  $B = 1/3$ , that is it takes three quarks to form a baryon and a quark-antiquark pair to form a meson. The leptons instead have baryon number  $B = 0$ , but they have lepton number  $L = 1$ . Each lepton family also has a flavour number (1 for the particle and  $-1$  for the antiparticle), which is conserved in all interactions except for neutrino oscillations. Each fermion in the SM has a corresponding anti-fermion with the same mass but opposite quantum numbers.

The bosons in the SM are the interaction carriers and the Higgs boson. The force carriers are vector bosons with spin  $S = 1$ , while the Higgs boson is the only scalar in the SM, having spin  $S = 0$ . We can divide the force carriers by which interaction they carry: the photon for the electromagnetic interaction, the gluon for the strong interaction and the  $W$  and  $Z$  bosons for the weak interaction. The  $W$  and  $Z$  bosons have mass [1] because the electroweak symmetry is spontaneously broken by the Higgs Mechanism [2]. The photon and the gluon are massless because the Higgs field does not interact with electric charge and colour. The  $Z$  boson has a mass  $m_Z = 91$  GeV [1] and a neutral charge. The  $W$  boson is responsible for the charged weak current. It exists in two different charged states ( $\pm 1$ ), one being the anti-boson of the other. Its mass is  $m_W = 80$  GeV [1].

Finally, the Higgs boson is the scalar responsible for the masses of the particles through the mechanism of spontaneous breaking of the symmetry. The  $U(1) \times SU(2) \times SU(3)$  symmetry is preserved, whereas the vacuum loses its symmetry due to the Higgs mechanism. The Higgs boson mass is  $m_H = 125$  GeV [1] and it is the newest member of the SM, discovered only in 2012 at LHC independently by the ATLAS experiment [3] and the CMS experiment [4], almost 50 years after it was theorized.

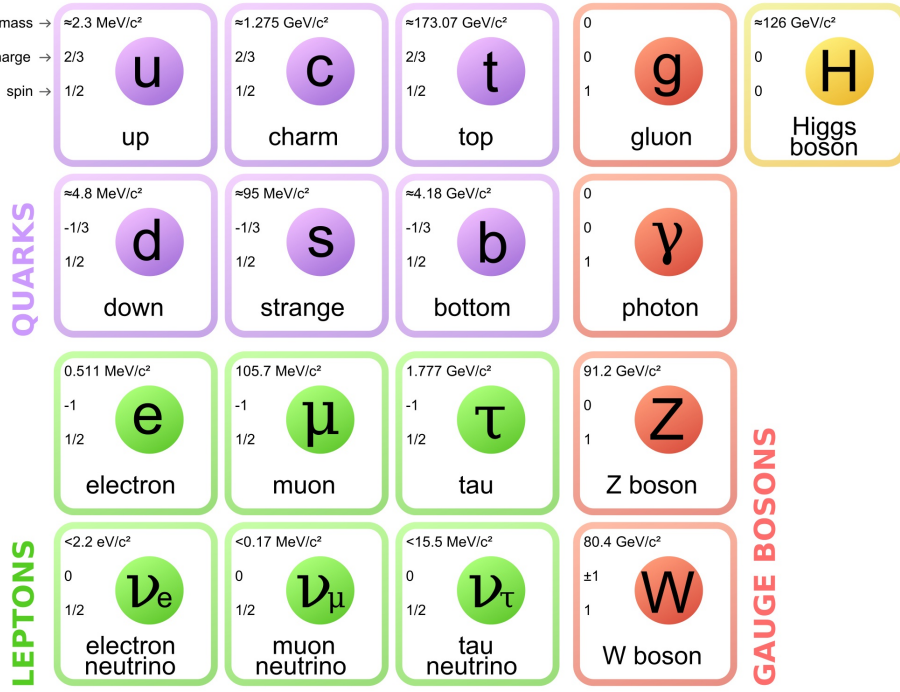


Figure 1.1: Scheme of the elementary particles described by the SM of particle physics with information regarding the mass, the charge and the spin of each particle.

## 1.2 Fundamental interactions

### 1.2.1 Electromagnetism

Electromagnetism is the interaction between charged particles. It is described by Maxwell equations, which can be written as in Equation (1.2.1) and it is represented by means of Feynman diagrams. The carrier is the photon  $\gamma$ , and the range of interaction is infinite, as can be easily calculated using Equation (1.2.2) because  $m_\gamma = 0$ .

$$\partial_\nu F^{\nu\mu} = J^\mu \quad (1.2.1)$$

$$R = \frac{\hbar}{mc} \quad (1.2.2)$$

Because of the photon being massless, the Yukawa potential of the electromagnetic field is  $\phi = \frac{\eta}{4\pi r}$ , with  $\eta = 4\pi\alpha \simeq 0.09$  ( $\alpha$  is the fine structure constant,  $\simeq 1/137$ ).

All the quarks and the charged leptons feel the effects of the electromagnetic field.

### 1.2.2 Weak interaction

The weak interaction is the interaction acting on all the doublets of particles in the SM. It's been observed that Parity, Charge conjugation (both violations observed by Wu [5]) and CP (Parity and Charge conjugation, observed with kaons oscillations

[6]) are violated. Therefore, the weak theory isn't left-right symmetric. By using Equation (1.2.2) to evaluate the range, knowing the masses of the carriers ( $W$  and  $Z$  bosons) from Figure 1.1, we get a range  $R \simeq 2 \cdot 10^{-3}$  fm.

The  $Z$  boson is responsible for neutral currents. So far, flavour changing neutral currents (FCNC) have not been detected at tree-level, so we can say that the  $Z$  boson interacts at Leading Order (LO) only with same type fermions. Therefore, the interaction between an anti-muon and an electron cannot be mediated by a  $Z$  boson, which can mediate interactions between, for example, an electron and a positron. The  $W$  boson instead is responsible for flavour changing charged currents. When acting on leptons, the  $W$  boson interacts only inside the family. Instead, when acting on quarks the  $W$  boson interacts also outside the mass-eigenstates family defined in Section 1.1. That is because the eigenstates of the weak interaction (Equation (1.2.3)) are different from the mass eigenstates (Equation (1.2.4))

$$\begin{pmatrix} u \\ d \end{pmatrix} \begin{pmatrix} c \\ s \end{pmatrix} \begin{pmatrix} t \\ b \end{pmatrix} \quad (1.2.3)$$

$$\begin{pmatrix} u \\ d' \end{pmatrix} \begin{pmatrix} c \\ s' \end{pmatrix} \begin{pmatrix} t \\ b' \end{pmatrix} \quad (1.2.4)$$

The  $d'$ ,  $s'$  and  $b'$  quarks are linear combinations of the  $d$ ,  $s$  and  $b$  quarks, with the Cabibbo-Kobayashi-Maskawa (CKM [7]) matrix being the mixing matrix between the two different sets of eigenstates, as can be seen in Equation (1.2.5)

$$\begin{pmatrix} d' \\ s' \\ b' \end{pmatrix} = \begin{pmatrix} V_{ud} & V_{us} & V_{ub} \\ V_{cd} & V_{cs} & V_{cb} \\ V_{td} & V_{ts} & V_{tb} \end{pmatrix} \begin{pmatrix} d \\ s \\ b \end{pmatrix} \quad (1.2.5)$$

A few things that should be said regarding the CKM matrix. The matrix is a unitary matrix, with the diagonal elements being the largest ( $V_{ud} \simeq 0.97$ ,  $V_{cs} \simeq 0.97$ ,  $V_{tb} \simeq 0.99$ ). These values are taken from Wolfenstein's parametrization of the CKM matrix [8]). That is because even though it's true that the up quark interacts with  $d'$  and not  $d$ , the probability of interacting with  $d$  is larger than the probability (which is proportional to  $|V_{ij}|^2$ ) of interacting with, for example,  $s$  ( $V_{us} \simeq 0.23$ ). In the flavour set of eigenstates (Equation (1.2.4)) the  $W$  boson acts only inside a family, and the weak interaction is diagonal. Thus, we can preserve the universality of the weak interaction because the coupling constants with the  $W$  boson for the families of both leptons and quarks are the same. Also, because of the CKM being a unitary  $3 \times 3$  matrix, it is described by four parameters, of which three are the angles between the family and one is a complex phase. In order to have CP violation, a complex phase is required, and the CKM matrix shows that in the weak interaction a complex phase is present in the mixing matrix, thus explaining the CP violation.

### 1.2.3 Electroweak unification

The propagator of the electromagnetic field, i.e., the Fourier transform of Yukawa's potential, depends only on the inverse square value of the transferred momentum  $\vec{q}$ ,  $f(q) \sim 1/q^2$ . The propagator of the weak nuclear field is proportional to the inverse value of  $q^2 - m^2$ , where  $m$  is the mass of the interaction carrier, either a  $W$  or a  $Z$  boson. It can be easily noted that if  $q^2 \gg m^2$ , the two propagators are the same. Therefore, we don't distinguish between the two interactions, and we say that there is only one interaction, the electroweak one. It is based on a  $SU(2) \times U(1)$  symmetry, and the conserved quantity is the electric charge  $Q$ , linked to the third component of the weak isospin  $I_3(SU(2))$  and the hypercharge  $Y(U(1))$  as stated by the Gell-Mann Nishijima [9] formula (Equation (1.2.6))

$$Q = \frac{Y}{2} + I_3 \quad (1.2.6)$$

The fermions in the electroweak Lagrangian appear as left-handed spinors in doublets and, if they have mass, right-handed singlets, as can be seen in Equation (1.2.7)

$$\begin{pmatrix} \nu_e \\ e \end{pmatrix}_L, \begin{pmatrix} \nu_\mu \\ \mu \end{pmatrix}_L, \begin{pmatrix} \nu_\tau \\ \tau \end{pmatrix}_L, \begin{pmatrix} u \\ d' \end{pmatrix}_L, \begin{pmatrix} c \\ s' \end{pmatrix}_L, \begin{pmatrix} t \\ b' \end{pmatrix}_L; e_R, \mu_R, \tau_R, u_R, c_R, t_R, d'_R, s'_R, b'_R \quad (1.2.7)$$

The Lagrangian has a pure weakly component, which is the component of the charged currents mediated by the  $W$  boson, a pure electromagnetic component, mediated by the photon, and a mixed electroweak component, mediated by  $Z^0$ .

The electroweak symmetry is spontaneously broken by the Higgs Mechanism, which I will be explaining in Section 1.4.

### 1.2.4 Strong nuclear interaction

The strong interaction is, as the name states, the strongest interaction. It acts only on quarks, and its carrier is the gluon, a massless neutral vector boson having colour charge. The colour charge has the same purpose as the electric charge has for the electromagnetic interaction, in that the strong interaction is the interaction between particles having colour charge. There are three different colour states (red, green and blue), so the symmetry is  $SU(3)$ , generated by the eight Gell-Mann matrices. That means that every one of the quarks in the Standard Model can appear in three different states. The non elementary particles, like baryons and mesons, are colourless, because there is a combination of the three colours that generate the colour "white", which is the total antisymmetric combination  $\frac{1}{\sqrt{6}}(rgb + brg + gbr - grb - rbg - brg)$ .

There are eight different gluons (Equation (1.2.8)), each one of them having a colour charge.

$$r\bar{g}, g\bar{r}, r\bar{b}, b\bar{r}, g\bar{b}, b\bar{g}, 1/\sqrt{2}(r\bar{r} - g\bar{g}), 1/2(r\bar{r} + g\bar{g} - 2b\bar{b}) \quad (1.2.8)$$

The big difference between the colour charge and the electric charge is that the gluon has colour, whereas the photon doesn't have electric charge. This means that interactions between gluons are possible, while interactions between photons are suppressed in the first order of QED theory.

### 1.3 The Lagrangian of the Standard Model

The equation describing the motion of a spinor is Dirac equation (Equation (1.3.1))

$$(i\gamma^\mu \partial_\mu - m) \psi = 0 \quad (1.3.1)$$

Where  $\psi$  is a four-component spinor, and the gammas are Dirac matrices<sup>1</sup> [10].

The free Dirac Lagrangian is then

$$L = i\bar{\psi}\gamma^\mu \partial_\mu \psi \quad (1.3.2)$$

It can be noted that there is not a mass term in the Lagrangian, and that is because the Lagrangian isn't left-right symmetric, because only left-handed or right-handed spinors are present, and a mass term would appear as  $\bar{\psi}m\psi$ , which would be left-right symmetric. The mass terms are introduced by means of the Higgs Mechanism.

The other terms in the Lagrangian are the interactions with the fields, interactions generated when a gauge invariance is required, and the free field. The strong nuclear field, because of the gluons carrying a colour charge, has also a self-interacting term, which is the term of gluons interacting with other gluons.

The complete SM Lagrangian can be written as in Equation (1.3.3)

$$\begin{aligned} \mathcal{L} = & \bar{R}_\ell i\gamma^\mu \left( \partial_\mu + i\frac{g'}{2} B_\mu Y \right) R_\ell + \bar{L}_\ell i\gamma^\mu \left( \partial_\mu + i\frac{g'}{2} B_\mu Y + i\frac{g}{2} \vec{\sigma} \cdot \vec{W}_\mu \right) L_\ell + \\ & + \bar{R}_q i\gamma^\mu \left( \partial_\mu + i\frac{g'}{2} B_\mu Y + i\frac{g_s}{2} G_\mu^k \lambda_k \right) R_q + \\ & + \bar{L}_q i\gamma^\mu \left( \partial_\mu + i\frac{g'}{2} B_\mu Y + i\frac{g}{2} \vec{\sigma} \cdot \vec{W}_\mu + i\frac{g_s}{2} G_\mu^k \lambda_k \right) L_q + \\ & - \frac{1}{4} W_{\ell\mu\nu} W^{\ell\mu\nu} - \frac{1}{4} B_{\mu\nu} B^{\mu\nu} - \frac{1}{4} G_{k\mu\nu} G^{k\mu\nu} \end{aligned} \quad (1.3.3)$$

$R_\ell$  is the right-handed singlets for leptons (only electrons, muons and taus because this Lagrangian (Equation (1.3.3)) is written for massless neutrinos, which have only a left-handed component), which interacts only with the hypercharge current  $B_\mu Y$  with a coupling constant  $g'$ .  $L_\ell$  is the left-handed spinor for the doublets of leptons (each doublet is  $(\nu_l, l)$  with  $l = e, \mu, \tau$ ). The left-handed leptons interact with the hypercharge

---

<sup>1</sup>

$\gamma^0 = \begin{pmatrix} \mathbb{I}_{2 \times 2} & 0_{2 \times 2} \\ 0_{2 \times 2} & -\mathbb{I}_{2 \times 2} \end{pmatrix}$ ,  $\gamma^i = \begin{pmatrix} 0_{2 \times 2} & \sigma_i \\ -\sigma_i & 0_{2 \times 2} \end{pmatrix}$

current, same as the right-handed ones, and also with the weak isospin current ( $\vec{\sigma}$  are the three Pauli matrices and  $\vec{W}_\mu$  is the electroweak potential) with a coupling constant  $g$ . For the quarks we have two different terms as well. The right-handed one is the singlet term for the six quarks in their mass eigenstates (so  $u_R, d_R, c_R, s_R, t_R, b_R$ ). They don't interact with the weak isospin current, which acts only on the doublets, and interact with the colour current ( $\lambda_k$  are the eight Gell-Mann matrices,  $k = 1, \dots, 8$ ;  $G_\mu^k$  is the gluon field) with a coupling constant  $g_s$ . The left-handed terms refer to the left-handed doublets of quarks, as in Equation (1.2.4), which interacts with all the three currents. Every term has also a free massless Dirac Lagrangian.

We then have the three free fields, given by  $B_{\mu\nu}$ ,  $W_{\ell\mu\nu}$  and  $G_{k\mu\nu}$ . They are defined as linear combinations of space-time derivatives of  $B_\mu$ ,  $W_{\ell\mu}$  and  $G_{k\mu}$ , describing the free propagation, and for  $W_{\ell\mu\nu}$  and  $G_{k\mu\nu}$  they also contain self-interacting terms.

## 1.4 The Higgs Mechanism

There is still one particle in the SM that did not appear yet in the Lagrangian written in Equation (1.3.3), the Higgs boson. The Higgs boson is the scalar term, responsible for the masses of the fermions and the masses of the  $W$  and  $Z$  bosons, by means of the spontaneous symmetry breaking. The Higgs boson doesn't satisfy Dirac equation (Equation (1.3.1)), which only works for fermions, but it satisfies Klein Gordon equation (Equation (1.4.1)).

$$(\partial_\mu \partial^\mu + m^2) \phi = 0 \quad (1.4.1)$$

The free Klein-Gordon Lagrangian is then written as in Equation (1.4.2)

$$\mathcal{L}_{free} = \frac{1}{2} \partial_\mu \phi \partial^\mu \phi - \frac{1}{2} m^2 \phi^2 \quad (1.4.2)$$

The Higgs potential is written in Equation (1.4.3), and the Lagrangian is written in Equation (1.4.4)

$$V = -\frac{1}{2} \mu^2 |\phi|^2 + \frac{1}{4} \lambda^2 |\phi|^4 \quad (1.4.3)$$

$$\mathcal{L} = \frac{1}{2} \partial_\mu \phi \partial^\mu \phi + \frac{1}{2} \mu^2 \phi^2 - \frac{1}{4} \lambda^2 \phi^4 \quad (1.4.4)$$

If  $-\mu^2 < 0$ , the potential has two different minima, at  $\phi = \pm \frac{\mu}{\lambda}$ . The potential is represented in Figure 1.2, and we can see that if the energy is high, the potential is symmetric, whereas if the energy is low we lose the symmetry. That means that even though the potential  $V$  is symmetric, the ground state isn't, because there are two possible "wells" where the system can evolve into. We then substitute  $\eta = \phi \pm \frac{\mu}{\lambda}$ , and expand around the minima  $\eta = 0$ . The Lagrangian (Equation (1.4.4)) then turns into (Equation (1.4.5)).

$$\mathcal{L} = \frac{1}{2} \partial_\mu \eta \partial^\mu \eta - \mu^2 \eta^2 \pm \mu \lambda \eta^3 - \frac{1}{4} \lambda^2 \eta^4 \quad (1.4.5)$$

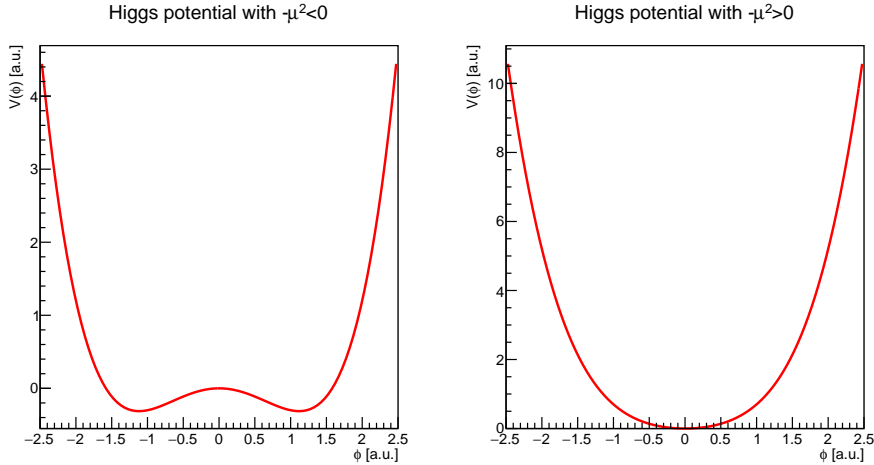


Figure 1.2: Higgs potential for  $-\mu^2 < 0$  and for  $-\mu^2 > 0$ . We can see how the spontaneous symmetry breaking occurs only for the first scenario

We can see that a new term  $-\mu^2\eta^2$  is introduced. This term is responsible for the mass, because if we apply Euler-Lagrange equation on this Lagrangian (Equation (1.4.5)) we get Klein-Gordon equation (Equation (1.4.1)), with the mass  $m$  being  $m = \sqrt{2}\mu$ . This is the mass term referring to the Higgs boson mass.

The Lagrangian in Equation (1.4.4) is not invariant under local phase transformation, necessary in order to preserve gauge invariance. Gauge invariance is preserved by changing the derivative term  $\partial_\mu$  in Equation (1.4.4) into a covariant derivative, so that  $\partial_\mu$  is substituted by  $\partial_\mu + i\frac{q}{hc}A_\mu$ . It can be noted that this new term, when applied on the scalar boson  $\phi$ , introduces an interaction between the field and the Higgs boson. An interaction with a field means that the free field term must be introduced in the Lagrangian. When expanding around one of the two minima of the Higgs field, we get that the scalar  $\phi$  is modified as  $\phi + v$ , where  $v$  is the *vacuum expectation value* (V.E.V.), which is the value of the field in vacuum. So, we have a coupling between the gauge field and the V.E.V. and a coupling between gauge field and the Higgs boson.

The vacuum coupling is the term which generates the masses of the vector bosons. Because the vacuum is neutrally charged and colourless, the photon and the gluon don't interact with it, so they remain massless. On the contrary, the  $W$  and  $Z$  boson interact with vacuum because vacuum has isospin  $I = 1/2$  and hypercharge  $Y = 1$ .

The coupling between the bosons and the Higgs potential is a term proportional to the mass squared of the bosons (those who gain mass by interacting with vacuum), in a term  $g_V = \frac{2m_V^2}{v}$ .

For fermions, there is a new term in the Lagrangian, the Yukawa coupling, which explains their masses. The Yukawa term has interactions with vacuum, which, same as for bosons, gives masses to the particles, and interaction with the Higgs boson, which gives the coupling constant  $g_f = \frac{m_f}{v}$ , proportional to the mass of the fermions.

In the end, we have:

- Two massive charged vector bosons ( $W^\pm$ )
- A massless vector boson ( $\gamma$ )
- A massive neutral vector boson ( $Z$ )
- A massive neutral scalar boson (the Higgs boson,  $H$ )
- 6 massive charged quarks
- 3 massive charged leptons
- 3 massive neutral neutrinos

Because of the coupling constant for fermion being proportional to the mass of the fermion, the top quark, being the heaviest particle in the SM, is the particle which interacts the most with Higgs boson. In Figure 1.3 a scheme of the interactions between the fermions and the vector bosons with the Higgs boson is represented.

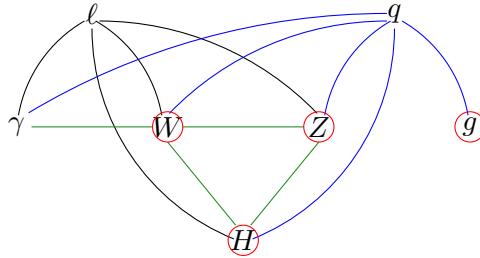


Figure 1.3: A scheme representing the interactions between the particles in the Standard Model. The black lines represent the interactions for the leptons, the blue lines represent the interactions for the quarks, the green lines represent the interactions between the bosons and the red circles represent the self-interactions.

## 1.5 The proton

The proton is a non-elementary fermion of spin  $S = 1/2$ , that is a particle made of other particles, in particular quarks and gluons. It is a baryon with mass  $m_P = 938$  MeV and charge  $Q_P = +1$ . Before the parton model [11], the proton was considered to be made of three quarks, precisely  $u, u, d$ . This model explained the baryon number ( $B = 1$ , because each quark has  $B = 1/3$ ) and the charge ( $Q = 1 = 2/3 + 2/3 - 1/3$ ). What wasn't yet explained was the scaling phenomena in the cross section for electron-proton scattering [12], that is, a high cross section for  $ep$  scattering even at large transferred momentum. It was theorized that the scaling was caused by the electrons interacting with the quarks inside the proton, and it was observed that the cross section could be expressed in terms of elementary cross section between electrons and quarks,

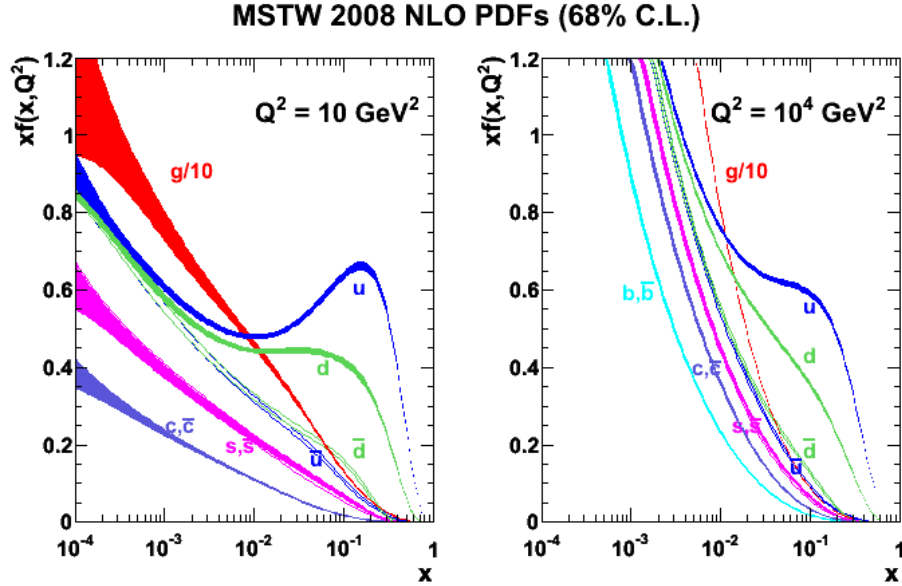


Figure 1.4: Parton distribution function of the proton, represented as a function of the transferred momentum  $Q^2$  [14].

with every quark weighted with its own probability density. It was also noted that the momentum carried by all the quarks was about half of the momentum of the proton. The other half of the momentum was carried by gluons, which are the biggest component inside a proton. Figure 1.4 represents the so-called Parton Distribution Functions (PDFs [13]), which give the probability to find a specific quark or gluon as a function of the fraction of the proton's momentum carried by the quark. Saying that the proton has two *up* quarks is wrong, but it does make sense to do so, because inside a proton,  $\int dx (f_u(x) - f_{\bar{u}}(x)) = 2$ , where  $f(x)$  is the probability of finding a quark with a fraction  $x$  of the proton's momentum. This result means that the valence quarks inside a proton are  $u, u, d$ , as predicted without using the Parton Model. An interesting remark about the Parton Distribution Functions is that the PDFs are scale-dependent objects. This implies that the proton structure depends on the energy of the incoming particle. Therefore, at low energy we see the proton being made only of  $u, u, d$ , but at high energy we start seeing gluons,  $\bar{u}$  and all the other quarks.

## 1.6 Beyond the Standard Model

The Standard Model is a theory that successfully describes the particle physics processes, and its predictions have been confirmed with very high precision with the various particle accelerators spread all over the world. However, there are still some observations that the Standard Model does not explain:

## Dark Matter

We know from cosmological observations that only 4% of the matter in the Universe is baryonic matter. The remaining 96% is made of Dark Energy and Dark Matter (27%). Whereas baryonic matter is explained in the Standard Model, Dark Matter isn't, and neither are the interactions between Dark and baryonic Matter. Dark Matter candidates are the so-called WIMPs (Weakly interacting massive particles), particles that interact gravitationally but not electromagnetically. Many experiments are now active in search for the existence of Dark Matter (for example DAMA/LIBRA and DarkSide), but so far there is no clear consensus about the observation of WIMPs.

## Neutrino oscillations

In the Standard Model neutrinos are considered massless particles, thus explaining why they do not appear with a singlet right-handed component in the Lagrangian. By studying the solar neutrinos, neutrino oscillations have been observed [15]. Yet, in order to oscillate, the neutrino must be a massive particle. An additional issue caused by the neutrino oscillation is the violation of leptonic flavour, because if a  $\nu_e$  oscillates into a  $\nu_\mu$ , the electronic number and the muonic number are not conserved. On the contrary, the Standard Model requires a conservation of each leptonic flavour separately.

## Gravitational interaction

The gravitational interaction is not included in the Standard Model. It has been theorized that, in case it were possible to have a quantum theory for the gravitational interaction, the interaction carrier of the field would be the graviton, a boson of spin  $S = 2$ , which yet has not been discovered.

Beyond Standard Model (BSM) theories nowadays include Supersymmetry (SUSY), a theory that would preserve the  $SU(3) \times U(1) \times SU(2)$  symmetry, but so far there are no experimental evidence sustaining this theory.



## Chapter 2

# Top Quark physics

The *top* quark was theorized in order to complete the weak isospin doublet with the *bottom* quark, and it was discovered in 1995 at the Fermilab Tevatron [16, 17]. It is a very peculiar particle, because it is heavier than the Higgs boson and it has a mass close to the scale of the electroweak symmetry breaking, which implies a near-unity coupling with the Higgs boson. It is also the only elementary fermion heavier than the  $Z$  and  $W$  bosons, thus allowing it to decay into a real boson and not a virtual one, as it is the case for the other quarks and leptons. That is the reason for the *top* quark having no bound states, because it can decay in a very short time (See Section 2.1) The *top* quark does not bind with other quarks to form hadrons, and that is the reason why we do not observe the *top quarkonium*, that is, the meson  $t\bar{t}$ , or other mesons or baryons with the *top* quark. This is peculiar only of the *top* quark, because the other heavy quarks (*charm* and *bottom*) form a quarkonium: the  $J/\psi$  [18] ( $c\bar{c}$ ) meson, observed in 1974 at SLAC by B. Richter [19] and by S. Ting [20] at BNL, and the  $\Upsilon$  [21] ( $b\bar{b}$ ) meson, discovered in 1977 at Fermilab by L.Lederman [22].

### 2.1 Top quark properties and decay

The *top* quark is the heaviest particle in the Standard Model, having a mass of  $m_t = 172.4 \text{ GeV} \pm 0.7 \text{ GeV}$  [1]. It has an electric charge  $Q_t = 2/3$ . In the SM it appears in a left-handed doublet of isospin  $1/2$ , with  $I_3 = +1/2$ , together with the quark *bottom*, and in a right-handed singlet. Because of the CPT theorem [23], the anti-quark  $\bar{t}$  has same mass,  $I_3 = -1/2$ ,  $Q = -2/3$  and same decay time.

The *top* quark has almost null mixing matrix elements with the other two families, with  $V_{td}$  and  $V_{ts}$  (Equation (1.2.5)) being close to zero, precisely  $|V_{td}|^2 \simeq 7.6 \times 10^{-5}$  and  $|V_{ts}|^2 \simeq 1.7 \times 10^{-3}$  [8]. The last remaining matrix element is  $V_{tb}$ , which is close to unity. Therefore the *top* quark interacts almost exclusively with the *bottom* quark.

The *top* quark decays as in Equation (2.1.1) with a branching fraction close to 1

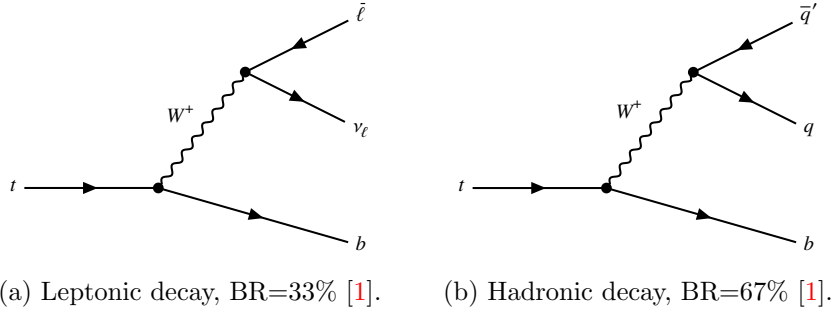


Figure 2.1: The two possible Feynman diagram of the *top* decay, based on the decay of the  $W$  boson

[1], with the Feynman diagrams represented in Figure 2.1.

$$t \rightarrow W^+ b \quad (2.1.1)$$

Figure 2.1(a) shows the  $W^+$  boson decaying leptonically to a charged anti-lepton (in order to preserve the electric charge) and a neutrino of the same family of the lepton (in order to preserve the lepton number), whereas Figure 2.1(b) shows the  $W^+$  boson decaying hadronically to a quark of "up" type (that is  $u, c$ ) and an antiquark of "down" type (that is  $d, s, b'$  respectively). All the quarks in the  $W$  decay process are the quarks in Equation (1.2.4), with the  $W$  boson acting only inside the same family.

The decay of the *top* quark is a weak process in that the flavour is not conserved. The life time is  $\tau_t \simeq 5 \times 10^{-25}$  s, lower than the average time it takes to form a hadron ( $t \simeq 10^{-24}$  s).

Because of the lifetime being so short, the resonance width  $\Gamma = \hbar/\tau$  is very small compared to its mass, with  $\Gamma_t = 1.32$  GeV.

## 2.2 Top quark production at the LHC

### 2.2.1 Pair production

At the Large Hadron Collider top quarks are produced predominantly in  $t\bar{t}$  pairs, a mechanism called pair production. It is a strong process, as the flavour is conserved, so the quarks are produced unpolarized due to parity being conserved in the strong interaction. The  $t\bar{t}$  production happens through *gluon-gluon fusion* or *quark-antiquark annihilation* at the leading order (LO) of QCD theory. Example Feynman diagrams for pair production are in Figure 2.2. At Tevatron, where proton and anti-proton collided with  $\sqrt{s} = 1.96$  TeV, the quark annihilation was the leading process (85%), while at LHC, where two proton beams collide with  $\sqrt{s} = 13$  TeV, gluon fusion dominates the process (90%), because of an antiquark being less present inside a proton than gluons are. The cross section at  $\sqrt{s} = 13$  TeV is  $832^{+40}_{-45}$  pb [24, 25].

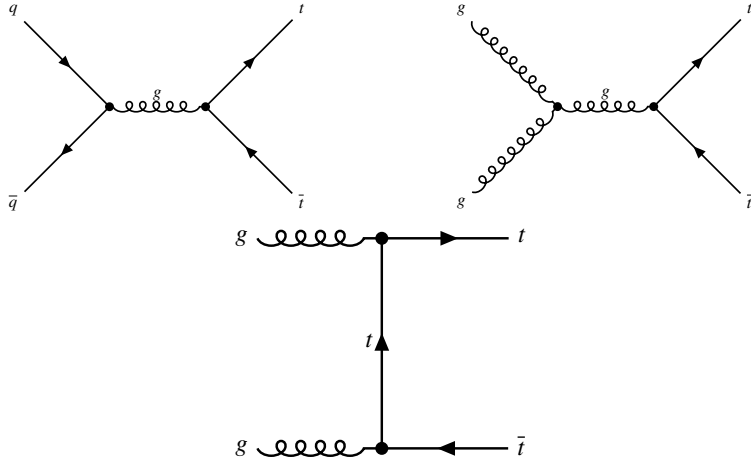


Figure 2.2: The three different LO Feynman diagrams for pair production of  $t\bar{t}$ . The first one is formed by quark annihilation, while the last one is formed by gluon fusion.

### 2.2.2 Single top production

A different way to produce the *top* quark is the single-top quark production. It is a weak process, in that it violates the flavour. Single *top* production can occur through three separates sub-processes:

- t-channel: it is the most dominant process for single *top* production. It involves the t-channel exchange of a virtual  $W$  boson between a light quark (most likely *up* or *down*) and a b-quark, generated by gluon splitting  $g \rightarrow b\bar{b}$  (See Figure 2.3(a)). Its cross section at  $\sqrt{s} = 13$  TeV is  $\sigma = 238^{+9}_{-8}$  pb [26].
- tW-channel: it involves the production of a real  $W$  boson by the s-channel exchange of a virtual b-quark (See Figure 2.3(b)). Its cross section at  $\sqrt{s} = 13$  TeV is  $\sigma = 71.7 \pm 3.8$  pb [26].
- s-channel: it is the least dominant process out of the three, it involves the s-channel exchange of a virtual space-like  $W$  boson which then decays into a *top* and a *bottom* quark (See Figure 2.3(c)). Its cross section at  $\sqrt{s} = 13$  TeV is  $\sigma = 10.3 \pm 0.4$  fb [26].

### 2.2.3 Top quark and $Z$ boson associated productions

With the unprecedented integrated luminosity collected by the experiments at the LHC, rare top production processes, as those where a top quark is produced in association with a  $Z$  boson, are now accessible. The most common *top* and  $Z$  boson associated production processes are:

- $t\bar{t}Z$ . It involves a  $t\bar{t}$  pair production associated with a  $Z$  boson. This process has been observed at LHC, and the cross section measured at  $\sqrt{s} = 13$  TeV and

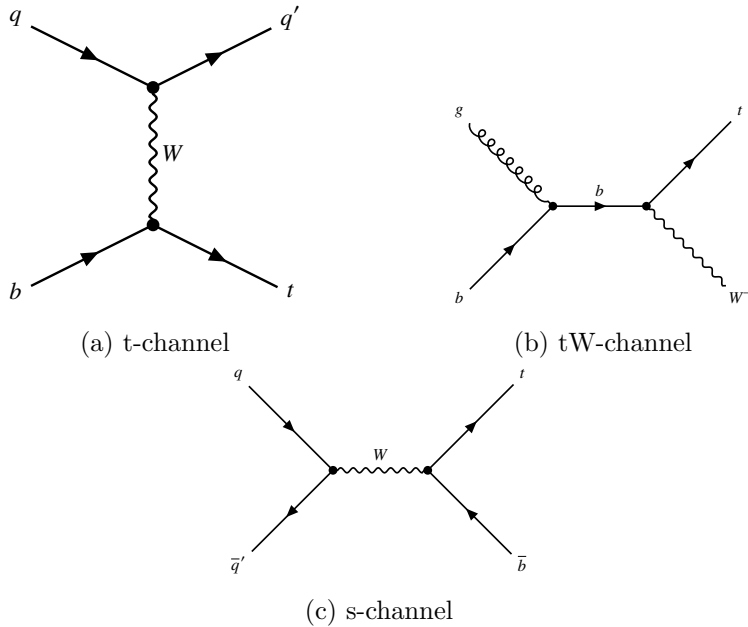


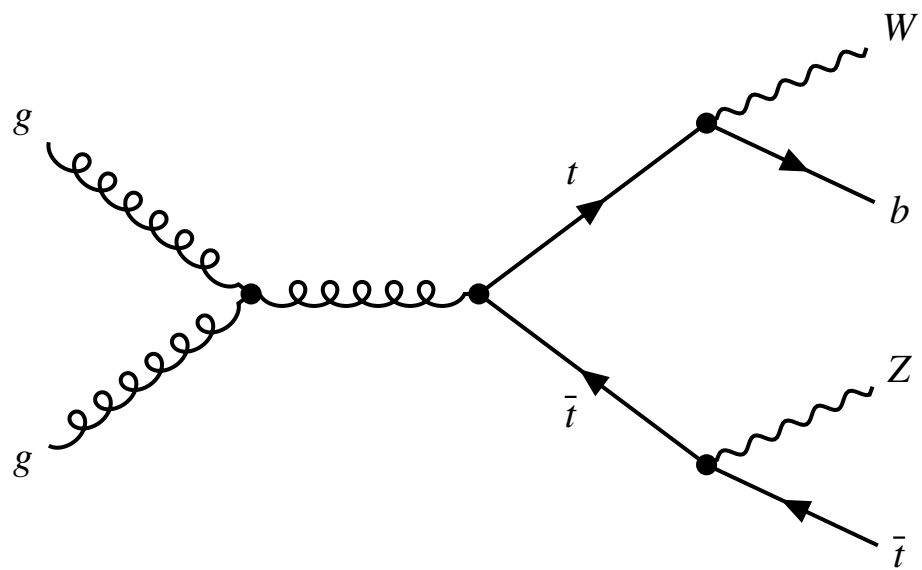
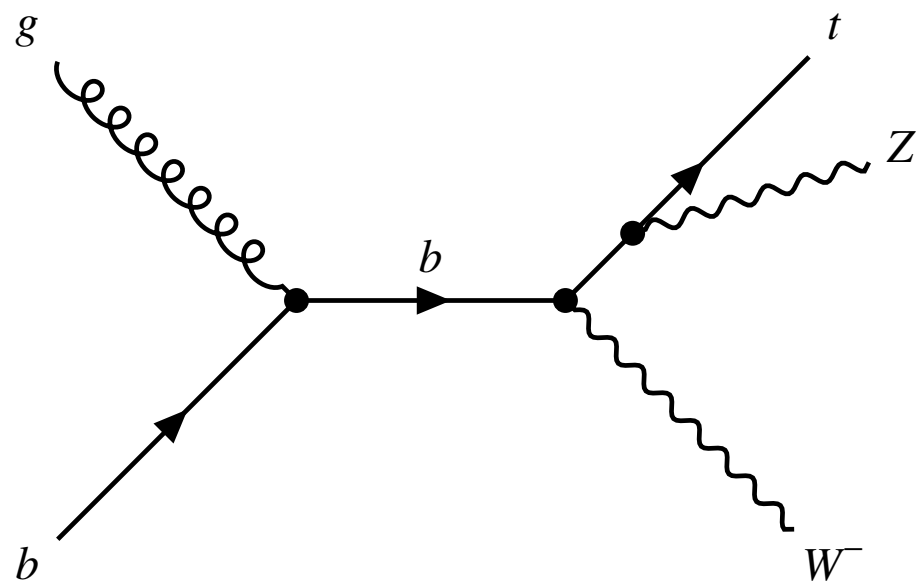
Figure 2.3: Feynman diagram for the single top production

integrated luminosity of  $139 \text{ fb}^{-1}$  is  $\sigma = 0.99 \pm 0.05(\text{stat.}) \pm 0.08(\text{syst.}) \text{ pb}$  [27]. Example Feynman diagram can be seen in Figure 2.4.

- $tZq$ . It involves the production of a single *top* quark in the t-channel in association with a  $Z$  boson. This process will be described in Section 2.2.4.
- $tWZ$ . It involves a single *top* quark production and a pair of a  $W$  and a  $Z$  boson. This process has not been measured yet, and the predicted cross section at  $\sqrt{s} = 13 \text{ TeV}$  is  $\sigma \simeq 160 \text{ fb}$  [28]. Example Feynman diagram of this process is in Figure 2.5.

## 2.2.4 $tZq$

The  $tZq$  is the process I am focusing on in this thesis. It is an electroweak process observed by the ATLAS and CMS experiments at  $\sqrt{s} = 13 \text{ TeV}$  with an integrated luminosity of  $139 \text{ fb}^{-1}$  [29]. I am going to heed my attention to the leptonic decay of the  $Z$  boson, so that the final state is  $t\ell^+\ell^-q$ . Another requirement is that the  $W$  boson, coming from the *top* quark decay, decays leptonically, thus giving us a three-lepton final state. The measured cross section for this process is  $\sigma = 97 \pm 13(\text{stat.}) \pm 7(\text{syst.}) \text{ fb}$  [29], comparable with the theoretical cross section, which is  $102 \text{ fb}$ . Example of LO Feynman diagrams for the resonant  $\ell^+\ell^-$  production are represented in Figures 2.6 and 2.7.

Figure 2.4: Example Feynman diagram for the  $t\bar{t}Z$  productionFigure 2.5: Example Feynman diagram for the  $tWZ$  production

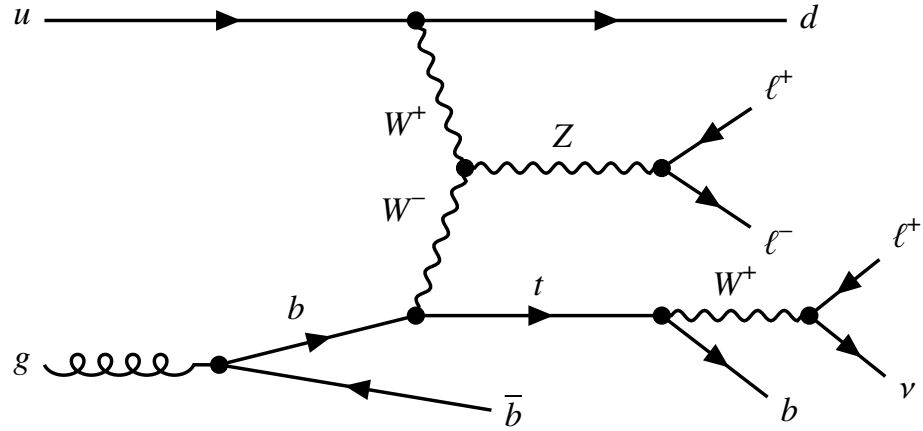


Figure 2.6: Example Feynman diagram for the  $tZq$  production with three lepton final state in four-flavour scheme

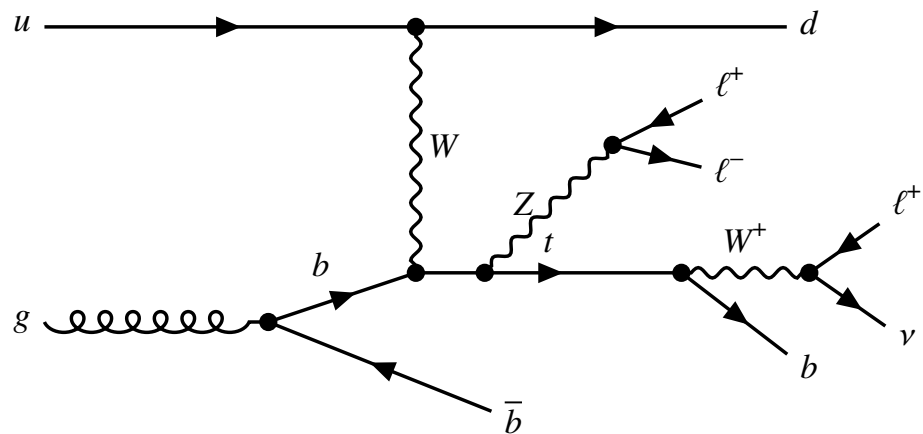


Figure 2.7: Example Feynman diagram for the  $tZq$  production with three lepton final state in four-flavour scheme

## Chapter 3

# The Large Hadron Collider and the ATLAS Experiment

### 3.1 The Large Hadron Collider

The Large Hadron Collider (LHC) [30] is the world's largest and most powerful particle accelerator. It has been active since 2008 as the latest addition to CERN's accelerator complex in Geneva. In Figure 3.1, an aerial view of the underground tunnels of LHC can be seen and in Figure 3.2 a scheme of the acceleration chain is represented. LHC was built using the tunnels of the old LEP (Large Electron-Positron Collider). The LHC is a 26.7 km ring built at an average depth of 100 m. It can accelerate two proton beams in opposite directions and make them collide at a center of mass energy of  $\sqrt{s} = 14$  TeV (even though now it operated at  $\sqrt{s} = 13$  TeV), but it can also accelerate and collide heavy ion beams at  $\sqrt{s_{NN}} = 5.5$  TeV. The beams are firstly accelerated by a linear accelerator (LINAC 2, *Linear Accelerator*) and then by four circular accelerators: PSB (*Proton Sicrotron Booster*), PS (*Proton Sicrotron*), SPS (*Super Proton Sicrotron*) and LHC. The beams then collide in four different points of collision, where four experiments are located:

- ATLAS (*A Toroidal LHC Apparatus*)[31].
- CMS (*Compact Muon Solenoid*)[32].
- ALICE (*A Large Ion Collider Experiment*)[33].
- LHCb (*LHC beauty*)[34].

The first two experiments both aim at to better understand the Standard Model (e.g. by looking for the Higgs boson, discovered by both ATLAS and CMS) and search for new physics beyond the Standard Model, e.g. SUSY. ALICE studies the high energy interactions between heavy ions in a plasma state, whereas LHCb explores the heavy flavour physics.



Figure 3.1: Aerial view of the underground tunnels of the Large Hadron Collider, with the four largest detectors.

### 3.1.1 Properties

#### Center of mass energy

The maximum center of mass energy reached by the LHC is  $\sqrt{s} = 13$  TeV, even though this value could go up to 14 TeV. A higher center of mass energy means more energy available after the collision.

#### Bunches

Protons are stored in bunches. During Run-2, the number of protons per bunch has been  $1.2 \times 10^{11}$ , with the bunches being spaced by 25 ns. The number of bunches per proton beam was 2500 for Run-2, and it is expected to rise up to 2800 for Run-3 [35].

#### Frequency of collisions

During Run-1 the frequency of collision was 20 MHz, whereas in Run-2 it has been increased to 40 MHz [36].

#### Magnets

There are 9593 magnets, of which 1232 dipoles, used to deflect the beams, and 392 quadrupoles, used to focalise the beam. The magnets are made of superconducting

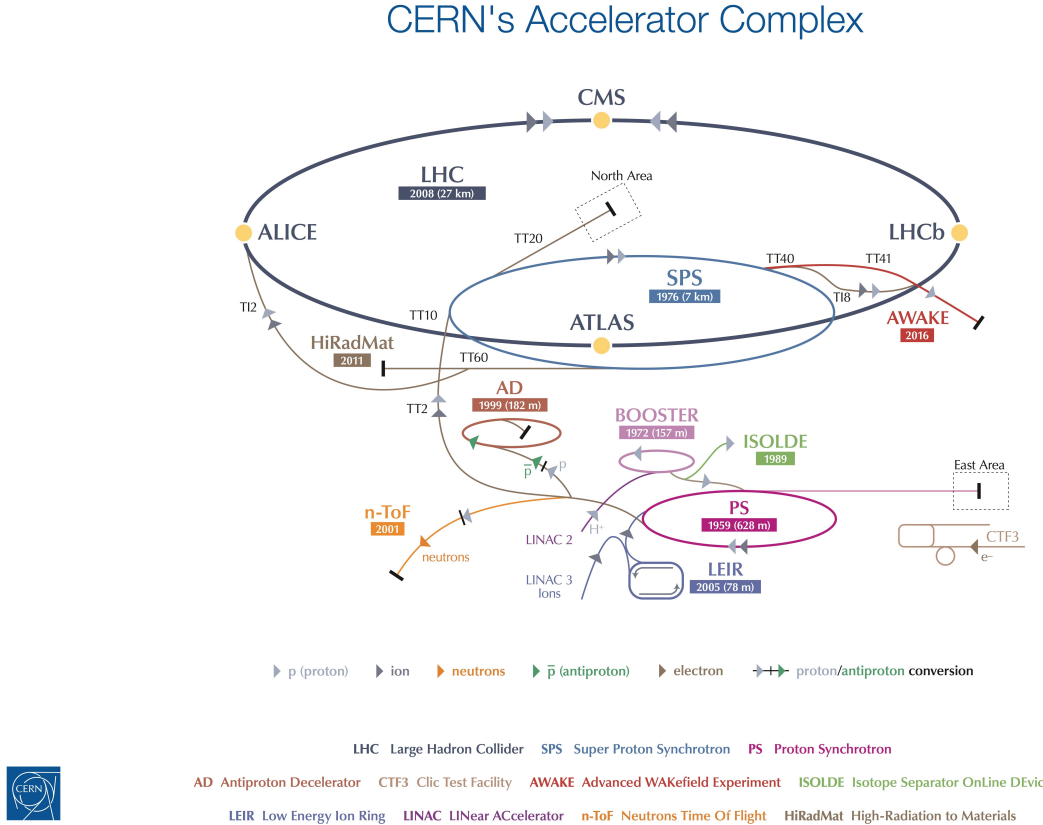


Figure 3.2: A schematic view of the acceleration chain at CERN.

materials and are kept at temperatures above 1.9 K, generating fields of around 7.7 T [30].

### RF cavities

There are eight Radio-Frequencies cavities per beam where the beam are accelerated with an electric field of frequency  $\nu = 400.8$  MHz [36].

### Instantaneous Luminosity

Luminosity is defined as the proportional constant between the rate of events  $R$  and the cross section  $\sigma$  of the same event,  $R = L\sigma$ . It is measured as  $L = n_b N_1 N_2 F / 4\pi\varepsilon\beta^*$ <sup>1</sup>. The luminosity is measured in  $b^{-1}s^{-1}$ . A higher luminosity means more statistics, thus allowing for rarer events to be seen. During Run2, the LHC reached a peak instantaneous luminosity of  $L = 2 \times 10^{30} b^{-1}s^{-1}$  [35].

<sup>1</sup> $n_b$  is the number of colliding bunches,  $N_1$  and  $N_2$  are the number of protons per bunch,  $\varepsilon$  is the beam emittance,  $\beta^*$  is a factor that considers the focus of the magnets and  $F$  is the geometric luminosity reduction factor due to the crossing angle at interaction point.

### Integrated luminosity

Because we consider the cross section to be time-independent, when integrating the formula for the rate  $R = L\sigma$ , we get  $\int R dt = N = \int L(t)dt \times \sigma$  where  $N$  is the number of total events and  $\int L(t)dt$  is the integrated luminosity. The integrated luminosity, whose unit of measure is the inverse barn  $b^{-1}$ , is a useful variable to evaluate the number of events expected for a process where the cross section is known. Throughout the years, the integrated luminosity available at the ATLAS experiment has been increasing, as can be seen in Figure 3.3. In this thesis I am going to look at the Run-2 Data, which includes the 2015-2018 events. The integrated luminosity of the full Run-2 data-taking period events is  $139 \text{ fb}^{-1}$ , as can be seen in Figure 3.4, split into  $36.2 \text{ fb}^{-1}$  for 2015-2016,  $44.3 \text{ fb}^{-1}$  for 2017 and  $58.5 \text{ fb}^{-1}$  for 2018.

### Pileup

The pileup is the phenomenon that occurs when multiple proton-proton collisions take place in the same time window of 25 ns in which the proton bunches collide. The multiple collisions lead to particle interaction events that overlap in the detector. The additional collisions, also called pileup, result in more particles being in the detector. The number of interaction per crossing  $\mu$  is the number of additional collisions occurring when two proton beams collide. It increases with luminosity, because the rate of the events is higher, as can be seen in Figure 3.5, and during Run2 on average it was 33.7.

## 3.2 The ATLAS experiment

The ATLAS experiment has been active since 2008, and aims at the study of both SM and BSM processes studying proton-proton collisions. The ATLAS detector (Figure 3.6) is the biggest detector at LHC, being 46 meters long with a 25 meters diameter. It is placed 100 meters below ground and it weights 7000 tonnes [38]. A complete description of the ATLAS detector can be found in [31]. It has a cylindrical symmetry, with the x-axis pointing toward the centre of the collision tunnel and the z-axis pointed along the tunnel. The azimuthal angle  $\phi$  is measured from the x-axis around the beam. The pseudorapidity  $\eta$  is defined as  $\eta = -\ln(\tan \frac{\theta}{2})$ . Transverse quantities, such as the transverse momentum  $p_T$ , transverse energy  $E_T$  and missing transverse energy  $E_T^{\text{miss}}$  are defined in the  $x - y$  plane, whereas the distance  $R$  is defined in the pseudorapidity-azimuthal space as  $R = \sqrt{\Delta\eta^2 + \Delta\phi^2}$ . Because of its cylindrical structure, the detector surrounds almost entirely the interaction point.

The ATLAS detector is made of different layers of subsystems, each of them with a specific target, as can be seen in Figure 3.7:

- the Inner Detector (ID). It is the closest system to the interaction point, it supplies the tracks of the charged particles. It is embedded in a 2 T solenoidal magnetic

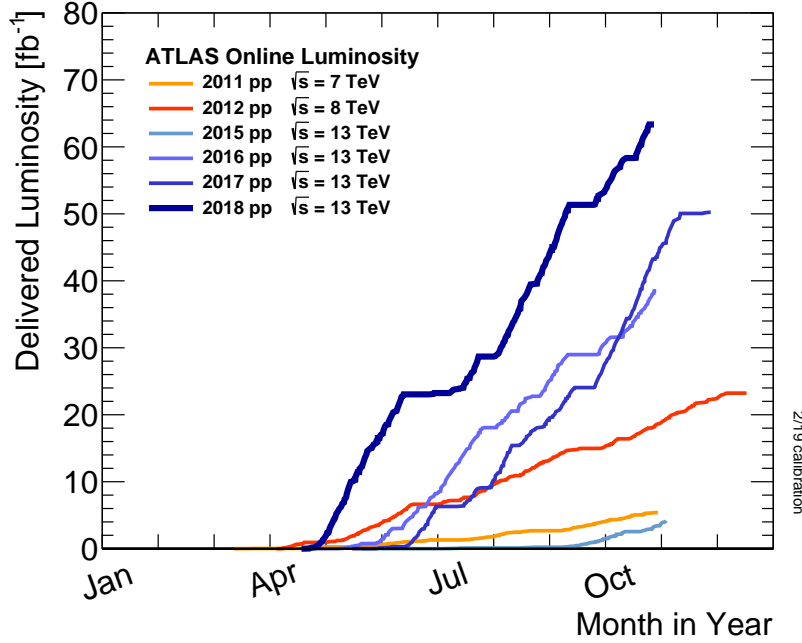


Figure 3.3: Cumulative luminosity versus day delivered to ATLAS during stable beams and for high energy p-p collisions [37].

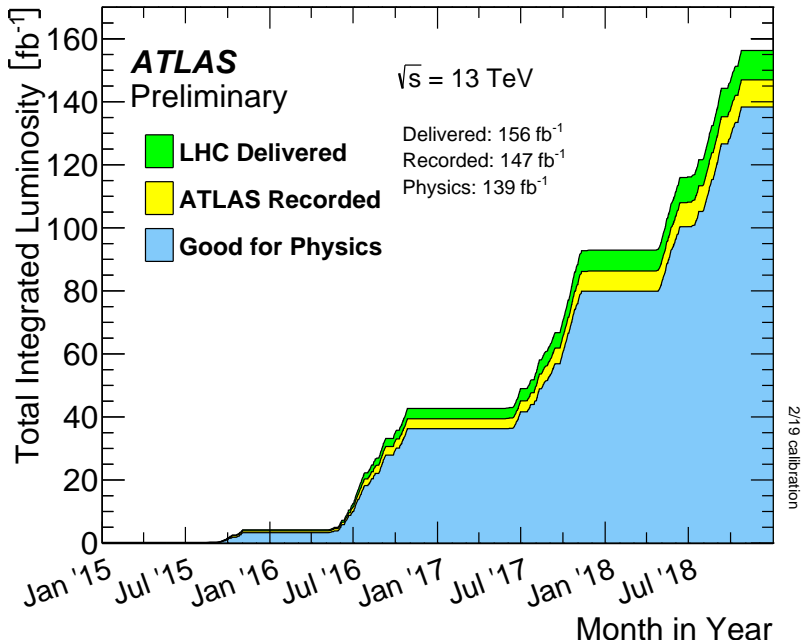


Figure 3.4: Cumulative luminosity versus time delivered to ATLAS (green), recorded by ATLAS (yellow), and certified to be good quality data (blue) during stable beams for pp collisions at 13 TeV centre-of-mass energy in 2015-2018 [37].

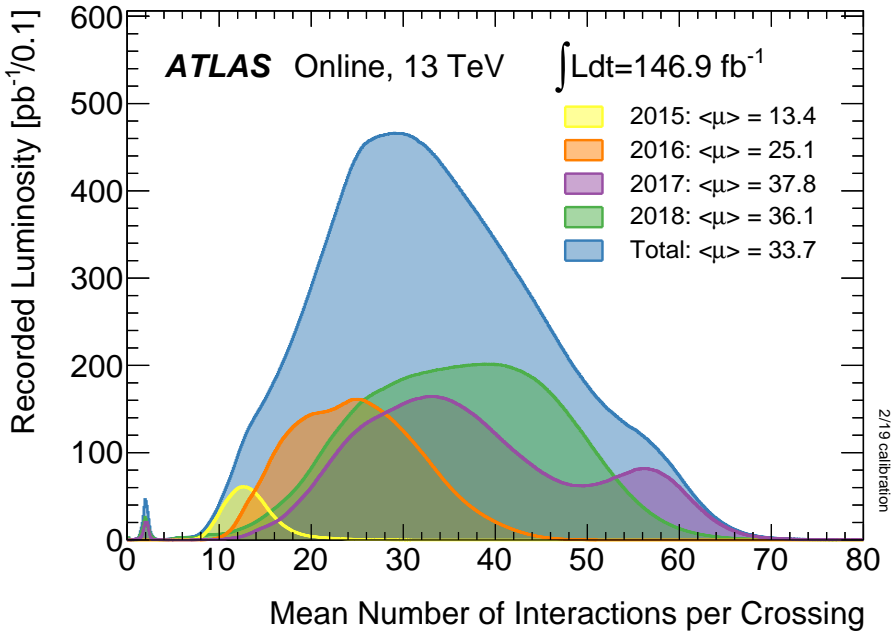


Figure 3.5: Luminosity-weighted distribution of the mean number of interactions per crossing for the 2015-2018  $pp$  collision data at  $\sqrt{s} = 13$  TeV. The integrated luminosity and the mean  $\mu$  value are shown separately for each year [37].

field, so, by measuring the trajectory of the particles, it provides informations about the momentum and the charge of said particles.

- the Electromagnetic Calorimeter (ECAL). It surrounds the ID, its purpose is to stop the electrons and the photons in order to measure their energy.
- the Hadronic Calorimeter (HCAL). It environs the ECAL, its aim is to measure the energy of the hadrons by stopping them.
- the Muon Spectrometer (MS). It is embedded in a toroidal magnetic field, it is designed to reconstruct the momentum and trajectory of the muons.

The general performance goals of the different layers are summarised in Table 3.1.

### 3.2.1 The magnets

ATLAS has a system of four large superconducting magnets. The system is 26 m long and 22 m wide, and stores an energy of 1.6 GJ. There are two type of magnets: the central solenoid (Figure 3.8(a)) and the barrel and end-caps toroids (Figure 3.8(b)).

The solenoid provides a 2 T axial magnetic field. The toroids are responsible for the magnetic field of the Muon Spectrometer. There are three toroids: the barrel, Figure 3.8(b), and two end-cap toroids. The field is centred on the beam axis, perpendicular to the field generated by the solenoid. The barrel toroid provides 1.5 to 5.5 T m of

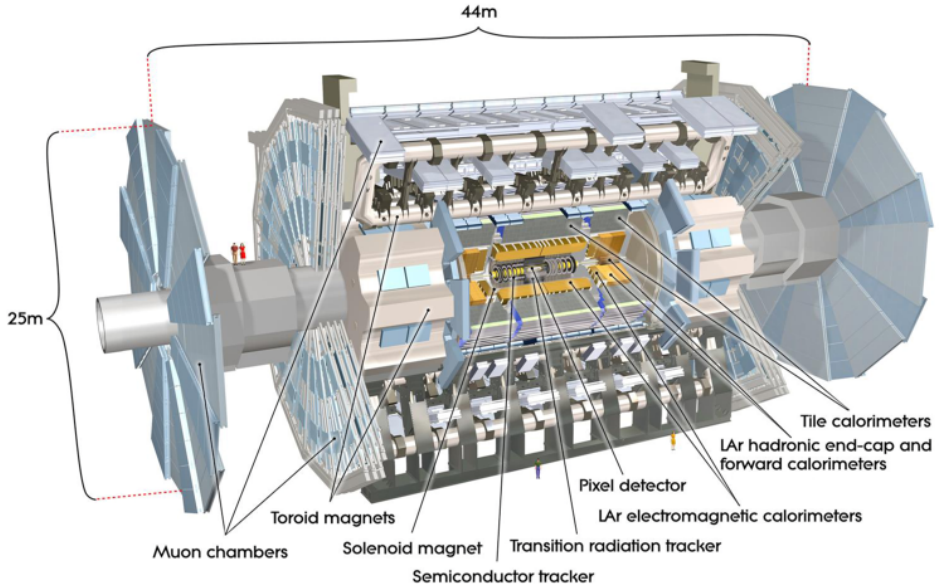


Figure 3.6: Cut-away view of the ATLAS detector[31].

Detector component	Required resolution	$\eta$ coverage Measurement (Trigger)
Tracking (ID)	$\sigma_{p_T}/p_T = 0.05\% p_T \oplus 1\%$	$\pm 2.5$
ECAL	$\sigma_E/E = 10\%\sqrt{E} \oplus 0.7\%$	$\pm 3.2 (\pm 2.5)$
HCAL barrel and end-cap forward	$\sigma_E/E = 50\%\sqrt{E} \oplus 3\%$ $\sigma_E/E = 100\%\sqrt{E} \oplus 10\%$	$\pm 3.2$ $3.1 <  \eta  < 4.9$
Muon Spectrometer	$\sigma_{p_T}/p_T = 10\% \text{ at } p_T = 1 \text{ TeV}$	$\pm 2.7 (\pm 2.4)$

Table 3.1: General performance goals of the ATLAS detector[31]. When not stated otherwise, the  $\eta$  trigger value is the same as the measurement one.

bending power in the range  $|\eta| < 1.4$  whereas the end-cap toroids provide 1 to 7.5 T m of bending power in the range  $1.6 < |\eta| < 2.7$ . In the overlap region  $1.4 < |\eta| < 1.6$ , the bending power is lower.

### 3.2.2 The Inner Detector

The ATLAS Inner Detector (See Figure 3.9) is designed to provide hermetic and robust pattern recognition, high momentum resolution and both primary and secondary vertex measurements for charged particles above a given  $p_T$  threshold, usually 0.5 GeV, and within the range  $|\eta| < 2.5$ . It is made of three different sub-detectors:

- Pixel detector. It is the nearest detector to the collision point, it has four layers of silicon sensors and it provides four measurement points for tracks with  $|\eta| < 2.5$  and it has a full coverage in  $\phi$ . It has a cylindrical barrel region and two end-caps regions, containing each three disks. The fourth layer (IBL) was installed in 2014 at  $R = 25.7$  mm, making it the closest one to the beam, thus allowing four

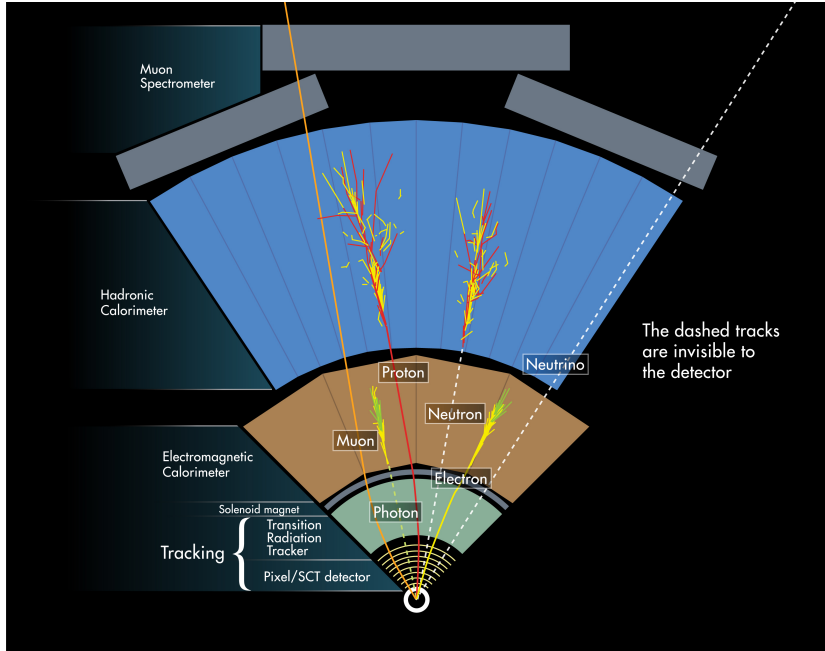


Figure 3.7: Diagram of particle paths in the ATLAS detector [39].

measurement points instead of three, as it was for Run-1. In Figure 3.9 only three layers are shown, because the drawing is from the original paper [31] describing the structure of the ATLAS detector, and in 2008 there were only three layers.

- SemiConductor Trackers (SCT). It is also made of silicon sensors (with a wider segmentation w.r.t. the pixel detector). It surrounds the Pixel detector in four coaxial cylindrical layers in the barrel region and two end-caps containing each nine disk layers. It operates at a temperature of  $-7^{\circ}\text{C}$ , same as the Pixel detector.
- Transition Radiation Tracker (TRT). It is the outermost system of the Inner Detector and it includes almost 300 000 proportional drift tubes (straws). The

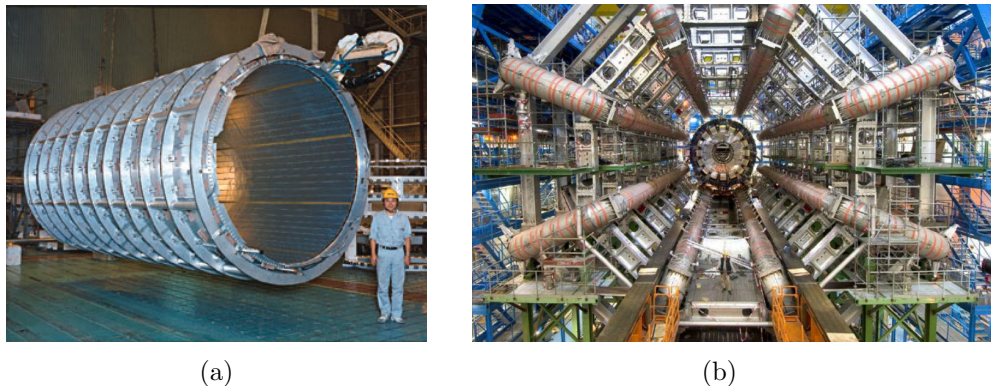


Figure 3.8: Photos of the magnets of the ATLAS experiment: the central solenoid Figure 3.8(a) and the barrel toroidFigure 3.8(b) [31].

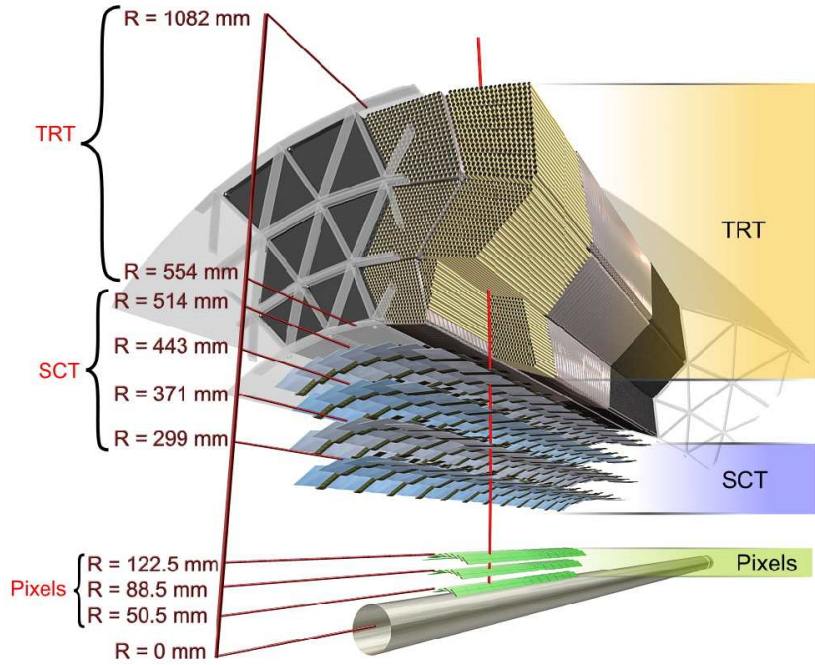


Figure 3.9: Drawing showing the sensors traversed by a charged particle in the Inner Detector [31].

TRT was designed so that particles with  $p_T > 0.5$  GeV and  $|\eta| < 2$  cross typically more than 30 straws. It can also be used for particle identification, because the charged particles passing through the boundary region between materials with different refraction index emits X-ray radiation whose intensity is proportional to the relativistic  $\gamma$  factor.

The Inner Detector is fully immersed in a solenoidal 2 T magnetic field generated by the Central Solenoid (CS), which operates at a temperature of 4.5 K.

### 3.2.3 The calorimeter system

The calorimeter system (See Figure 3.10) includes both the Electromagnetic Calorimeter (ECAL) and the Hadron Calorimeter (HadCAL). The first is dedicated to the study of photons and electrons, whilst the latter is dedicated to the measurement of hadrons. They cover a range of  $|\eta| < 4.9$ .

The main purpose of the calorimeter system is to measure the energy and the position of the particles, and it does that having good containment for both electromagnetic and hadronic showers. Therefore, calorimeter depth is an important consideration. The thickness of the ECAL is more than 22 radiation lengths ( $X_0$ ). In this way, the ECAL is able to contain 2/3 of a typical hadronic shower. The rest of the calorimeter is designed for missing energy and jet reconstruction. The total thickness of the ECAL+HCAL system is  $\sim 10\lambda$ , with  $\lambda$  being the interaction length, which is wide enough to reduce punch-through into the muon system.

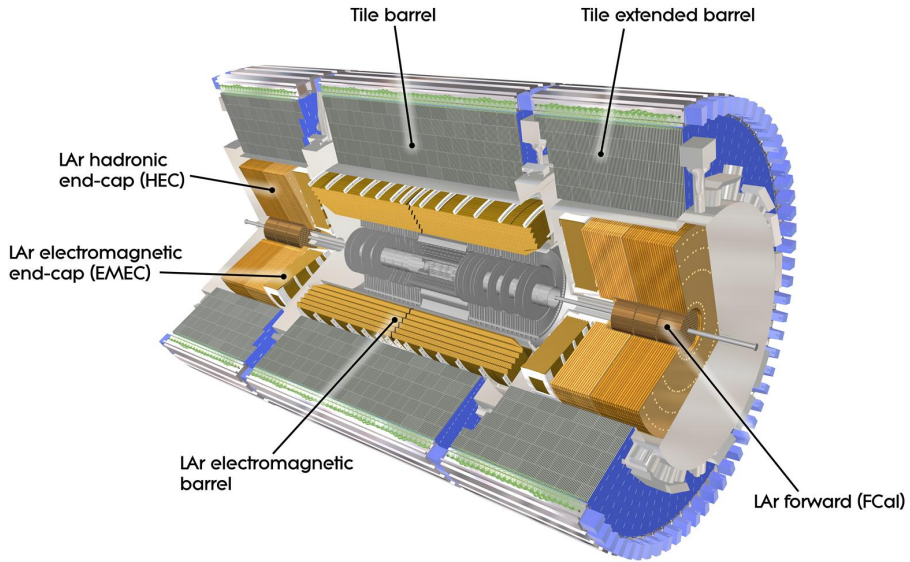


Figure 3.10: A schematic view of the calorimeter system of the ATLAS Experiment [31].

The Electromagnetic Calorimeter is a lead liquid Argon (LAr) detector with accordion-shaped kapton electrodes and lead absorber plates over its full coverage. This geometry allows for complete  $\phi$  symmetry without azimuthal cracks.

The Hadronic Calorimeter is made of three different layers. The Tile calorimeter is placed directly outside the ECAL. It uses steel as an absorber. The LAr hadronic end-cap calorimeter consists of two independent wheels per end-cap, located behind the ECAL end-caps. The LAr forward calorimeter (FCal) is integrated into the end-cap, it reduces the radiation background levels in the muon spectrometer, because of it being 10 interaction lengths deep. The FCal is made of three different modules. The first one is made of copper and it is optimised for electromagnetic measurements, while the other two are made of tungsten and are optimised for hadronic measurements of energy.

The detection process works as follows: incident particles shower in the absorber material, the LAr is ionised and the electrons, coming from the ionisation, drift due to an electric field being applied in the gap, inducing a signal in the read out electrodes.

### 3.2.4 The Muon Spectrometer

The Muon Spectrometer (MS) is the outermost detector of the ATLAS experiment. It is made of different muon chambers, as represented in Figure 3.11. The aim of the MS is to trigger and measure the muons, in particular the track reconstruction and the transverse momenta evaluation. It is immersed in a toroidal magnetic field which bends the muons (because of them being electrically charged), and it measures the tracks at three different points. Therefore, by measuring the sagitta  $s$ , it is possible to determine

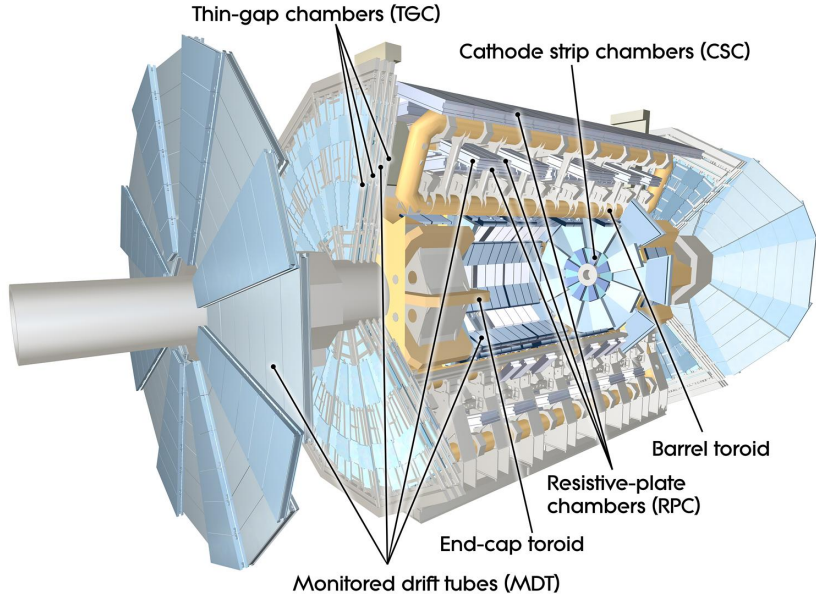


Figure 3.11: Cut-away view of the ATLAS muon system [31].

the transverse momentum  $p_T = L^2 qB/8s$ , where  $L$  is the length of the trajectory,  $B$  is the magnetic field and  $q$  is the charge of the muon (either  $\pm 1$ ).

### 3.2.5 Trigger system

ATLAS uses a two-levels trigger to select events: a hardware-based level (L1) is followed by a software-based High-Level Trigger (HLT).

The L1 trigger performs the initial event selection, reducing the rate of incoming data from 40 MHz to 100 kHz. Muons are identified in the barrel and in the end-caps regions of the spectrometer using dedicated trigger chambers, whereas calorimeter selections (electrons, photons and jets) are based on reduced-granularity information from all the calorimeters. The L1 decision must reach the front-end electronics within 2.5  $\mu$ s after the bunch-crossing, providing Regions of Interest (RoI) to the HLT. These regions are the ones where possible trigger objects within the event are identified. The HLT uses both fast and offline reconstruction algorithms to confirm the trigger decision. The output rate of the HLT trigger is 1 kHz.

### 3.2.6 Forward detectors

There are other detectors whose aim is to measure the luminosity. The closest one to the interaction point (17 m) is LUCID (LUminosity Cherenkov Integrating Detector, [40]), which detects inelastic  $pp$  scattering in the forward direction and it is the main online relative-luminosity monitor for ATLAS. LUCID is also used to check the beam losses before collisions. At 240 m from the collision ALFA (Absolute Luminosity For

ATLAS) is located, and finally there is ZDC (Zero-Degree Calorimeter) at 140 m from the interaction point.

## Chapter 4

# Optimisation of the event selection for $tZq$

In this section I am going to explain the work I have done in order to optimize the event selection for the  $tZq$  process. The process was observed with a 15% uncertainty on the cross section, and my results will facilitate reducing the uncertainty on the inclusive cross section and measuring the differential cross section.

Out of all the possible final states for the  $tZq$  process, the most interesting one is the trilepton final state, which occurs when both the  $Z$  and  $W$  bosons decay leptonically. The trilepton channel is the one with the lowest branching ratio, but it is the purest channel because it can be best separated from the backgrounds.

In Section 4.1 and Section 4.2 I will be describing the Data and MC samples respectively. In Section 4.3 I will discuss the object reconstruction process at the ATLAS detector, in Section 4.4 I will describe the event selection for my analysis, whereas in Section 4.5 I will briefly describe the state of the art for the  $tZq$  process. Finally, in Section 4.6 I will present my analysis for the optimisation of the event selection for  $tZq$  and in Section 4.8 I will check the data/MC agreement.

### 4.1 Data Samples

In this thesis I am focusing on the data collected by ATLAS during the full Run-2 (2015-2018) proton-proton collision at  $\sqrt{s} = 13$  TeV with a total integrated luminosity of  $139 \text{ fb}^{-1}$ .

Only events collected when the LHC beams were stable and the ATLAS detector fully operational are analysed. The Good Run List (GRL) allows to select only events satisfying these requirements. The GRLs used in this analysis are reported in Figure 4.1, alongside the integrated luminosity for each sample. The events were selected only if they satisfied at least one of the single-electron triggers or one of the single-muon triggers listed in Figure 4.2. The trigger for the transverse momentum  $p_T$  was 24 GeV in 2015 and 26 GeV from 2016 for the electrons and 20 GeV in 2015 and 26 GeV from

Year	Int. Lumi. ( $\text{fb}^{-1}$ )	Good Run List
2015	3.2	data15_13TeV/20170619/physics_25ns_21.0.19.xml
2016	33.0	data16_13TeV/20170605/physics_25ns_21.0.19.xml
2017	44.3	data17_13TeV/20180619/physics_25ns_Triggerno17e33prim.xml
2018	58.5	data18_13TeV/20181111/physics_25ns_Triggerno17e33prim.xml

Figure 4.1: Data samples used in the analysis

Year	Single $e$	Single $\mu$
2015	HLT_e24_lhmedium_L1EM20VH HLT_e60_lhmedium HLT_e120_lhloose	HLT_mu20_iloose_L1MU15 HLT_mu50
2016-2018	HLT_e26_lhtight_nod0_ivarloose HLT_e60_lhmedium_nod0 HLT_e140_lhloose_nod0	HLT_mu26_ivarmedium HLT_mu50

Figure 4.2: Trigger selections [41–44].

2016 for the muons[41–44].

## 4.2 Monte Carlo samples

Monte Carlo techniques are used in order to simulate the events coming from the inelastic collision of protons. The simulated events were grouped in three Monte Carlo simulated campaigns:

- **mc16a.** It contains the events simulating the data collected in 2015 and 2016. The total integrated luminosity to which these events have to be scaled to is  $36.2 \text{ fb}^{-1}$ .
- **mc16d.** It contains the events simulating the data collected in 2017. The integrated luminosity to which these events have to be scaled to is  $44.3 \text{ fb}^{-1}$ .
- **mc16e.** It contains the events simulating the data collected in 2018. The integrated luminosity to which these events have to be scaled to is  $58.5 \text{ fb}^{-1}$ .

The events are simulated using a set parameter for the mass of the *top* quark  $m_t = 172.5 \text{ GeV}$  and with a branching fraction of the  $t \rightarrow Wb$  decay of 1. In the following, I am going to describe the samples for both the signal and the SM backgrounds. A more accurate description of all the samples is in Appendix A.

### 4.2.1 Signal sample

The signal sample, as stated earlier, is  $tZq$ . The request is for both the  $Z$  and the  $W$  bosons to decay leptonically, thus having a three lepton plus one neutrino ( $3\ell 1\nu$ )

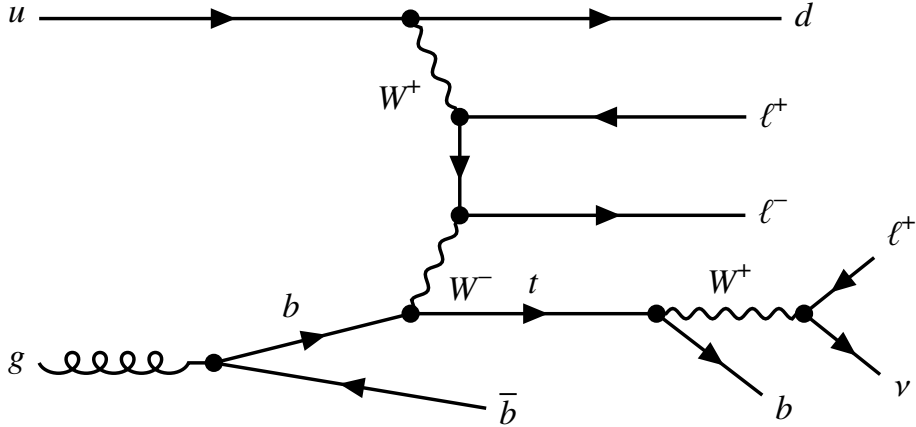


Figure 4.3: Feynman diagram for the non-resonant  $\ell^+\ell^-$  production, with a trilepton final state in four-flavour scheme

final state (See Figures 2.6 and 2.7). The SM cross section for the  $t\ell\ell q$  process (See Figures 2.6 and 2.7), including non-resonant lepton pairs (See Figure 4.3) with  $m_{ll} \geq 30$  GeV is 101.7 fb.

The signal sample shows an interesting confirmation of the parton model. The Feynman diagrams in Figures 2.6 and 2.7 have an *up* quark in the initial state, but we know that any other quark could be in its place. Inside a proton, the *up* and *down* quarks are the ones with the highest probability to be found, with the *up* quarks having twice the probability of the *down* quark. If we consider the  $tZq$  process initiated by a *down* quark, the Feynman diagram is different (See Figure 4.4). By comparing this diagram (Figure 4.4) with the diagram with the *up* quark (Figure 2.6), we can see that if there is an *up* quark in the initial state, the final state has one Opposite Sign Same Flavour (OSSF) lepton pair and one lepton with positive charge, whereas if we have a *down* quark in the initial state, we have the same OSSF lepton pair coming from the  $Z$  boson, but this time the third lepton (the one coming from the  $W$  boson) is a lepton with a negative charge.

If we plot the charge of the lepton coming from the  $W$  boson, we expect to have 67% of the times a lepton with a positive charge and the remaining 33% a lepton with a negative charge. This plot is represented in Figure 4.5, and it shows exactly that, because we have little less than  $120 \times 10^3$  events for the negative lepton and little less than  $240 \times 10^3$  events for the positive one.

#### 4.2.2 Background samples

The background is made of all the predicted SM processes.

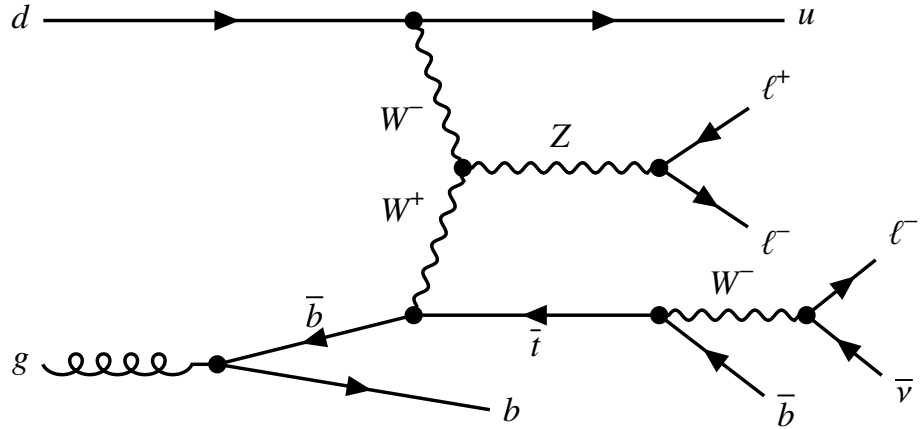


Figure 4.4: Feynman diagram of the signal with a *down* quark in the initial state

$t\bar{t}$

The pair production is the background with the highest number of events, due to it being a strong process. The pair production process is described in Section 2.2.1. The generated MC sample has a dilepton final state, with both *top* quarks decaying leptonically as in Figure 2.1(a).

$tW$

It is one of the three single-top channels, described in Section 2.2.2. It is the second most dominant channel out of the three, but it is the only one with an overlap with  $tZq$ . Therefore, the  $tW$  channel is the only single-top channel sample used in the analysis. There are two samples used. The first one has a *top* quark and a  $W^-$  boson in the final state, whereas the latter has an *anti-top* quark and a  $W^+$  boson. The samples both have two leptons in the final state, one coming from the leptonic decay of the  $W^\pm$  boson and the second from another leptonic decay of the  $W$  boson, which is generated by the decay of the *top* quark.

$t\bar{t}H$

It is a strong process with three different final states, pending the decay of the *top* and the *anti-top*. We can have a fully-hadronic ( $0\ell$ ) final state, that is when both  $t$  and  $\bar{t}$  decay hadronically, a one-lepton final state, which is when only one of the two  $W$  bosons decays leptonically and a dilepton final state when both  $W$  bosons decay leptonically.

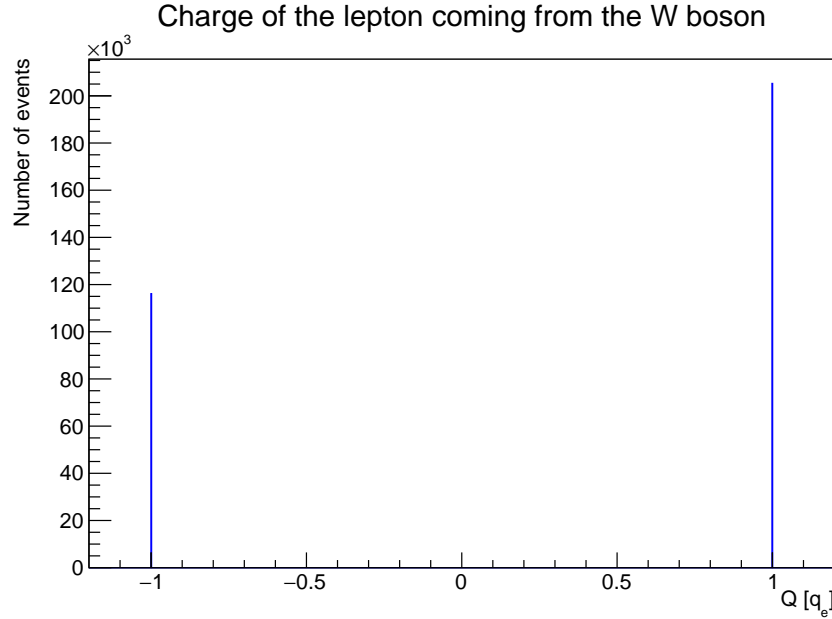


Figure 4.5: Number of events for the charge of the lepton coming from the  $W$  boson.

### $t\bar{t}W$

It is a process involving a strong *top* quark pair production associated with a  $W$  boson. There is only one sample, which is inclusive, in that the three  $W$  bosons (two from  $t\bar{t}$  and the third one) can decay either leptonically or hadronically.

### $t\bar{t}Z$

There are five different samples for  $t\bar{t}Z$ , depending on the  $Z$  boson decay ( $\nu\nu$ ,  $q\bar{q}$ ,  $e\bar{e}$ ,  $\mu\bar{\mu}$ ,  $\tau\bar{\tau}$ ). Non resonant lepton pairs with  $m_{ll} > 5$  GeV are also included. These samples are inclusive in the  $W$  boson, which means that they allow the  $W$  boson from *top* quark decay to decay both leptonically and hadronically.

### $tWZ$

The  $tWZ$  process was described in Section 2.2.3. There is one sample, in which both the leptonic and the hadronic decay of the *top* quark are included, whereas the  $Z$  boson is forced to decay into a couple of leptons.

### $Z+jets$

The samples belonging to  $Z+jets$  are all the samples where a  $Z$  boson decays leptonically. Non resonant lepton pairs are included, provided their invariant mass  $m_{ll}$  is greater than 40 GeV.  $Z+jets$  is one of the main backgrounds that has to be dealt with. Because the

request is for a trilepton final state with at least one jet, this sample can be mistaken for the signal when a fake lepton and two additional jets are produced.

### 3 top

This sample has 3 *top* quarks, either being two *top* and an *anti-top* or the opposite. The final state has 3 *b*-jets and 3 *W* bosons. The sample is inclusive.

#### Diboson

In this category all the samples containing two bosons (either a *W* or a *Z*) with at least two charged leptons in the final state are included. We have two samples with on shell diboson production with factorised decays, which are  $Z(\rightarrow q\bar{q})Z(\rightarrow \ell\ell)$  and  $W(\rightarrow qq')Z(\rightarrow \ell\ell)$ . They are both semi-leptonic diboson samples. Then we have three fully-leptonic samples:  $\ell\ell\ell\ell$ ,  $\ell\ell\ell\nu$  and  $\ell\ell\nu\nu$ . The requirements are for the invariant mass of Opposite Sign Same Flavour (OSSF) leptons  $m_{ll}^{OSSF}$  to be greater than 4 GeV and for the momentum of the two leptons with higher invariant mass to be greater than 5 GeV.

#### Electroweak $VVjj$

Three samples are part of this group. We have  $\ell\ell\ell\ell jj$ ,  $\ell\ell\ell\nu jj$  and  $\ell\ell\nu\nu jj$ . A *Z* boson is required every time, and that means that the two leptons in the  $\ell\ell\nu\nu jj$  sample must be of opposite sign but same flavour. In this samples also triboson  $VVV$  diagrams where one of the bosons decays hadronically ( $V \rightarrow jj$ ) are included. The possible decays of the two bosons are described above in the Diboson category.

#### Triboson

For the triboson category we have seven samples, all of them requiring on shell  $VVV$  production with factorised fully leptonic decays.

## 4.3 Object reconstruction

The reconstruction of the basic objects used in the analysis is described in the following.

#### Primary vertex

The primary vertex [45] of the interaction is selected as the  $pp$  vertex candidate with the highest sum of the  $p_T^2$  of all the associated tracks with  $p_T > 500$  MeV.

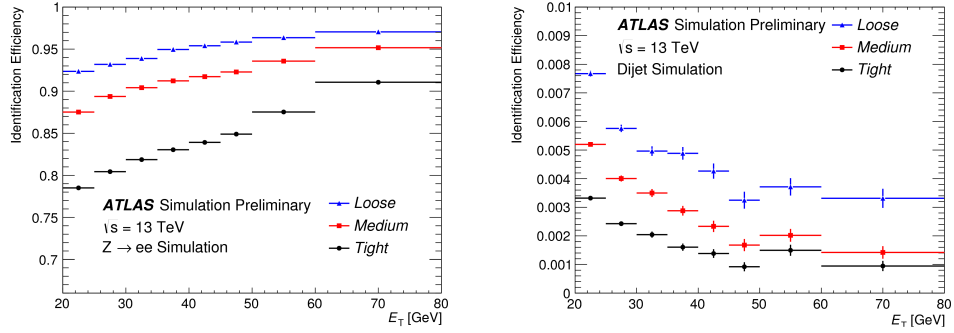


Figure 4.6: The efficiency to identify prompt electrons (left) and to identify hadrons as electrons (background rejection, right) at different values of  $E_T$  for the different IDWPs [48].

## Electrons

The electrons in the central region of the ATLAS detector, i.e., the electrons with  $|\eta| < 2.47$ , are reconstructed from energy deposits in the electromagnetic calorimeter which have a match with a track in the inner detector [46]. The transition region ( $1.37 < |\eta| < 1.52$ ) between the barrel and the end-caps of the ECAL is excluded. The electrons are required to have  $E_T^1 > 10$  GeV. The electrons are then identified through three different Identification Working Points (IDWPs), **Tight**, **Medium** or **Loose**. A Working Point is a set of cuts and selections which gives a certain efficiency on the identification or isolation of an object. The efficiency for identifying a prompt electron (that is, an electron from e.g.  $Z$  boson decay) with  $E_T = 40$  GeV is 93% for **Loose**, 88% for **Medium** and 80% for **Tight**[47]. These working points require at least two hits in the pixel detector and seven hits total in the pixel and silicon-strip detectors combined. For **Medium** and **Tight**, one of the pixels must belong to the innermost pixel layer, in order to reduce the background from photon conversion, that is the misidentification of an electron with a photon.

In this analysis the electrons must pass the **Tight** selection to reject electrons from photons, hadronic particle decays and fake electrons. The **Tight** selection was used because, as can be seen in Figure 4.6, even though we lose a lot of prompt electrons, because of the efficiency being not so high, we also lose a lot of fakes for the same reason.

The electrons then have to be isolated, and we do that by using different isolation Working Points (WPs) that will be described in the following. In the paper regarding the observation of the  $tZq$  process [29] the **Gradient** isolation WP was used. The object of this thesis is to verify if there is any other isolation Working Point that works better for the signal/background discrimination.

---

<sup>1</sup> $E_T = E \sin \theta$

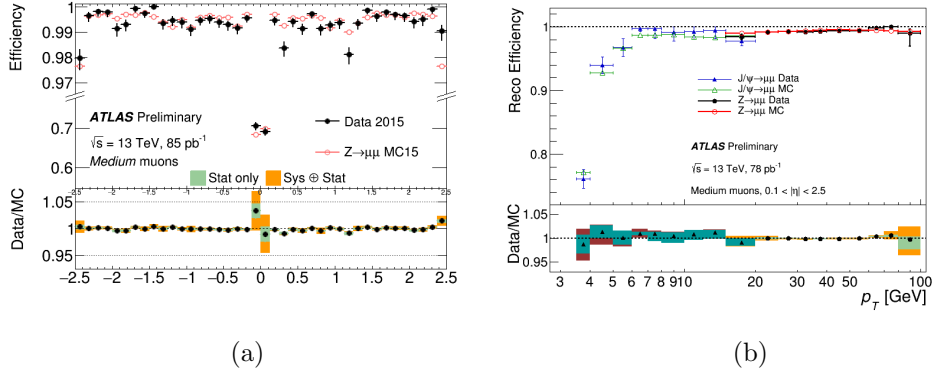


Figure 4.7: Muon reconstruction efficiency for the Medium IDWP as a function of pseudorapidity  $\eta$  (left) and  $p_T$  (right)[49].

## Muons

The muons at ATLAS are reconstructed either using the information from both the Muon Spectrometer and the Inner Detector (combined muons (CB)) or from the MS alone (standalone (SA)).

The Identification Working Points (IDWPs) used for muons are **Tight**, **Medium** and **Loose**, same as the electrons. The **Medium** selection is used to identify both CB and SA muons. It is a WP which minimise the systematic uncertainties associated with muon reconstruction and calibration. The efficiency at different values of  $\eta$  for muons from  $Z \rightarrow \mu^+ \mu^-$  is shown in Figure 4.7(a). It can be noted how the **Medium** algorithm has a high efficiency, close to 99%, over the full  $\eta$  range, with the exception of the central region ( $|\eta| < 0.1$ ). The efficiency as a function of  $p_T$  in both  $Z \rightarrow \mu^+ \mu^-$  and  $J/\psi \rightarrow \mu^+ \mu^-$  is shown in Figure 4.7(b). From there, it can be seen that the efficiency is close to 99% for muons with transverse momentum  $p_T$  higher than 7 GeV.

Muons are required to have  $|\eta| < 2.5$  and  $p_T > 15$  GeV. Same as for the electrons, muons in the analysis [29] were isolated using the **Gradient Isolation** WP.

## Jets

Jets reconstruction in the calorimeter starts from grouping together energy deposits in adjacent cells of the calorimeter, creating a *topocluster*. Topoclusters are formed by a growing-volume algorithm starting from a calorimeter cell with a highly significant seed signal. The basic observable controlling the cluster formation is the cell significance  $\zeta_{cell}^{EM}$ , defined as in Equation (4.3.1).

$$\zeta_{cell}^{EM} = \frac{E_{cell}^{EM}}{\sigma_{noise,cell}^{EM}}^2 \quad (4.3.1)$$

The seeding, growth and boundary features of the topoclusters are defined by three respecting parameters ( $S, N, P$  respectively). This three define signal thresholds in terms of  $\sigma_{noise,cell}^{EM}$  and thus apply selections based on  $\zeta_{cell}^{EM}$  (Equation (4.3.1))

$$|E_{cell}^{EM}| > S\sigma_{noise,cell}^{EM} \implies |\zeta_{cell}^{EM}| > S \text{ (default } S = 4\text{)}; \quad (4.3.2)$$

$$|E_{cell}^{EM}| > N\sigma_{noise,cell}^{EM} \implies |\zeta_{cell}^{EM}| > N \text{ (default } N = 2\text{)}; \quad (4.3.3)$$

$$|E_{cell}^{EM}| > P\sigma_{noise,cell}^{EM} \implies |\zeta_{cell}^{EM}| > P \text{ (default } P = 0\text{)}. \quad (4.3.4)$$

The cells near the seed are selected as belonging to the topocluster if their  $\zeta_{cell}^{EM}$  is greater than the thresholds given in Equations (4.3.2) to (4.3.4). The total energy of the topocluster is defined as the sum of the energy deposits of all the cells belonging to the topocluster.

Another parameter used to identify and group topoclusters is the radius  $R$ . We evaluate the distance between clusters as  $\Delta R_{i,j}^2 = (Y_i - Y_j)^2 + (\phi_i - \phi_j)^2$  ( $Y$  is the rapidity), and if said distance is smaller than  $R$ , the two clusters are merged into a single jet. The jet algorithm is iterative. First we compute the values  $d_i = (k_T^{(i)})^{2p}$ ,  $d_{i,j} = \min \left[ (k_T^{(i)})^{2p}; (k_T^{(j)})^{2p} \right] \frac{\Delta R_{i,j}^2}{R^2}$  and  $d_{\min} = \min(\{d_i\} \cup \{d_{ij}\})$  for each object of our list. If we find an  $i$  such that  $d_i \equiv d_{\min}$ , then  $i$  is defined as a jet and it is removed from the list. Otherwise, there must be a pair  $(i, j)$  such that  $d_{i,j} = d_{\min}$ . When this is the case, we merge together the objects  $i$  and  $j$  into a new object whose four-momentum  $k$  is the sum of the four-momentum of the two objects. We then remove this new object from the list. We reiterate on all the objects until we find only jets.

The exponent  $p$  depends on the jet algorithm. It can be 1 for the  $k_T$  algorithm, 0 for the Cambridge-Aachen and  $-1$  for the anti- $k_T$ . The latter is the one used in ATLAS. With the anti- $k_T$  algorithm,  $d_i = \frac{1}{(k_T^{(i)})^2}$  and  $d_{i,j} = \frac{1}{\max[(k_T^{(i)})^2; (k_T^{(j)})^2]} \left( \frac{\Delta R}{R} \right)^2$ . Jets are seeded by the hardest objects and the jets have a conical shape with radius  $R$ . In Figure 4.8, a representation of the algorithm is shown.

In this analysis, jets are selected using the anti- $k_T$  algorithm with a radius  $R = 0.4$ . Jets are also required to have  $p_T > 35$  GeV and  $|\eta| < 4.5$ . In order to reject forward jets originating by additional proton-proton interactions, a forward jet vertex tagger (fJVT) requirement is applied. All jets with  $|\eta| > 2.5$  must pass, in order to be selected, the requirements of the fJVT Medium WP, which has an efficiency of selecting hard scattered jets close to 97% and a pile-up jet efficiency of 53.4% for jets with  $40 \text{ GeV} < p_T < 50 \text{ GeV}$ .

---

<sup>2</sup> $\sigma_{noise,cell}^{EM} = \sqrt{(\sigma_{noise,cell}^{electronic})^2 + (\sigma_{noise,cell}^{pile-up})^2}$

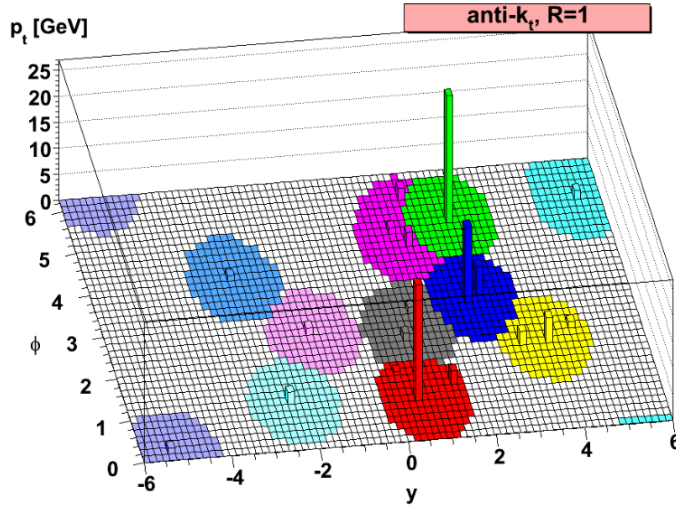


Figure 4.8: Representation of the anti- $k_T$  algorithm for jets reconstruction for a sample parton-level event with radius  $R = 1$  [50].

### b-Jets

*b*-Jets are very important in a *top* quark analysis, in that the *top* quark decays in a *b*-quark (Equation (2.1.1)) with a branching ratio close to unity. The bottom quark generates a jet because of the confinement. Confinement is caused by the *QCD* potential being linear, that is  $V(r) = kr$ . When a quark strays from another quark, their energy increases up to a point where it is convenient for the vacuum to generate a quark anti-quark pair in order to form bound states. This process is iterated for all the free quarks, and it leads to the so-called hadron shower. *b*-mesons and *b*-hadrons have a long life-time compared to the others ( $\tau \simeq 10^{-12}$  s), so the *b*-jet, that is a jet generated by the bottom quark, has a relatively long mean time decay length, which leads to measurably secondary vertices and impact parameters of the decay products, as can be seen in Figure 4.9.

The identification of *b*-jets is based on several objects reconstructed in the ATLAS detector, mainly the tracks, the vertices and the jet flavour label. Only tracks with  $p_T$  larger than 500 MeV are considered in the *b*-tagging algorithm. The efficiency of track reconstruction ranges from 91% in the inner region of the ID ( $|\eta| < 0.1$ ) down to 73% in the forward region ( $2.3 \leq |\eta| < 2.5$ ). The vertices are important for the *b*-tagging in that, as stated earlier, a *b*-jet differs from a light jet because it has two vertices.

Because of *b*-jets requiring track reconstruction, which takes place in the ID, the *b*-jets must have  $|\eta| < 2.5$ . The algorithm used for *b*-jets reconstruction is DL1R [51]. Pseudo-continuous *b*-tagging working points are used, with the different values for *b*-jet efficiency and  $c$ ,  $\tau$  and light jets rejection reported in Table 4.1.

Finally, jet flavour label is assigned to all simulated jets. Jets are labelled as *b*-jets if they are matched to at least one weakly decaying *b*-hadron with  $p_T \geq 5$  GeV within

Name	$b$ -jet efficiency (%)	$c$ -jet R	light-jet R	$\tau$ -jet R
<code>eff_60</code>	60.61	27	1495	314
<code>eff_70</code>	70.56	9	429	61
<code>eff_77</code>	77.50	4	141	17
<code>eff_85</code>	85.39	2	31	4

Table 4.1: Efficiency for  $b$ -jet reconstruction and rejection (R) corresponding to different  $b$ -tagging efficiency single-cut operating points for the DL1r algorithm, evaluated on  $t\bar{t}$  events [52].

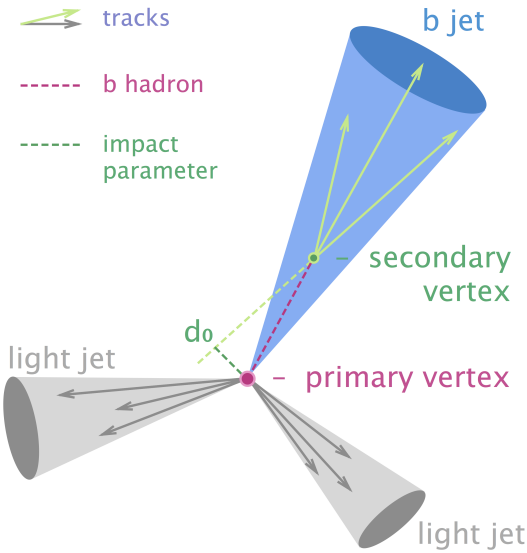


Figure 4.9: Schematic view of a  $b$ -hadron decay inside a jet coming from a secondary vertex, compared to light jets.

a cone of  $\Delta R = 0.3$  around the jet axis. If a  $b$ -hadron is not found, a  $c$ -hadron or  $\tau$ -leptons are searched. If one of them is found, the jet is labelled either as a  $c$ -jet or a  $\tau$ -jet. Otherwise, the jet is labelled as a light jet.

For this thesis, the `eff_70` and `eff_77` working points were used.

### Missing energy

Neutrinos do not interact with any of the detectors, so they can be reconstructed only using the difference between the initial state and final state total momentum. The initial transverse momentum is zero, so the final one has to be zero too. Candidate neutrinos are defined by missing transverse energy  $E_T^{miss} = \sqrt{(E_x^{miss})^2 + (E_y^{miss})^2}$ , and the two components are calculated as the magnitude of the negative vector sum of the transverse momentum of all the jets with  $p_T > 20$  GeV, all the leptons with  $p_T > 25$  GeV and a soft term built from tracks that are associated to the hard-scatter vertex, which are not associated to any of the reconstructed objects.

## 4.4 Event selection

The final state of the  $tZq$  process I am working on in this thesis is a trilepton channel. It consists of three charged leptons (two coming from a  $Z$  boson and one coming from the leptonic decay of the  $W$  boson), one neutrino, one  $b$ -quark (which leads to one  $b$ -jet) and one light quark. The final state can be seen in Figures 2.6, 2.7 and 4.3. The trilepton final state is the one with the lowest branching ratio, but it is the cleanest one. Therefore, it is the easiest channel to study.

The  $Z$  boson and the  $top$  quark must be reconstructed in order to differentiate the signal from some of the background sources. The  $Z$  boson mass distribution, for example, can be used to reduce the  $top$  quark backgrounds, because they do not have a  $Z$  boson in the final state.

The event selection used in the previous analysis [29] is reported in Table 4.3. Exactly three leptons (no hadronically-decaying  $\tau$ ) are required, with  $p_T(\ell_1) > 28$  GeV and  $p_T(\ell_{2,3}) > 20$  GeV. To reconstruct the leptons coming from the  $Z$  boson, an opposite-sign-same-flavour (OSSF) lepton pair is required. The lepton final states combinations are  $ee\mu$ ,  $e\mu\mu$ ,  $eee$  and  $\mu\mu\mu$ . In the first two cases it is obvious to reconstruct the OSSF pair, whereas in the other two, the OSSF pair is made of the two leptons with invariant mass closer to the mass of the  $Z$  boson (91 GeV). A limit on the invariant mass of the OSSF pair is set at 81 GeV, in order to avoid non-resonant OSSF lepton pairs.

Three signal regions were defined. The first two,  $2j1b$  and  $3j1b$ , are orthogonal, and are presented in Table 4.3. The  $2j1b$  region has a dijet final state with only one  $b$ -jet, whereas the  $3j1b$  region has a trijet final state with only one  $b$ -jet. The  $nj1b$  region is the inclusive region. It accepts a number of jets between 2 and 8, of which only one is a  $b$ -jet.

For the SR  $2j1b$  we define the  $b$ -jet  $j_b$  as the jet which was  $b$ -tagged and the forward jet  $j_f$  as the other jet. For the SR  $3j1b$ , the definition of the  $b$ -jet is the same as for  $2j1b$ . The forward and the radiation jets are defined respectively as the jet with the highest and the lowest invariant mass with the  $b$ -jet.

A summary of the symbols representing the reconstructed objects is presented in Table 4.2.

## 4.5 State of the art

The  $tZq$  process was observed in 2018 by both ATLAS and CMS [29]. This process is interesting for several reasons. Among those, it gives insights into the coupling between the  $Z$  boson and the top quark. Another reason is that this process is a background for the  $tHq$  production, one of the processes which allows to evaluate the Yukawa coupling between the Higgs boson and the top quark. The theoretical cross section for this process at  $\sqrt{s} = 13$  TeV at NLO is 102 fb. In 2018 [29], this cross section was

Symbol	Description
$\ell_1^Z$	Highest- $p_T$ lepton from the reconstructed $Z$ boson
$\ell_2^Z$	Lowest- $p_T$ lepton from the reconstructed $Z$ boson
$\ell^W$	Lepton from the reconstructed $W$ boson from the $t$ -quark decay
$Z$	Reconstructed $Z$ boson
$W$	Reconstructed $W$ boson
$j_b$	$b$ -tagged jet
$j_f$	Forward jet
$j_r$	Radiation jet
$\ell_{1,2,3}$	$p_T$ -ordered leptons
$j_{1,2,3}$	$p_T$ -ordered jets

Table 4.2: Summary on object reconstruction

measured with a 15% uncertainty, dominated by the statistics. The cross section at  $\sqrt{s} = 13$  TeV with  $139 \text{ fb}^{-1}$  of integrated luminosity is  $\sigma = 97 \pm 13(\text{stat.}) \pm 7(\text{syst.}) \text{ fb}$ .

The analysis now aims at improving the measurement of the inclusive cross section and at implementing the first measurement of the differential cross section. In order to do so, it is important to reduce the background and enhance the signal events.

## 4.6 Event selection optimisation

The aim of this thesis is to optimise the event selection for the  $tZq$  analysis, in order to help future measurements for this process. The aim is to increase the signal acceptance keeping the background contamination as low as possible. The optimisation focused on the following aspects: the choice of the isolation requirements for the leptons (Section 4.6.1), the tuning of the lepton  $p_T$  thresholds (Section 4.6.2), the efficiency of the  $b$ -tagging (Section 4.6.3) and the number of jets in the events (Section 4.6.4).

For the purpose of this analysis, the MC samples described in Section 4.2.2 were grouped, based on similar final states. I have merged  $t\bar{t}$  with  $tW$  into a  $t\bar{t} + tW$  sample,  $t\bar{t}Z$  with  $tWZ$  into a  $t\bar{t}Z + tWZ$  sample and  $t\bar{t}H$  with  $3t$  and  $t\bar{t}W$  into a  $t\bar{t}H + t\bar{t}W + 3t$  sample. Finally, the Diboson, Triboson and Electroweak  $VVjj$  samples were all merged into one sample, called Multiboson. A classification of Multiboson based on flavour tagging was also implemented. I have separated the Multiboson sample into three different samples, called Multiboson[ $LF$ ], Multiboson[ $HF$ ] +  $C$  and Multiboson[ $HF$ ] +  $B$ . The first sample contains events where all jets come from light quarks. The second one contains events where at least one jet originates from a  $c$ -quark, but none come from a  $b$ -quark. The latter contains events where at least one jet originates from a  $b$ -quark.

As much it is good to reduce the background, we can't completely eliminate it. If we want to do a multivariate analysis (NN or BDT), we must have both signal and

Common selections	
Exactly 3 leptons with $ \eta  < 2.5$ ( $e$ and $\mu$ )	
$p_T(\ell_1) > 28 \text{ GeV}$ , $p_T(\ell_2) > 20 \text{ GeV}$ , $p_T(\ell_3) > 20 \text{ GeV}$	
$p_T(\text{jet}) > 35 \text{ GeV}$	
$b$ -tagging efficiency: 70%	
SR 2j1b	SR 3j1b
exactly 1 OSSF pair	exactly 1 OSSF pair
$ m_{ll} - m_Z  < 10 \text{ GeV}$	$ m_{ll} - m_Z  < 10 \text{ GeV}$
2 jets, $ \eta  < 4.5$	3 jets, $ \eta  < 4.5$
1 $b$ -jet, $ \eta  < 2.5$	1 $b$ -jet $ \eta  < 2.5$

Table 4.3: Common selections used for the analysis

background in order to teach the NN how to distinguish them, and the NN cannot do that if there is no background. It is also important to keep a high number of events for the signal for the same reason.

Each event carries a statistically independent weight  $\omega_i$ ,  $i = 1, \dots, n$ . This weight takes into account the cross-section of the process, the integrated luminosity and all the MC/data correction factors from object identification, isolation and trigger requirements. The event yields are evaluated as  $\mu = \sum_{i=1}^n \omega_i$  and the statistical  $\sigma_\mu$  is defined as  $\sigma_\mu = \sqrt{\sum_{i=1}^n \omega_i^2}$  [53]. The uncertainties on the yields are only statistics.

#### 4.6.1 Lepton isolation requirements

Out of all the backgrounds,  $Z + \text{jets}$  and  $t\bar{t} + tW$  are the most important ones to reduce by means of an Isolation Working Point study, even though these backgrounds are not the highest (the Multiboson is). This samples have only two prompt leptons, but they enter the selection because of the presence of a third non-prompt lepton. I am going to refer to those two backgrounds as *fake*, and the first part of my analysis is going to be aimed at reducing those two backgrounds without cutting out too much of the signal. Prompt leptons are the ones coming from the decay of  $W$  and  $Z$  bosons. On the other hand, non-prompt leptons are the ones generated by the decay of hadrons from heavy quarks, which lead to jets. They can be distinguished because non-prompt leptons are not isolated, as they are part of a jet. Prompt leptons instead are found without high- $p_T$  tracks near them. The difference between prompt and non-prompt can be seen in Figure 4.12.

In this thesis I have analysed different Isolation Working Points (WPs) in order to find the WP which optimise the event selection of the signal process. Isolation WPs use a set of selections and cuts in order to identify the isolated objects. The Isolation WP combination used are shown in Table 4.4.

The isolation is made in two different ways. The first one is the one used by the

Name	Electrons	Muons
<i>Default</i>	Gradient	FCTight_TrackOnly_FixedRad
<i>PLV</i>	PLVTight	PLVTight
<i>PFlow</i>	PflowTight	PflowTight_VarRad
<i>TightTrack</i>	TightTrackOnly	TightTrackOnly_VarRad
<i>PLI</i>	PLImprovedTight	PLImprovedTight
<i>PLIV</i>	PLImprovedVeryTight	PLImprovedVeryTight

Table 4.4: List of the Isolation Working Point combinations used in the analysis. The *Name* column refers to the name I have used in the following plots and tables in order to describe the particular combination

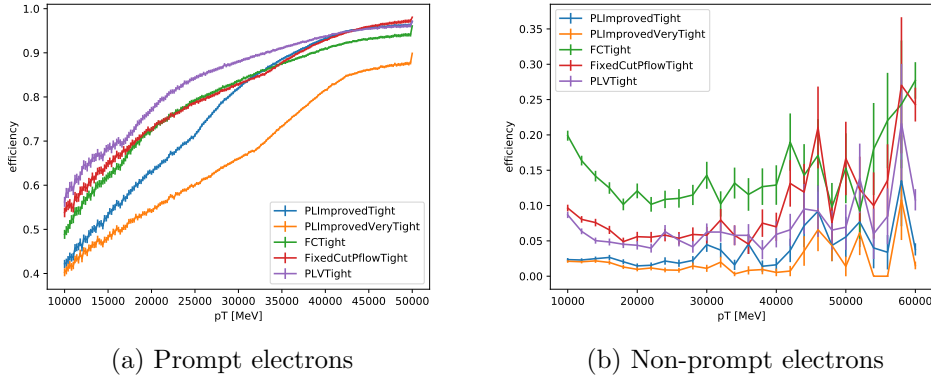


Figure 4.10: Efficiency for isolation of prompt (Figure 4.10(a)) and non-prompt (Figure 4.10(b)) electrons for different Isolation Working Points [54].

”standard” WPs, which are the ones in *Default*, *PFlow* and *TightTrack*. This WPs count the transverse momentum inside a cone centered on the track with the highest momentum. The cone can be either a fixed cone, that is a cone with fixed radius, or a variable cone, that is a cone with a smaller radius at high  $p_T$ . The lepton is considered isolated if the ratio between the sum of all the transverse momentum of the tracks inside the cone and the lepton  $p_T$  is lower than a given threshold. If the momentum inside a cone is similar to the momentum of the lepton, it means that the lepton is isolated, because it has no tracks near it. If there is a lot of momentum inside the cone not being carried by the lepton it means that there are other particles near the lepton. Therefore, the lepton is not isolated and it is a non-prompt one.

On the other hand, the *PLV* WPs, which are *PLVTight*, *PLImprovedTight* and *PLImprovedVeryTight* use the *Prompt Lepton Veto* algorithm for isolation. This algorithm uses, in addition to the counting of the momentum inside the cone, a MVA in order to identify prompt leptons. The MVA uses additional variables, such as number of tracks in the cone, lifetime information associated with the track jet that matches the selected lepton and  $\Delta R$  between the lepton and track jet axis. The use of a MVA

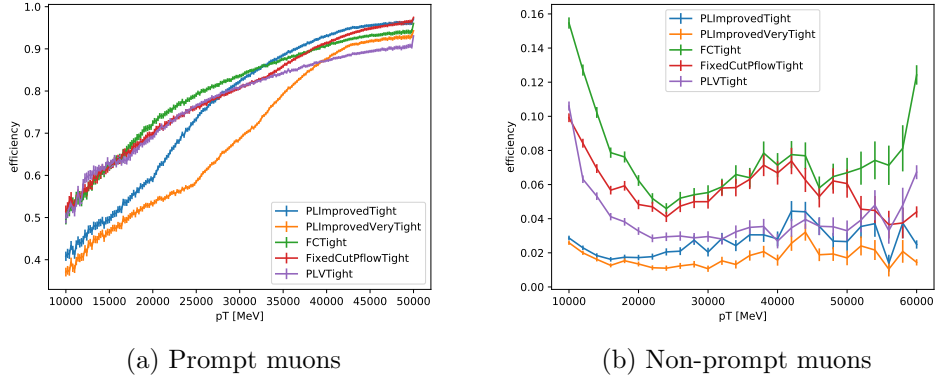


Figure 4.11: Efficiency for isolation of prompt (Figure 4.10(a)) and non-prompt (Figure 4.10(b)) muons for different Isolation Working Points [55].

allows for a higher rejection of non-prompt background even at low- $p_T$ , at the cost of losing signal efficiency. A higher rejection of non-prompt leptons means less fake background.

## Default

The *Default* selection consists of using the `FCTight_TrackOnly_FixedRad` WP for muons and `Gradient` WP for electrons. It is called *Default* because it is the most similar combination of WPs used in the analysis [29], where `Gradient` was used for both electrons and muons. We changed the muon WP because `Gradient` was not available any more for the v32 ntuples, which are the ones I used. This selection was also used to check if the code used for the analysis worked. To verify that, the event yields for this selection were compared to the yields of the previous analysis [29].

The `Gradient` WP has a 90% efficiency of identifying a prompt lepton with  $p_T = 25$  GeV. The efficiency of misidentifying a non-prompt lepton with  $p_T = 25$  GeV is 20%. The `FCTight_TrackOnly_FixedRad` WP requires that  $p_T^{\text{varcone},30}/p_T^\mu < 0.06$ <sup>3</sup> for  $p_T^\mu < 50$  GeV and  $p_T^{\text{cone},20}/p_T^\mu < 0.06$ <sup>4</sup> for  $p_T^\mu > 50$  GeV [56]. The latter considers the events inside a cone with a fixed value of radius, whereas the former considers a cone whose radio is 0.3 if  $p_T^\mu < 33$  GeV, otherwise it is  $\Delta R = \frac{10 \text{ GeV}}{p_T^\mu}$ . For high- $p_T$  muons ( $p_T > 50$  GeV) we use the cone instead of the varcone in order to have a wider cone. This allows us to have a better background rejection.

The event yields for both  $2j1b$  and  $3j1b$  SR are presented in Table 4.5.

I compared these yields with those from the old analysis [29] and we find, as expected, a good comparison. The small differences are due to the fact that, even though they are similar, the lepton Isolation Working Points used were different. My

<sup>3</sup>  $p_T^{\text{varcone},30}$  is the transverse momentum of all tracks inside a cone with  $\Delta R = \min(0.3, \frac{10 \text{ GeV}}{p_T^\mu})$

<sup>4</sup>  $p_T^{\text{cone},20}$  is the transverse momentum of all tracks inside a cone with  $\Delta R = 0.2$

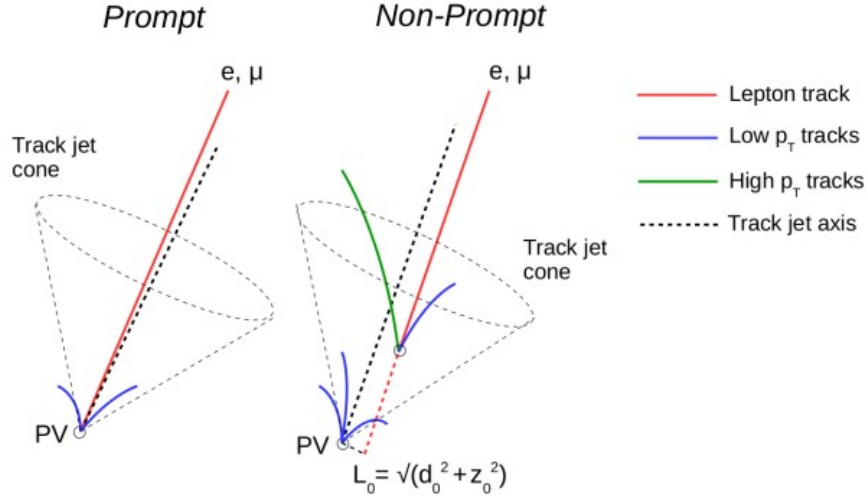


Figure 4.12: Comparison between prompt and non-prompt leptons

analysis also used few different MC samples compared to the previous one, so that could account too for the small discrepancy. I expected a total of  $327 \pm 2.3$  events and I found  $317.8 \pm 5.5$ . The percentages of  $t\bar{t}lq$  are comparable.

I have also brought my attention to the number of leptons for each sample. I want a trilepton final state, so there are four possible combinations of leptons ( $eee$ ,  $\mu\mu\mu$ ,  $ee\mu$ ,  $e\mu\mu$ ). The goal was to see if one of the combinations could maximise the signal and minimise the fake background. The results are presented in Table 4.6 for  $2j1b$  and in Table 4.7 for  $3j1b$ , and it can be seen that the tri-electron final state suppresses a lot more the fake background than it does to the signal. For  $2j1b$ , the number of signal events with three electrons is  $1/3$  of the number of events with three muons, whereas for  $t\bar{t}$  that number goes down to  $1/20$ . Another thing that can be easily noted is that there are more muons than there are electrons. This is not due to muons being more present in the process, because the lepton universality is still valid, but it happens because the efficiency of identification is higher for muons than it is for electrons, as explained in Section 4.3. So, this result must not be taken as some kind of confirmation of the violation of lepton universality.

Although this selection shows a good signal/background ratio (measured as  $S/\sqrt{B}$  or  $S/\sqrt{B+S}$ ), the percentage of the fake background is too high.

## Pflow

The *Pflow* selection consists of using `PflowTight` for electrons and `PflowTight_VarRad` for muons.

The `PflowTight` WP reconstructs electrons with  $p_T = 25$  GeV with a 75%

<i>Default</i>	<i>2j1b</i>	<i>3j1b</i>
<i>tllq</i>	$89.5 \pm 0.7$	$51.0 \pm 0.5$
<i>t̄t + tW</i>	$33.6 \pm 1.2$	$13.8 \pm 0.8$
<i>Z + jets</i>	$15.0 \pm 1.2$	$7.8 \pm 1.4$
Multiboson[ <i>LF</i> ]	$6.6 \pm 0.2$	$3.7 \pm 0.1$
Multiboson[ <i>HF</i> ] + <i>B</i>	$53.2 \pm 0.6$	$33.0 \pm 0.4$
Multiboson[ <i>HF</i> ] + <i>C</i>	$37.4 \pm 0.6$	$20.2 \pm 0.4$
<i>t̄tZ + tWZ</i>	$76.2 \pm 0.8$	$117.6 \pm 0.9$
<i>t̄tH + t̄tW + 3t</i>	$6.4 \pm 0.2$	$4.8 \pm 0.1$
Total	$317.8 \pm 5.5$	$251.7 \pm 4.7$
<i>S/√B</i>	5.92	3.59
<i>S/√B + S</i>	5.02	3.21
% <i>tllq</i>	28.02	20.25
% <i>t̄t + tW</i>	10.59	5.48
% <i>Z+jets</i>	4.71	2.62

Table 4.5: Event yields using *Default* selection

<i>2j1b</i>		<i>Default</i>		
Sample		<i>eee</i>	<i>eeμ</i>	<i>eμμ</i>
<i>tllq</i>		12.1	17.4	24.3
<i>t̄t + tW</i>		0.9	4.7	9.6
<i>Z + jets</i>		0.7	4.9	1.0
Multiboson		15.4	18.6	27.5
<i>t̄tZ + tWZ</i>		11.7	16.0	19.4
<i>t̄tH + t̄tW + 3t</i>		0.8	1.3	1.8

Table 4.6: Number of different leptons combinations using *Default* selection

efficiency, much less than **Gradient**. I expect to have less events than the *Default* selection. Fake electrons with  $p_T = 25$  GeV are identified with a 8% efficiency, so I

<i>3j1b</i>		<i>Default</i>		
Sample		<i>eee</i>	<i>eeμ</i>	<i>eμμ</i>
<i>tllq</i>		7.2	10.0	14.0
<i>t̄t + tW</i>		0.7	2.2	3.8
<i>Z + jets</i>		0.2	1.9	0.4
Multiboson		8.9	11.2	15.9
<i>t̄tZ + tWZ</i>		17.8	25.0	30.9
<i>t̄tH + t̄tW + 3t</i>		0.7	0.8	1.4

Table 4.7: Number of different leptons combinations using *Default* selection

<i>Pflow</i>	2j1b	3j1b
$tllq$	$80.0 \pm 0.6$	$45.9 \pm 0.5$
$t\bar{t} + tW$	$10.6 \pm 0.7$	$5.0 \pm 0.5$
$Z + jets$	$5.3 \pm 0.8$	$1.9 \pm 0.2$
Multiboson[ <i>LF</i> ]	$6.0 \pm 0.2$	$3.4 \pm 0.1$
Multiboson[ <i>HF</i> ] + <i>B</i>	$49.0 \pm 0.6$	$30.1 \pm 0.4$
Multiboson[ <i>HF</i> ] + <i>C</i>	$34.1 \pm 0.6$	$18.4 \pm 0.4$
$t\bar{t}Z + tWZ$	$69.1 \pm 0.7$	$107.2 \pm 0.9$
$t\bar{t}H + t\bar{t}W + 3t$	$5.6 \pm 0.2$	$4.2 \pm 0.1$
Total	$259.7 \pm 4.4$	$216.0 \pm 3.1$
$S/\sqrt{B}$	5.97	3.51
$S/\sqrt{B+S}$	4.96	3.19
% $tllq$	30.80	22.15
% $t\bar{t} + tW$	4.08	2.31
% $Z+jets$	2.04	0.88

Table 4.8: Event yields using *Pflow* selection

also expect lower fake yields than *Default*, which has a 20% efficiency. For muons with  $p_T$  between 20 and 100 GeV the efficiency is 87% for prompt and 0.9% for non-prompt. As for *Default*, the discriminant variable for isolation is the transverse momentum inside a cone. We consider an electron (with **PflowTight** WP) or a muon (with **PflowTight\_VarRad**) isolated if  $p_T^{\text{varcone},30}/p_T < 0.045$ . It can be noted that the requirement is tighter than it is for *Default*.

The yields are presented in Table 4.8. This selection looks promising for both 2j1b and 3j1b because it is similar to *Default* in the signal/background ratios and it cuts a huge amount of the fakes. The signal is reduced by less than the fake backgrounds are, and the signal/background ratios are comparable.

Because of the fake background being so little, the analysis on the number of leptons did not give useful information, because there is not enough statistics.

### TightTrack

The *TightTrack* selection consists of using **TightTrackOnly\_VarRad** for muons and **TightTrackOnly** for electrons.

The **TightTrackOnly** WP has a 85% efficiency of reconstructing a prompt electron and a 15% efficiency of identifying non-prompt ones. The **TightTrackOnly\_VarRad** WP instead has a 94% efficiency for prompt muons and a 3.2% efficiency for non-prompt muons in the 20 – 100 GeV range. Both electrons and muons are considered isolated if  $p_T^{\text{varcone},30}/p_T < 0.06$ , which is the same requirement as **FCTight\_TrackOnly\_FixedRad** (*Default* selection) for  $p_T < 50$  GeV and it is looser than *Pflow*.

The yields for the *TightTrack* selection are in Table 4.9. This selection allows for

<i>TightTrack</i>	<i>2j1b</i>	<i>3j1b</i>
<i>tllq</i>	$92.7 \pm 0.7$	$52.7 \pm 0.6$
<i>t̄t + tW</i>	$36.0 \pm 1.2$	$14.7 \pm 0.8$
<i>Z + jets</i>	$15.9 \pm 1.2$	$8.3 \pm 1.4$
Multiboson[ <i>LF</i> ]	$6.8 \pm 0.2$	$3.7 \pm 0.1$
Multiboson[ <i>HF</i> ] + <i>B</i>	$54.9 \pm 0.6$	$34.1 \pm 0.4$
Multiboson[ <i>HF</i> ] + <i>C</i>	$38.8 \pm 0.6$	$20.8 \pm 0.4$
<i>t̄tZ + tWZ</i>	$79.4 \pm 0.8$	$122.5 \pm 0.9$
<i>t̄tH + t̄tW + 3t</i>	$6.7 \pm 0.2$	$5.0 \pm 0.1$
Total	$331.2 \pm 5.6$	$261.9 \pm 4.7$
<i>S/√B</i>	6.05	3.64
<i>S/√B + S</i>	5.09	3.26
% <i>tllq</i>	27.99	20.12
% <i>t̄t + tW</i>	10.86	5.60
% <i>Z+jets</i>	4.79	3.18

Table 4.9: Event yields using *TightTrack* selection

more signal events than *Default* (93 against 90 for *2j1b*), but at the cost of increasing *t̄t + tW* by the same amount. For *3j1b* the signal and both fake backgrounds increase by the same amount. For both SRs the signal to background ratio (*S/√B* and *S/√B + S*) is higher than it is for *Default* but the percentage of the signal is a little lower. I have also noticed that this selection allows for more fakes than *Pflow*, but it has more signal to compensate for. The signal/background ratios are higher than *Pflow* in both SRs.

For this selection I have analysed the number of leptons for each sample as well and I noticed a 93% decrease in the fake backgrounds going from  $\mu\mu\mu$  to  $eee$  compared to only a 63% decrease in the signal. This result reflects what we have seen for the *Default* selection.

## PLV

The *PLV* selection consists of using *PLVTight* for both electrons and muons. *PLV* is short for *Prompt Lepton Veto*. The Prompt Lepton tagging algorithm matches electrons and muons to track jets, in order to select the prompt leptons and reject the non-prompt ones.

As described earlier, The *Prompt Lepton Veto* algorithm was built in order to reject more non-prompt leptons than other IWPs. The background rejection is close to 98% for electrons and 99% for muons. The *Prompt Lepton Veto* uses both MVA, as described earlier and a *varcone*, with the restraint  $p_T^{\text{varcone},30}/p_T < 0.016$ .

The yields are presented in Table 4.10. As expected, all the samples but the Multiboson show a decrease in number when compared to the previous selections. The signal event number decreases a little, however the percentage of the signal increases.

<i>PLV</i>	<i>2j1b</i>	<i>3j1b</i>
<i>tllq</i>	$83.8 \pm 0.6$	$47.7 \pm 0.5$
$t\bar{t} + tW$	$8.8 \pm 0.6$	$4.3 \pm 0.4$
$Z + jets$	$4.7 \pm 0.7$	$2.0 \pm 0.3$
Multiboson[ <i>LF</i> ]	$6.2 \pm 0.2$	$3.3 \pm 0.1$
Multiboson[ <i>HF</i> ] + <i>B</i>	$49.6 \pm 0.6$	$30.8 \pm 0.4$
Multiboson[ <i>HF</i> ] + <i>C</i>	$34.8 \pm 0.6$	$18.9 \pm 0.4$
$t\bar{t}Z + tWZ$	$71.9 \pm 0.7$	$110.8 \pm 0.9$
$t\bar{t}W + t\bar{t}H + 3t$	$5.7 \pm 0.2$	$4.3 \pm 0.1$
Total	$265.6 \pm 4.3$	$222.2 \pm 3.1$
$S/\sqrt{B}$	6.37	3.61
$S/\sqrt{B+S}$	5.23	3.20
% <i>tllq</i>	31.56	21.47
% $t\bar{t} + tW$	3.33	1.93
% $Z+jets$	1.83	0.91

Table 4.10: Event yields using *PLV* selection

Fake background yields drop by almost 80% from *Default* and *TightTrack* for both SRs. The signal to background ratios are the highest for *2j1b* and are few less than *TightTrack* for *3j1b*.

The analysis on the leptons shows results similar to the ones obtained from previous selections, but because of the statistics being so little (especially for  $Z+jets$ ) those results are statistically irrelevant. An example is  $Z+jets$  in *3j1b* region where we have 0.6 events with a trimuon final state and 0.3 events with trielectron final state.

## PLI

The *PLI* selection consists of using `PLImprovedTight` for both electrons and muons. `PLImprovedTight` (*Prompt Lepton Veto Improved Tight*) is the improved version of `PLVTight`, implemented in the ntuples' version v32. Figures 4.10(a) and 4.11(a) show how this WP works compared to the older version (*PLV*). *PLI* has a lower efficiency on identification of prompt leptons, so I expect to have less signal than *PLV* and the other looser Working Points (*Default*, *TightTrack* and *Pflow*). The efficiency of identification of a prompt lepton with  $p_T = 25$  GeV (which is the peak in the distribution of  $p_T(\ell^W)$ , chosen because  $\ell^W$  is the lepton mostly misidentified as a prompt lepton) is 70% for electrons and 73% for muons, less than *PLV* (83% for electrons and 75% for muons). The gain in using `PLImprovedTight` instead of `PLVTight` is in the fake background rejection. From Figures 4.10(b) and 4.11(b) it can be seen that the efficiency of identifying a non-prompt electron is 2.5% for `PLImprovedTight` compared to 6.5% for `PLVTight` and for muons it is 2% for `PLImprovedTight` and 3.5% for `PLVTight`. This means that I expect to have a lot fewer fake backgrounds than I do with the

<i>PLI</i>	<i>2j1b</i>	<i>3j1b</i>
<i>tllq</i>	$80.7 \pm 0.6$	$46.1 \pm 0.5$
<i>t̄t + tW</i>	$5.1 \pm 0.5$	$3.5 \pm 0.4$
<i>Z + jets</i>	$2.8 \pm 0.6$	$0.9 \pm 0.2$
Multiboson[ <i>LF</i> ]	$6.1 \pm 0.2$	$3.3 \pm 0.1$
Multiboson[ <i>HF</i> ] + <i>B</i>	$48.7 \pm 0.6$	$30.4 \pm 0.4$
Multiboson[ <i>HF</i> ] + <i>C</i>	$34.1 \pm 0.6$	$18.7 \pm 0.4$
<i>t̄tZ + tWZ</i>	$69.3 \pm 0.7$	$107.0 \pm 0.9$
<i>t̄tH + t̄tW + 3t</i>	$5.7 \pm 0.2$	$4.2 \pm 0.1$
Total	$252.5 \pm 4.0$	$214.2 \pm 3.0$
<i>S/√B</i>	6.16	3.55
<i>S/√B + S</i>	5.08	3.15
% <i>tllq</i>	32.0	21.52
% <i>t̄t + tW</i>	2.02	1.63
% <i>Z+jets</i>	1.11	0.42

Table 4.11: Event yields using *PLI* selection

previuos selections.

Table 4.11 shows the yields using this selection. Those yields meet my expectations, because we see a small decrease in the signal which is matched with an evenly decrease in the fake backgrounds. For SR *3j1b* *Z+jets* becomes almost negligible (0.9 events). The percentage of signal is on average equal to that of *PLV* (a little lower for *2j1b* and a little higher for *3j1b*), however the percentage of fakes is halved for all but *t̄t 3j1b*. Signal to background ratio for SR *2j1b* is lower only than *PLV*, instead SR *3j1b* is the lowest out of all the selections tested.

The Multiboson samples yields are almost identical to the ones for *PLV*, whereas the two remaining samples (*t̄tZ + tWZ* and *t̄tW + t̄tH + 3t*) have less events than *PLV*.

The analysis on the leptons showed the same results as *PLV*, because of the fake background being almost negligible.

## PLIV

The *PLIV* selection consists of using `PLImprovedVeryTight` for both electrons and muons. As well as `PLImprovedTight`, `PLImprovedVeryTight` (*Prompt Lepton Veto Improved Very Tight*) was implemented in the ntuples' version v32 as an even tighter Isolation Working Point than `PLImprovedTight`. A tighter WP means less efficiency in identification of both prompt leptons, which means less signal, and non-prompt lepton, which means less fake background. This Working Point is the one with the lowest efficiency out of the ones in Figures 4.10 and 4.11, with a 55% efficiency in identifying prompt electrons and muons and less than 2% efficiency for non-prompt leptons (both electrons and muons) with  $p_T = 25$  GeV.

<i>PLIV</i>	<i>2j1b</i>	<i>3j1b</i>
<i>tllq</i>	$66.5 \pm 0.6$	$38.3 \pm 0.5$
$t\bar{t} + tW$	$2.9 \pm 0.3$	$1.8 \pm 0.3$
$Z + jets$	$1.8 \pm 0.6$	$0.4 \pm 0.1$
$VV(V)[LF]$	$5.2 \pm 0.2$	$2.9 \pm 0.1$
$VV(V)[HF] + B$	$41.2 \pm 0.5$	$26.0 \pm 0.4$
$VV(V)[HF] + C$	$28.3 \pm 0.5$	$15.8 \pm 0.3$
$t\bar{t}Z + tWZ$	$57.0 \pm 0.7$	$88.9 \pm 0.8$
$t\bar{t}H + t\bar{t}W + 3t$	$4.5 \pm 0.2$	$3.3 \pm 0.1$
Total	$207.4 \pm 3.5$	$177.4 \pm 2.6$
$S/\sqrt{B}$	5.60	3.24
$S/\sqrt{B+S}$	4.62	2.88
% <i>tllq</i>	32.06	21.59
% $t\bar{t} + tW$	1.4	1.01
% $Z+jets$	0.88	0.23

Table 4.12: Event yields using *PLIV* selection

Table 4.12 shows the yields. I notice again a decrease in the signal yields matched with a halving of the fake backgrounds. The percentage of signal is a little lower than *PLV* but higher than it is for *PLI*. On the other hand, the signal to background ratios are the lowest out of all the selections.

As opposed to *PLI*, the yields for the Multiboson decrease significantly when compared to *PLV* and *PLI*. The same decrease is observed in  $t\bar{t}Z + tWZ$  and  $t\bar{t}W + t\bar{t}H + 3t$ .

The lepton analysis gave statistically irrelevant results, because of the yields for the fake background being so little.

## Conclusions

Figures 4.13 and 4.14 show the percentages of the samples for the different WP combinations analysed for both SRs. The summary for all the selections tested is in Table 4.13. I used the five parameters in the table to determine which was the better selection to use, both for *2j1b* and *3j1b*, keeping in mind that the aim was to reduce mostly the fake backgrounds. The three most prominent selections are *PLV*, *PLI* and *PLIV*. The *Default* selection had, as expected, too much of the fake background. *Pflow* and *TightTrack* show slightly better results than *Default*, but they retain too much of the fake background. *PLV* and *PLI* have very similar results, whereas *PLIV* has a lot of the signal cut out and it leaves too little of the fake backgrounds to be used in a multivariate analysis. But as far as reducing the fake backgrounds, *PLIV* works very well. Out of the three, *PLV* seems to be the best, with *PLIV* being the worst because it cuts too much of the signal. This hypothesis will be verified using different cuts on

SR		<i>Default</i>	<i>Pflow</i>	<i>TightTrack</i>	<i>PLV</i>	<i>PLI</i>	<i>PLIV</i>
<i>2j1b</i>	$S/\sqrt{B}$	5.92	5.97	6.05	6.37	6.16	5.60
	$S/\sqrt{B+S}$	5.02	4.96	5.09	5.23	5.08	4.62
	$tllq$	$89.5 \pm 0.7$	$80.0 \pm 0.6$	$92.7 \pm 0.7$	$83.8 \pm 0.6$	$80.7 \pm 0.6$	$66.5 \pm 0.6$
	$t\bar{t} + tW$	$33.6 \pm 1.2$	$10.6 \pm 0.7$	$36.0 \pm 1.2$	$8.8 \pm 0.6$	$5.1 \pm 0.5$	$2.9 \pm 0.3$
	$Z+jets$	$15.0 \pm 1.2$	$5.3 \pm 0.8$	$15.9 \pm 1.2$	$4.7 \pm 0.7$	$2.8 \pm 0.6$	$1.8 \pm 0.6$
<i>3j1b</i>	$S/\sqrt{B}$	3.59	3.51	3.64	3.61	3.55	3.24
	$S/\sqrt{B+S}$	3.21	3.19	3.26	3.20	3.15	2.88
	$tllq$	$51.0 \pm 0.5$	$45.9 \pm 0.5$	$52.7 \pm 0.6$	$47.7 \pm 0.5$	$46.1 \pm 0.5$	$38.3 \pm 0.5$
	$t\bar{t} + tW$	$13.8 \pm 0.8$	$5.0 \pm 0.5$	$14.7 \pm 0.8$	$4.3 \pm 0.4$	$3.5 \pm 0.4$	$1.8 \pm 0.3$
	$Z+jets$	$7.8 \pm 1.4$	$1.9 \pm 0.2$	$8.3 \pm 1.4$	$2.0 \pm 0.3$	$0.9 \pm 0.2$	$0.4 \pm 0.1$

Table 4.13: Results for all the selections

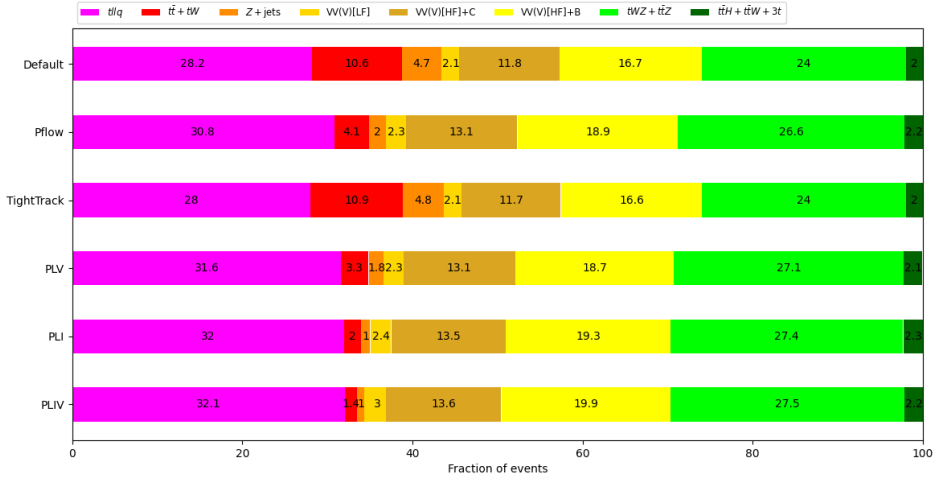


Figure 4.13: Summary of the fractions of various samples for all the different WP combinations tested using the common selections (Table 4.3) for SR 2j1b.

the leptons  $p_T$ .

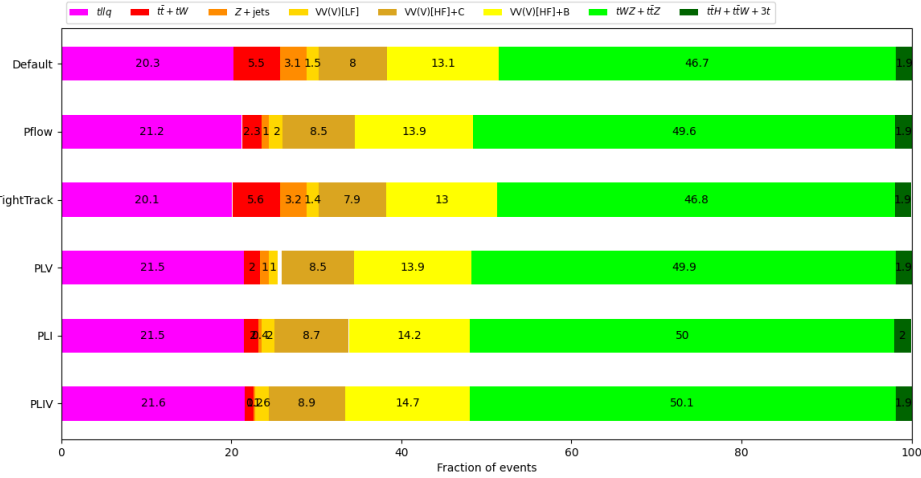


Figure 4.14: Summary of the fractions of various samples for all the different WP combinations tested using the common selections (Table 4.3) for SR 3j1b.

#### 4.6.2 Lepton $p_T$ requirements

When analysing the distributions (Figure 4.15) for the transverse momentum of the second and third lepton I noticed that a lot of signal was lost using a 20 GeV cut on both sub-leading leptons. Both leptons had a high number of signal events in the bin going from 20 to 30 GeV, which led me to think that applying the cut on a lower value of the transverse momentum could give more signal events without increasing too much the background. The graphs for the third lepton (right pictures in Figure 4.15) show clearly that more signal events can be found, because the lowest- $p_T$  bin contains the peak in the distribution.

Having chosen *PLV*, *PLI* and *PLIV* as the best IWPs, I decided to apply different cuts on the  $p_T$  of both second and third leptons on those selections. I tested three other combinations, which are reported in Table 4.14. In the following I will be showing the yields for all the selections only for *PLV*. For *PLI* and *PLIV* I will be showing only the information regarding the yields for the signal and the fakes, alongside the signal/background ratio. The selections used for this analysis are the ones described in Table 4.3, with the exception of the minimum  $p_T$  of the leptons.

In the previous analysis [29] a similar attempt was made, but when the 28-20-15 GeV cuts were applied on the *Default* selection, the number of fake backgrounds, especially  $Z+jets$ , increased too much. This is due to the fact that **Gradient** works fine for isolating high- $p_T$  leptons, but it fails on isolating low- $p_T$  ones. I present only a plot (Figure 4.16) which shows the comparison between a 28-20-20 GeV and a 28-20-15 GeV cut on leptons  $p_T$ , which illustrates the increase in the backgrounds in the lowest- $p_T$  bin. The fake yields increase from 48 to 78, with the  $Z+jets$  sample doubling its yields (from 15.7 to 29.7). The signal instead increases only by 20 events; therefore,

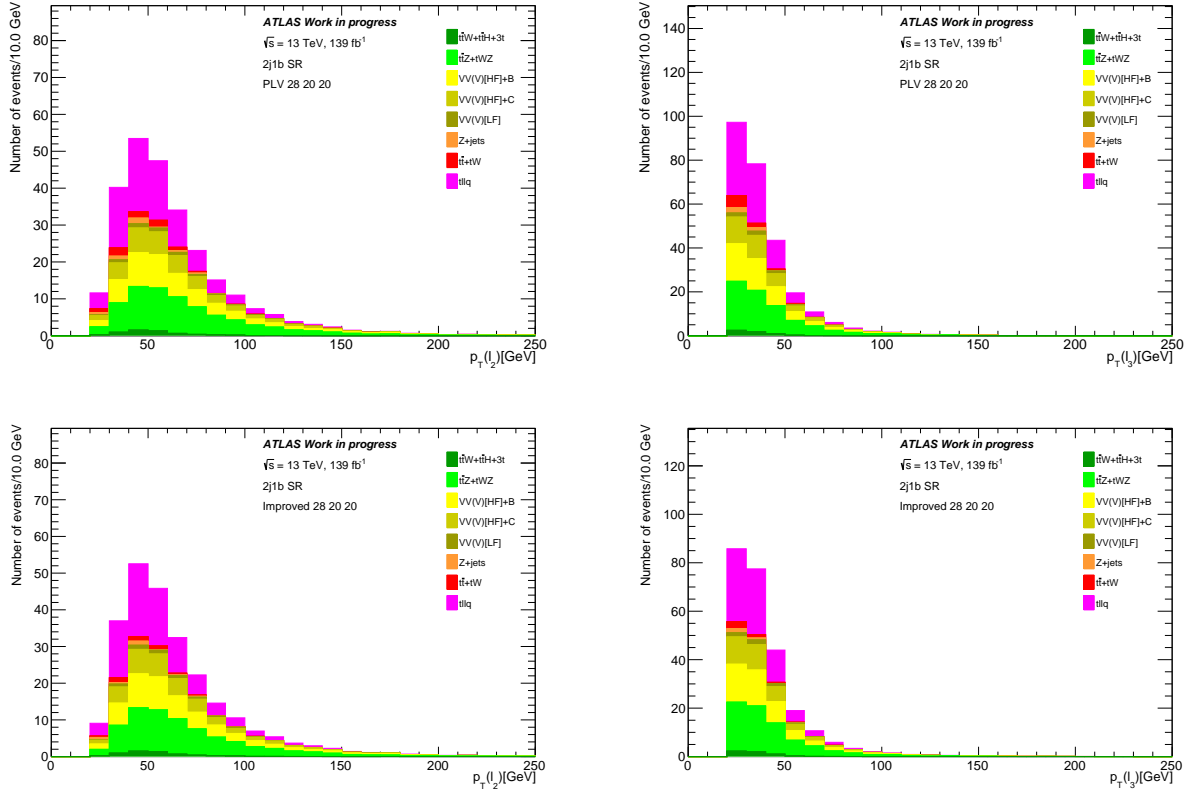


Figure 4.15: Plots for  $p_T$  of second (left) and third (right) lepton using  $PLV$ (top) and  $PLI$  (bottom) for SR  $2j1b$ .

its percentage is smaller ( $\sim 26\%$ ).

Since I am analysing the WPs which has the lowest number of fakes, I won't be talking about the analysis on the number of leptons, because for all of them the statistic is too little to gain useful information.

### 28-20-15

First, I applied a lower cut on the third lepton  $p_T$ , because, by looking at the distributions in Figure 4.15 it was possible to see that, potentially, we were missing out on a lot of signal events by cutting it to 20 GeV. I lowered the threshold to 15 GeV, without

Name	$p_T(\ell_1)$ [GeV]	$p_T(\ell_2)$ [GeV]	$p_T(\ell_3)$ [GeV]
28-20-15	28	20	15
28-20-10	28	20	10
28-15-15	28	15	15

Table 4.14: Different combinations of lepton  $p_T$  tested for  $PLV$ ,  $PLI$  and  $PLIV$ .

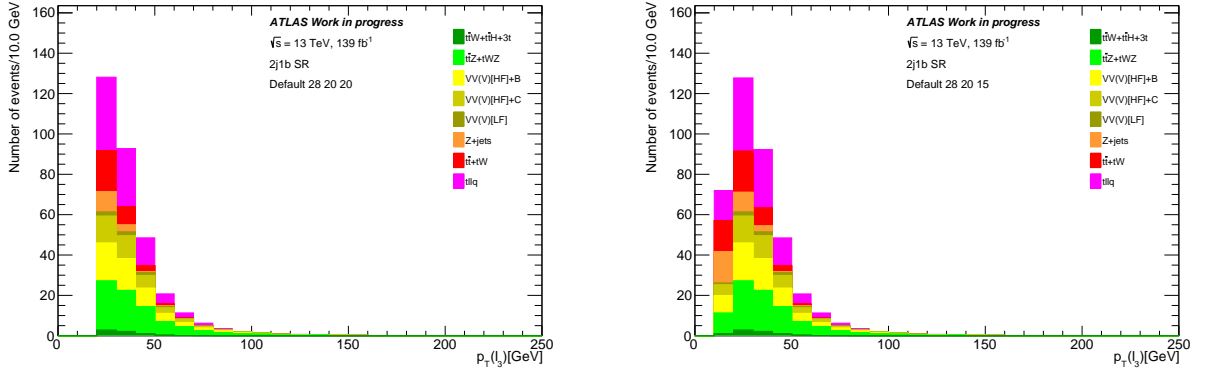


Figure 4.16: Comparison between a 28-20-20 (left) and a 28-20-15 (right) cut on lepton  $p_T$  for *Default* selection in SR 2j1b.

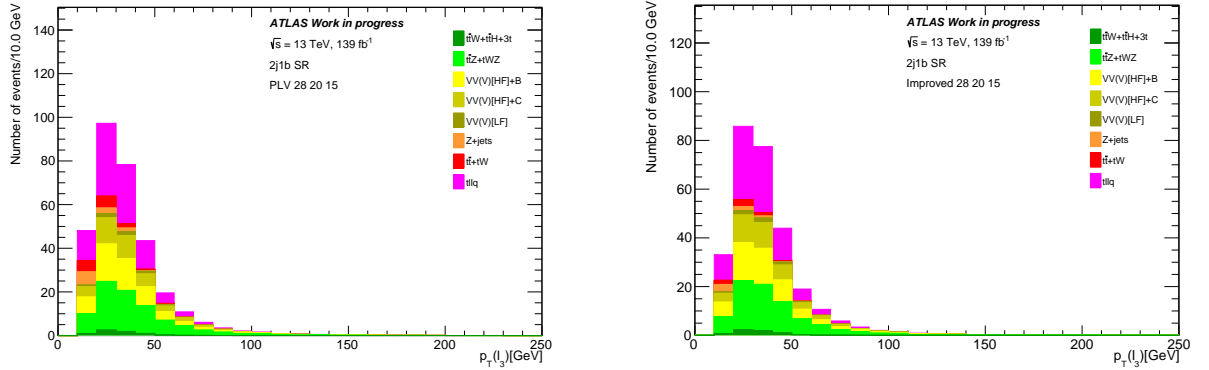


Figure 4.17: Plots for  $p_T$  of third lepton using *PLV* (left) and *PLI* (right) for SR 2j1b.

changing the threshold to the other two.

In Table 4.15 the event yields for *PLV* (28-20-15) are presented. We can see how, as expected, we gain a lot of the signal (almost 14 events for 2j1b and almost eight events for 3j1b) when compared to the 28-20-20 GeV selection (4.10). The fraction of the signal, however, decreases. On the other hand, the fakes increase in both number and fraction. However, the signal/background ratios are higher than the ones in Table 4.10.

Table 4.16 shows the results for all the three different WPs analysed. The results are similar to the ones obtained using a 20 GeV cut on the third lepton (Table 4.13): *PLV* has the best ratios and highest numbers. However, the signal fractions of *PLV* are the lowest, with *PLIV* being the one with highest fraction of signal and lowest fraction of fake backgrounds.

<i>PLV (28-20-15)</i>	<i>2j1b</i>	<i>3j1b</i>
<i>tllq</i>	$97.5 \pm 0.7$	$55.1 \pm 0.6$
<i>t̄t + tW</i>	$14.1 \pm 0.7$	$6.7 \pm 0.5$
<i>Z+jets</i>	$10.7 \pm 1.8$	$3.5 \pm 0.6$
Multiboson[ <i>LF</i> ]	$7.0 \pm 0.2$	$3.7 \pm 0.1$
Multiboson[ <i>HF</i> ] + <i>B</i>	$57.2 \pm 0.6$	$34.9 \pm 0.4$
Multiboson[ <i>HF</i> ] + <i>C</i>	$39.4 \pm 0.6$	$21.6 \pm 0.4$
<i>t̄tZ + tWZ</i>	$81.1 \pm 0.8$	$124.1 \pm 1.0$
<i>t̄tH + t̄tW + 3t</i>	$6.6 \pm 0.2$	$5.0 \pm 0.1$
Total	$313.6 \pm 5.7$	$254.7 \pm 3.7$
<i>S/√B</i>	6.63	3.90
<i>S/√(B + S)</i>	5.51	3.45
% <i>tllq</i>	31.09	21.63
% <i>t̄t + tW</i>	4.50	2.63
% <i>Z+jets</i>	3.32	1.37

Table 4.15: Event yields using *PLV(28-20-15)* selection

SR	<i>28-20-15</i>	<i>PLV</i>	<i>PLI</i>	<i>PLIV</i>
<i>2j1b</i>	<i>S/√B</i>	6.63	6.55	5.95
	<i>S/√(B + S)</i>	5.51	5.39	4.90
	<i>tllq</i>	$97.5 \pm 0.7$	$91.2 \pm 0.7$	$75.0 \pm 0.6$
	<i>t̄t + tW</i>	$14.1 \pm 0.7$	$6.8 \pm 0.5$	$4.0 \pm 0.4$
	<i>Z+jets</i>	$10.7 \pm 1.8$	$5.9 \pm 1.0$	$4.0 \pm 0.9$
<i>3j1b</i>	<i>S/√B</i>	3.90	3.79	3.46
	<i>S/√(B + S)</i>	3.45	3.35	3.06
	<i>tllq</i>	$55.1 \pm 0.6$	$51.7 \pm 0.5$	$42.9 \pm 0.5$
	<i>t̄t + tW</i>	$6.7 \pm 0.5$	$4.6 \pm 0.5$	$2.5 \pm 0.3$
	<i>Z+jets</i>	$3.5 \pm 0.6$	$1.5 \pm 0.4$	$0.8 \pm 0.3$

Table 4.16: Results for all the WPs analysed with a *28-20-15* cut on the leptons  $p_T$

**28-20-10**

The plots in Figure 4.17 show that, with a threshold selection of 28-20-15 GeV, in the lowest- $p_T$  bin the amount of signal is higher than the number of fakes. So, I expect that lowering even more the cut on the  $p_T$  of the third lepton could increase the signal more than it does the fakes. I applied a 10 GeV cut on the third lepton  $p_T$ .

The yields are presented in Table 4.17. It can be noted that, although there is an increase in the signal events, there is an even bigger increase in the fakes event. For 2j1b the fakes sum up to almost 65 events, 61% of the signal events. The signal fractions and the signal/background ratios go down, whereas there is a small increase in all the other background samples. Figure 4.18 shows what we just explained. The first bin, which is the one I added by applying a lower cut on the third lepton  $p_T$ , has more fake events than it has signal.

Table 4.18 shows the results for this selection for the IWP analysed. The gain in the signal does not justify the increase in the fake backgrounds. The leptons with  $p_T$  lower than 15 GeV are mostly fake, so this cut does not give any advantage when compared to the previous one. Therefore, I will not analyse a 28-15-10 combination of lepton  $p_T$ .

This result can be explained by looking at Figures 4.10(b) and 4.11(b). it can be noted that *PLV* has a worse rejection at low- $p_T$  than it has at high- $p_T$ . When going from 15 GeV to 10 GeV on the third lepton we see the same result we observed with *Default* when going down from 20 GeV to 15 GeV, that is a higher increase in the fakes with respect to the signal. On the other hand, *PLI* and *PLIV* are able to keep a better rejection of the fake backgrounds with respect to *PLV*, as can be seen from both Figures 4.10(b) and 4.11(b) and Table 4.18. If the threshold was lowered even more, *PLI* and *PLIV* would give the same results which *PLV* and *Default* give at 10 and 15 GeV respectively.

<i>PLV (28-20-10)</i>	<i>2j1b</i>	<i>3j1b</i>
<i>tllq</i>	$106.4 \pm 0.7$	$60.0 \pm 0.6$
<i>t̄t + tW</i>	$26.6 \pm 1.0$	$12.5 \pm 0.7$
<i>Z + jets</i>	$39.4 \pm 4.2$	$14.0 \pm 1.2$
Multiboson[ <i>LF</i> ]	$7.8 \pm 0.3$	$4.1 \pm 0.1$
Multiboson[ <i>HF</i> ] + <i>B</i>	$62.9 \pm 0.7$	$38.3 \pm 0.4$
Multiboson[ <i>HF</i> ] + <i>C</i>	$42.8 \pm 0.7$	$23.4 \pm 0.4$
<i>t̄tZ + tWZ</i>	$87.3 \pm 0.8$	$133.6 \pm 1.0$
<i>t̄tH + t̄tW + 3t</i>	$7.3 \pm 0.2$	$5.6 \pm 0.2$
Total	$380.3 \pm 8.6$	$291.5 \pm 4.6$
<i>S/√B</i>	6.42	3.94
<i>S/√(B + S)</i>	5.45	3.51
% <i>tllq</i>	27.97	20.58
% <i>t̄t + tW</i>	6.99	4.30
% <i>Z+jets</i>	10.36	3.77

Table 4.17: Event yields using *PLV (28-20-10)* selection

SR	<i>28-20-10</i>	<i>PLV</i>	<i>PLI</i>	<i>PLIV</i>
<i>2j1b</i>	<i>S/√B</i>	6.42	6.58	6.00
	<i>S/√(B + S)</i>	5.45	5.47	4.98
	<i>tllq</i>	$106.4 \pm 0.7$	$96.8 \pm 0.7$	$79.9 \pm 0.6$
	<i>t̄t + tW</i>	$26.6 \pm 1.0$	$11.2 \pm 0.7$	$7.5 \pm 0.5$
<i>3j1b</i>	<i>Z+jets</i>	$39.9 \pm 4.2$	$12.5 \pm 2.4$	$9.2 \pm 2.0$
	<i>S/√B</i>	3.94	3.87	3.54
	<i>S/√(B + S)</i>	3.51	3.42	3.13
	<i>tllq</i>	$60.0 \pm 0.6$	$54.8 \pm 0.6$	$45.6 \pm 0.5$
	<i>t̄t + tW</i>	$12.5 \pm 0.7$	$6.5 \pm 0.6$	$4.0 \pm 0.4$
	<i>Z+jets</i>	$14.0 \pm 1.2$	$4.5 \pm 0.7$	$3.5 \pm 0.6$

Table 4.18: Results for all the WPs analysed with a *28-20-10* cut on the leptons  $p_T$

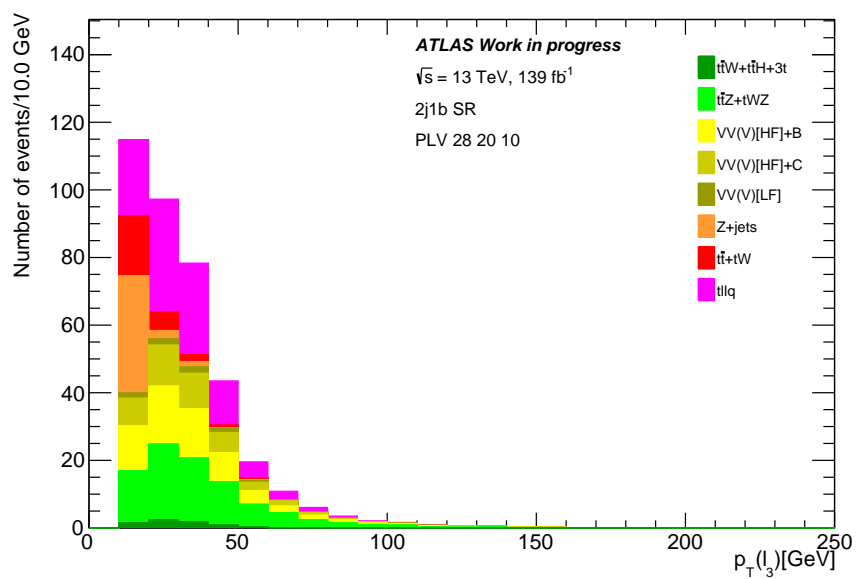


Figure 4.18: Plot for third lepton transverse momentum with *PLV (28-20-10)* SR 2j1b.

**28-15-15**

Seeing how the 10 GeV cut on the third lepton added too much of the fake background, I decided to stick with 15 GeV on the third lepton and we tried to reduce the second lepton  $p_T$  down to 15 GeV.

The yields using  $PLV$  are presented in Table 4.19. Surprisingly, the yields are almost identical to the ones of 28-20-15 selection. This means that the cut on the second lepton  $p_T$  added only few events for both signal and background. Because the background is made of less events, its percentage increase is higher than the signal's one. Therefore, it is better to keep a 20 GeV limit on the second lepton  $p_T$ .

$PLV$ (28-15-15)	2j1b	3j1b
$tllq$	$98.1 \pm 0.7$	$55.4 \pm 0.6$
$t\bar{t} + tW$	$14.4 \pm 0.8$	$7.0 \pm 0.5$
$Z + jets$	$11.2 \pm 1.8$	$3.6 \pm 0.6$
Multiboson[LF]	$7.0 \pm 0.2$	$3.8 \pm 0.1$
Multiboson[HF] + B	$57.4 \pm 0.6$	$35.1 \pm 0.4$
Multiboson[HF] + C	$39.6 \pm 0.6$	$21.6 \pm 0.4$
$t\bar{t}Z + tWZ$	$81.4 \pm 0.8$	$124.4 \pm 1.0$
$t\bar{t}H + t\bar{t}W + 3t$	$6.7 \pm 0.2$	$5.1 \pm 0.1$
Total	$315.8 \pm 5.7$	$255.9 \pm 3.8$
$S/\sqrt{B}$	6.65	3.91
$S/\sqrt{B + S}$	5.52	3.46
% $tllq$	31.06	21.65
% $t\bar{t} + tW$	4.56	2.74
% $Z + jets$	3.55	1.41

Table 4.19: Event yields using  $PLV$  (28-15-15) selection

The other two Working Points showed the same results, as can be seen in Table 4.20.

SR	28-15-15	$PLV$	$PLI$	$PLIV$
2j1b	$S/\sqrt{B}$	6.65	6.56	5.97
	$S/\sqrt{B + S}$	5.52	5.41	4.92
	$tllq$	$98.1 \pm 0.7$	$91.5 \pm 0.7$	$75.3 \pm 0.6$
	$t\bar{t} + tW$	$14.4 \pm 0.8$	$6.9 \pm 0.5$	$4.1 \pm 0.4$
	$Z + jets$	$11.2 \pm 1.8$	$5.7 \pm 1.1$	$3.8 \pm 1.0$
3j1b	$S/\sqrt{B}$	3.91	3.80	3.46
	$S/\sqrt{B + S}$	3.46	3.36	3.06
	$tllq$	$55.4 \pm 0.6$	$51.9 \pm 0.6$	$43.0 \pm 0.5$
	$t\bar{t} + tW$	$7.0 \pm 0.5$	$4.7 \pm 0.5$	$2.5 \pm 0.3$
	$Z + jets$	$3.6 \pm 0.6$	$1.7 \pm 0.4$	$0.9 \pm 0.3$

Table 4.20: Results for all the selections

## Conclusions

Summaries for each selection are presented in Tables 4.21 to 4.23, whereas Figures 4.19 and 4.20 show the summary with the fractions for all samples. The better cut is 28-20-15 GeV. The fakes increase by almost 50% with respect to 28-20-20 GeV, but the amount of signal increasing is more. A 10 GeV cut on the third lepton allows for too much background, with the signal increasing by only a few points. A 15 GeV cut on the second lepton reduced in two total events added to 28-20-15, with half of those being fakes.

The analysis with different cuts on the leptons  $p_T$  made me realise, as predicted earlier using the common selection, that the PLImprovedVeryTight WP is worse than PLVTight and PLImprovedTight. Its signal/background ratios are the lowest, as well as the signal yields, for all the different combinations of lepton  $p_T$ . On the other hand, there is a significant decrease in the fakes. However, the loss on the signal is not compensated with the decrease in the fakes.

*PLV* and *PLI* show once again similar results. *PLV* has more events, thus it has more fakes too, with higher signal/background ratios. On the other hand, *PLI* reduces the fakes more than it does to the signal, especially for  $Z$ -jets 3j1b. At low- $p_T$ , *PLI* is better because it is able to keep the fake background under control better than *PLV*.

SR	<i>PLV</i>	28-20-20	28-20-15	28-20-10	28-15-15
2j1b	$S/\sqrt{B}$	6.37	6.63	6.42	6.65
	$S/\sqrt{B+S}$	5.23	5.51	5.45	5.52
	$tllq$	$83.8 \pm 0.6$	$97.5 \pm 0.7$	$106.4 \pm 0.7$	$98.1 \pm 0.7$
	$t\bar{t} + tW$	$8.8 \pm 0.6$	$14.1 \pm 0.7$	$26.6 \pm 1.0$	$14.4 \pm 0.8$
	$Z$ -jets	$4.7 \pm 0.7$	$10.7 \pm 1.8$	$39.4 \pm 4.2$	$11.2 \pm 1.8$
3j1b	$S/\sqrt{B}$	3.61	3.90	3.94	3.91
	$S/\sqrt{B+S}$	3.20	3.45	3.51	3.46
	$tllq$	$47.7 \pm 0.5$	$55.1 \pm 0.6$	$60.0 \pm 0.6$	$55.4 \pm 0.6$
	$t\bar{t} + tW$	$4.3 \pm 0.4$	$6.7 \pm 0.5$	$12.5 \pm 0.7$	$7.0 \pm 0.5$
	$Z$ -jets	$2.0 \pm 0.3$	$3.5 \pm 0.6$	$14.0 \pm 1.2$	$3.6 \pm 0.6$

Table 4.21: Results for *PLV* with all the cuts applied on second and third lepton  $p_T$

SR	<i>PLI</i>	28-20-20	28-20-15	28-20-10	28-15-15
2j1b	$S/\sqrt{B}$	6.16	6.55	6.58	6.56
	$S/\sqrt{B+S}$	5.08	5.39	5.47	5.41
	$tllq$	$80.7 \pm 0.6$	$91.2 \pm 0.7$	$96.8 \pm 0.7$	$91.5 \pm 0.7$
	$t\bar{t} + tW$	$5.1 \pm 0.5$	$6.8 \pm 0.5$	$11.2 \pm 0.7$	$6.9 \pm 0.5$
	Z+jets	$2.8 \pm 0.6$	$5.9 \pm 1.0$	$12.5 \pm 2.4$	$5.7 \pm 1.1$
3j1b	$S/\sqrt{B}$	3.55	3.79	3.87	3.80
	$S/\sqrt{B+S}$	3.15	3.55	3.42	3.36
	$tllq$	$47.7 \pm 0.5$	$51.7 \pm 0.5$	$54.8 \pm 0.6$	$51.9 \pm 0.6$
	$t\bar{t} + tW$	$3.5 \pm 0.4$	$4.6 \pm 0.5$	$6.5 \pm 0.6$	$4.7 \pm 0.5$
	Z+jets	$0.9 \pm 0.2$	$1.5 \pm 0.4$	$4.5 \pm 0.7$	$1.7 \pm 0.4$

Table 4.22: Results for *PLI* with all the cuts applied on second and third lepton  $p_T$ 

SR	<i>PLIV</i>	28-20-20	28-20-15	28-20-10	28-15-15
2j1b	$S/\sqrt{B}$	5.60	5.95	6.00	5.97
	$S/\sqrt{B+S}$	4.62	4.90	4.98	4.92
	$tllq$	$66.5 \pm 0.6$	$75.0 \pm 0.6$	$79.9 \pm 0.6$	$75.3 \pm 0.6$
	$t\bar{t} + tW$	$2.9 \pm 0.3$	$4.0 \pm 0.4$	$7.5 \pm 0.5$	$4.1 \pm 0.4$
	Z+jets	$1.8 \pm 0.6$	$4.0 \pm 0.9$	$9.2 \pm 2.0$	$3.8 \pm 1.0$
3j1b	$S/\sqrt{B}$	3.24	3.46	3.54	3.46
	$S/\sqrt{B+S}$	2.88	3.06	3.13	3.06
	$tllq$	$38.3 \pm 0.5$	$42.9 \pm 0.5$	$45.6 \pm 0.5$	$43.0 \pm 0.5$
	$t\bar{t} + tW$	$1.8 \pm 0.3$	$2.5 \pm 0.3$	$4.0 \pm 0.4$	$2.5 \pm 0.3$
	Z+jets	$0.4 \pm 0.1$	$0.8 \pm 0.3$	$3.5 \pm 0.6$	$0.9 \pm 0.3$

Table 4.23: Results for *PLIV* with all the cuts applied on second and third lepton  $p_T$ 

Figure 4.19: Summary of the fractions of various samples for the different selections tested for SR 2j1b.

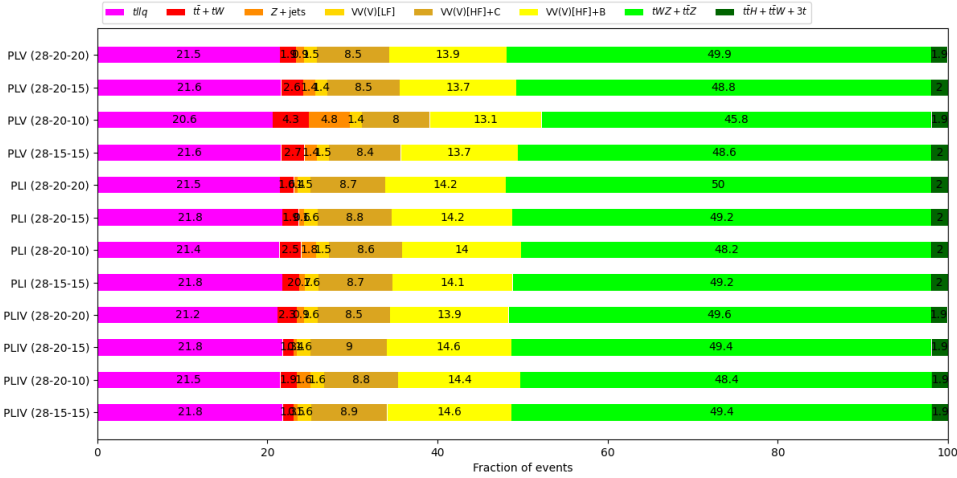


Figure 4.20: Summary of the fractions of various samples for the different selections tested for SR 3j1b.

#### 4.6.3 $b$ -tagging analysis

Once the fake backgrounds were reduced by means of IWPs and the signal acceptance was maximised using different thresholds for the leptons  $p_T$ , I tried to work on the Multiboson background. This background is made of Multiboson, especially Diboson  $WZ$ , plus jets. It is not made of fake leptons, therefore it cannot be reduced using isolation. Because the background has jets in the final state, it can be reduced by changing the  $b$ -tagging WP.

When starting this analysis, I split the Multiboson sample in three different samples, based on the flavour of the jet. The purpose of that was to see how the three different flavours were affected by a different  $b$ -tagging Working Point. In the common selection I used a 70% efficiency (Table 4.1), now I want to test the 77% efficiency. A higher efficiency means less rejection of  $c$  and light jets, so we expect all the yields (especially the Multiboson) to rise up. On the other hand, this will increase the signal yields too, because the more  $b$ -jets we recognise, the more signal we have.

I tested the `eff_77` WP for *PLV* and *PLI* only using a 28-20-20 GeV and 28-20-15 GeV cut on leptons  $p_T$ . The `eff_60` WP was not tested because in the previous analysis it was noted that it reduced too much of the signal.

Once again, I will be showing the yields only for one selection, *PLV* (28-20-15), and for the others I will report the ratios and the summary table for comparison.

Table 4.24 shows the event yields for this WP. We get the results we expected, that is an increase in all samples. The samples most affected are, as predicted, the Multibosons. We have an increase in the number of Multiboson[HF] +  $B$  because the efficiency of identifying a  $b$ -jet is higher, but we also have an even bigger increase for the light-jet and the  $c$ -jet, because their rejection decreases. The  $c$ -jet in particular

<i>PLV (28-20-15), b-tag=77</i>	<i>2j1b</i>	<i>3j1b</i>
<i>tllq</i>	$105.0 \pm 0.7$	$56.8 \pm 0.6$
$t\bar{t} + tW$	$15.3 \pm 0.8$	$6.8 \pm 0.5$
$Z + jets$	$12.0 \pm 1.9$	$4.2 \pm 0.6$
Multiboson[ <i>LF</i> ]	$22.1 \pm 0.5$	$11.8 \pm 0.3$
Multiboson[ <i>HF</i> ] + <i>B</i>	$61.3 \pm 0.6$	$37.1 \pm 0.4$
Multiboson[ <i>HF</i> ] + <i>C</i>	$80.3 \pm 0.9$	$42.2 \pm 0.5$
$t\bar{t}Z + tWZ$	$84.9 \pm 0.8$	$122.4 \pm 1.0$
$t\bar{t}H + t\bar{t}W + 3t$	$6.6 \pm 0.2$	$4.8 \pm 0.1$
Total	$387.5 \pm 6.4$	$286.0 \pm 4.0$
$S/\sqrt{B}$	5.58	3.77
$S/\sqrt{B+S}$	4.90	3.36
% <i>tllq</i>	22.88	19.86
% $VV(V)[LF]$	4.81	4.13
% $VV(V)[HF] + B$	13.36	12.97
% $VV(V)[HF] + C$	17.49	14.69

Table 4.24: Event yields using *PLV (28-20-15)* selection with *b*-tagging efficiency at 77%

becomes the sample with the highest number of events out of the three. The fake backgrounds don't increase because the isolation does not depend on the type of jet. The signal increases because our signal requires exactly one *b*-jet, and this WP allows for more *b*-jets than the previous one used for *b*-tagging. Nevertheless, the background increases more than the signal does. As a consequence, the signal/background ratios decrease, as well as the fraction of signal.

The comparison between the two *b*-tagging WPs can be seen in Table 4.25 for *PLV* and in Table 4.26 for *PLI*. Figures 4.21 and 4.22 show the fractions for different cuts for both SRs. For *PLI* as well the signal/background ratios are lower when using the 77% *b*-tagging efficiency. The percentage of signal for both *PLI* and *PLV* (using either 20 GeV or 15 GeV on the third lepton) is the lowest tested so far (around 20%), and the gain in the signal, compared to 70% efficiency, is less than the increase on the background. Therefore, the `eff_77` WP is worse at maximising the signal than the `eff_70` WP.

Since the `eff_77` WP increased the backgrounds more than the signal, I did not test the `eff_85` WP, because even though it would increase the signal events, it would also double the *charm-jet* background and it would increase by 450% the *light-jet* background with respect to the `eff_77` WP.

SR	PLV	28-20-20		28-20-15	
		b-tag=70	b-tag=77	b-tag=70	b-tag=77
2j1b	$S/\sqrt{B}$	6.37	5.82	6.63	5.58
	$S/\sqrt{B+S}$	5.23	4.96	5.51	4.90
	$tllq$	$83.8 \pm 0.6$	$90.2 \pm 0.7$	$97.5 \pm 0.7$	$105.0 \pm 0.7$
	$VV(V)[LF]$	$6.2 \pm 0.2$	$19.6 \pm 0.4$	$7.0 \pm 0.2$	$22.1 \pm 0.5$
	$VV(V)[HF] + B$	$49.6 \pm 0.6$	$53.2 \pm 0.6$	$57.2 \pm 0.6$	$61.3 \pm 0.6$
3j1b	$S/\sqrt{B}$	3.61	3.27	3.79	3.77
	$S/\sqrt{B+S}$	3.20	2.93	3.55	3.36
	$tllq$	$47.7 \pm 0.5$	$49.0 \pm 0.5$	$55.1 \pm 0.6$	$56.8 \pm 0.6$
	$VV(V)[LF]$	$3.3 \pm 0.1$	$10.2 \pm 0.2$	$3.7 \pm 0.1$	$11.8 \pm 0.3$
	$VV(V)[HF] + B$	$30.8 \pm 0.4$	$31.4 \pm 0.4$	$34.9 \pm 0.4$	$37.1 \pm 0.4$
	$VV(V)[HF] + C$	$18.9 \pm 0.4$	$36.8 \pm 0.5$	$21.6 \pm 0.4$	$42.2 \pm 0.5$

Table 4.25: Results for  $PLV$  using all lepton  $p_T$  combinations for the two  $b$ -tagging WPs analysed

SR	PLI	28-20-20		28-20-15	
		b-tag=70	b-tag=77	b-tag=70	b-tag=77
2j1b	$S/\sqrt{B}$	6.16	5.74	6.55	6.12
	$S/\sqrt{B+S}$	5.08	4.89	5.39	5.20
	$tllq$	$80.7 \pm 0.6$	$86.7 \pm 0.7$	$91.2 \pm 0.7$	$98.1 \pm 0.7$
	$VV(V)[LF]$	$6.1 \pm 0.2$	$19.3 \pm 0.4$	$6.7 \pm 0.2$	$21.3 \pm 0.5$
	$VV(V)[HF] + B$	$48.7 \pm 0.6$	$52.2 \pm 0.6$	$54.5 \pm 0.7$	$58.5 \pm 0.6$
3j1b	$S/\sqrt{B}$	3.61	3.39	3.79	3.64
	$S/\sqrt{B+S}$	3.20	3.04	3.35	3.25
	$tllq$	$46.1 \pm 0.5$	$47.2 \pm 0.5$	$51.7 \pm 0.6$	$53.2 \pm 0.6$
	$VV(V)[LF]$	$3.5 \pm 0.4$	$10.4 \pm 0.2$	$3.7 \pm 0.1$	$11.6 \pm 0.3$
	$VV(V)[HF] + B$	$30.4 \pm 0.4$	$32.2 \pm 0.4$	$33.7 \pm 0.4$	$35.7 \pm 0.3$
	$VV(V)[HF] + C$	$18.7 \pm 0.4$	$36.7 \pm 0.5$	$20.8 \pm 0.4$	$40.4 \pm 0.5$

Table 4.26: Results for  $PLI$  using all lepton  $p_T$  combinations for the two  $b$ -tagging WPs analysed

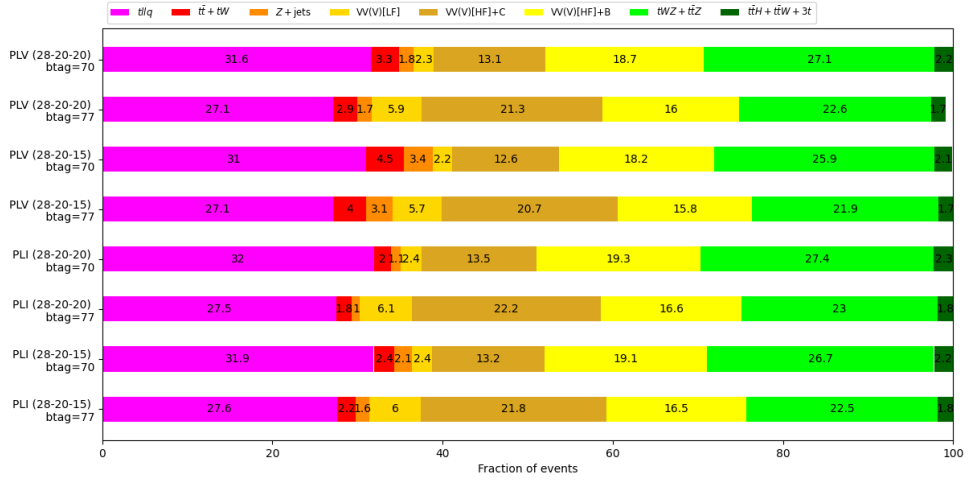


Figure 4.21: Summary of the percentages of the various samples for the  $b$ -tagging analysis with SR  $2j1b$ .

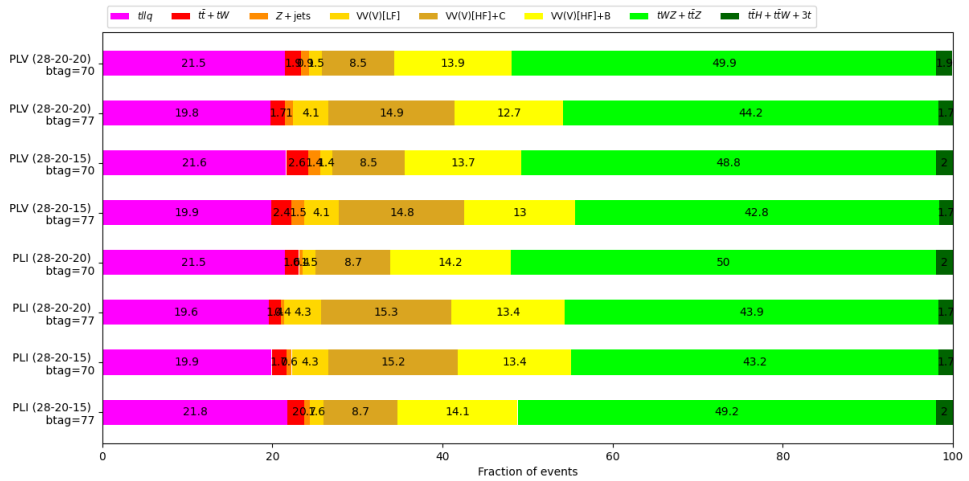


Figure 4.22: Summary of the percentages of the various samples for the  $b$ -tagging analysis with SR  $3j1b$ .

#### 4.6.4 High jet multiplicity signal region

Finally, I have tested a more inclusive jet selection. The SRs in the previous analysis required exactly two or three jets, with exactly one  $b$ -tagged jet. The aim is to try to increase the signal acceptance by allowing events with more than three jets with only one  $b$ -tagged, defining a  $nj1b$  SR.

I have tested this SR only with  $PLV$  and  $PLI$  using both a 28-20-20 GeV and a 28-20-15 GeV cut on the leptons  $p_T$ , because these turned out to be the best selections. I have used the common selection (Table 4.3) with a 70%  $b$ -tagging efficiency.

This SR is the inclusive one, in that it has yields of both  $2j1b$  and  $3j1b$  as well as other five combinations ( $4j1b$ ,  $5j1b$ ,  $6j1b$ ,  $7j1b$  and  $8j1b$ ). The requirement is to have always only one  $b$ -jet, while the number of total jets can be between 2 (which is SR  $2j1b$ ) and 8. We predict more events than the previous two SR combined. The majority of events will be from SR  $2j1b$  and SR  $3j1b$ , because only few samples allow more than three jets, especially for the signal.

In Table 4.27 the yields for  $PLV$  (28-20-15) are presented. I get the results I expected, with the increase in the signal (20 events more than the two SRs combined) accompanied by a smaller increase in the fakes (4 for  $t\bar{t}$  and 2 for  $Z+jets$ ) and an increase in the Multiboson by 40 events. The  $t\bar{t}Z + tWZ$  sample is the one with the highest increase, 100 events.

The signal/background ratios are higher than they are in  $2j1b$  and  $3j1b$ , but the fraction of signal is less. Nevertheless, because the fakes' percentage is even lesser, this SR could be useful when performing isolation studies. We have many events for the signal (even though they contribute to only one fifth of the total events), which could be useful in a multivariate analysis, and some 40 events for the fakes, which accounts for less than 5% of the total but are enough to train a NN for discriminating the signal and the background.

In Tables 4.28 and 4.29 I have presented the comparison between the yields for  $2j1b + 3j1b$  (exclusive SR) and for  $nj1b$  (inclusive SR). It is interesting to see that the signal/background ratios for the exclusive SR are the highest. We can observe that the signal for the inclusive has approximately 20 events more than the exclusive. The fakes increase from exclusive to inclusive by few events, whereas the Multiboson increase almost as much as the signal. Instead, the other backgrounds (especially  $t\bar{t}Z$ , but also  $tWZ$ ,  $t\bar{t}W$ ,  $t\bar{H}$  and  $3t$ ) have the highest increase (almost 80%). This increase can be easily noted in Figure 4.23. Therefore, the exclusive region better optimise the signal than the inclusive region, because the latter increases the background by more than it does to the signal.

The use of SR  $nj1b$  is not recommended, whereas an analysis using the exclusive region could bring some interesting results.

	<i>PLV</i> (28-20-15)	<i>nj1b</i>
<i>tllq</i>		$173.7 \pm 1.0$
$t\bar{t} + tW$		$24.8 \pm 1.0$
$Z + jets$		$16.2 \pm 1.9$
Multiboson[ <i>LF</i> ]		$44.1 \pm 0.5$
Multiboson[ <i>HF</i> ] + <i>B</i>		$94.2 \pm 0.7$
Multiboson[ <i>HF</i> ] + <i>C</i>		$67.9 \pm 0.7$
$t\bar{t}Z + tWZ$		$379.6 \pm 1.7$
$t\bar{t}W + t\bar{t}H + 3t$		$16.7 \pm 0.3$
Total		$817.1 \pm 7.9$
$S/\sqrt{B}$		6.55
$S/\sqrt{B+S}$		5.88
% <i>tllq</i>		19.82
% $t\bar{t} + tW$		2.83
% $Z+jets$		1.84

Table 4.27: Event yields for SR *nj1b* using *PLV* selection

<i>PLV</i>	28-20-20		28-20-15	
	<i>2j1b + 3j1b</i>	<i>nj1b</i>	<i>2j1b + 3j1b</i>	<i>nj1b</i>
$S/\sqrt{B}$	6.97	6.43	7.48	6.55
$S/\sqrt{B+S}$	5.95	5.63	6.47	5.88
<i>tllq</i>	$131.5 \pm 1.1$	$149.9 \pm 0.9$	$152.5 \pm 1.3$	$173.7 \pm 1.0$
$t\bar{t} + tW$	$13.1 \pm 1.0$	$16.0 \pm 0.8$	$20.8 \pm 1.2$	$24.8 \pm 1.0$
$Z+jets$	$6.7 \pm 1.0$	$7.9 \pm 0.8$	$14.2 \pm 2.4$	$16.2 \pm 1.9$
Multiboson	$143.6 \pm 2.3$	$161.6 \pm 1.8$	$163.8 \pm 2.3$	$206.2 \pm 2.2$
Remaining BKGs	$192.8 \pm 1.9$	$343.8 \pm 1.8$	$217 \pm 2.1$	$396.3 \pm 2.0$

Table 4.28: Comparison between the inclusive (*nj1b*) and the exclusive (*2j1b* and *3j1b*) yields for *PLV*

<i>PLI</i>	28-20-20		28-20-15	
	<i>2j1b + 3j1b</i>	<i>nj1b</i>	<i>2j1b + 3j1b</i>	<i>nj1b</i>
$S/\sqrt{B}$	6.88	6.28	7.32	6.87
$S/\sqrt{B+S}$	5.87	5.56	6.25	5.93
<i>tllq</i>	$126.8 \pm 1.1$	$144.6 \pm 0.9$	$142.9 \pm 1.2$	$162.9 \pm 1.0$
$t\bar{t} + tW$	$8.6 \pm 0.9$	$9.4 \pm 0.6$	$11.4 \pm 1.0$	$13.2 \pm 0.8$
$Z+jets$	$3.7 \pm 0.8$	$4.2 \pm 0.7$	$7.41 \pm 1.3$	$8.2 \pm 1.1$
Multiboson	$141.5 \pm 2.1$	$178.6 \pm 1.8$	$157.1 \pm 2.2$	$197.7 \pm 1.8$
Remaining BKGs	$186.1 \pm 1.9$	$340.9 \pm 1.8$	$204.2 \pm 1.9$	$372.9 \pm 1.8$

Table 4.29: Comparison between the inclusive (*nj1b*) and the exclusive (*2j1b* and *3j1b*) yields for *PLI*

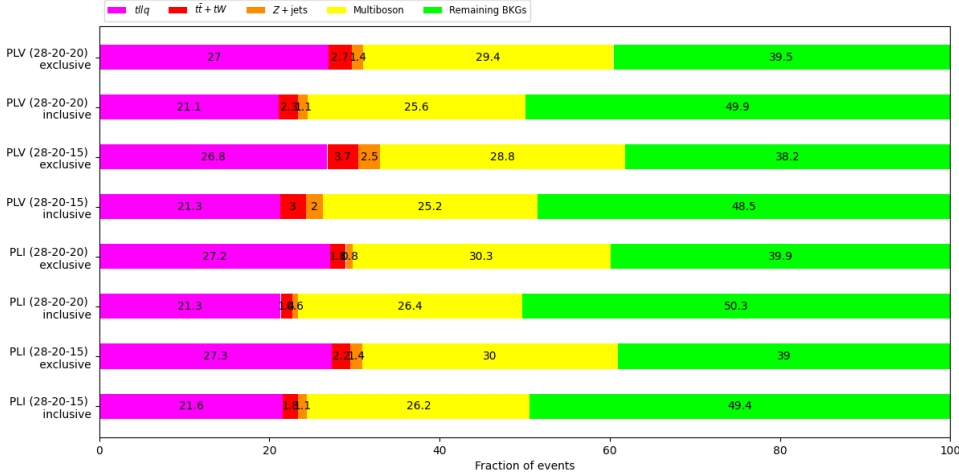


Figure 4.23: Summary of the percentages of the various samples for the inclusive SR ( $nj1b$ ) and the exclusive SR ( $2j1b+3j1b$ ).

## 4.7 Conclusions

For this thesis I have analysed a total of six different Isolation WP combinations, four different cuts on the leptons  $p_T$ , three different signal regions and two  $b$ -tagging efficiencies.

The Isolation WPs which give the highest signal acceptance while reducing the fake backgrounds for SRs  $2j1b$  and  $3j1b$  are **PLVTight** and **PLIMprovedTight**. The former has more events, which is useful for a multivariate analysis, whereas the latter has less of the fake background, at the cost of smaller signal/background ratio and fraction of signal events. The first three WP combinations (*Default*, *Pflow* and *TightTrack*) do not provide a good fake background rejection, while **PLIV**'s efficiency on the signal is too low.

The best lepton  $p_T$  cut combination is **28-20-15** GeV for all the SRs. A 10 GeV cut on the third lepton adds more fakes than signal, so it is recommended to stick to 15 GeV. The 15 GeV cut on the third lepton gives better signal/background ratios than **28-20-20** GeV, without adding too much of fake backgrounds. Instead, a 15 GeV cut on the second lepton gives no advantage in terms of optimising the signal acceptance, because it adds less than one event for both signal and fakes, so the fraction increase is more for the background.

The 70%  $b$ -tagging efficiency is recommended instead of the 77%. The latter adds more background than signal, resulting in having the lowest fractions of signal out of all the selections. With a 77% efficiency, the  $c$ -jet Multiboson events double up with respect to the 70%, as opposed to the signal increasing by 10%.

The inclusive  $nj1b$  SR is obviously the one with most events. I tested this inclusive SR with **PLV** and **PLI** and I noticed good signal/background ratios and very low

<i>PLV (28-20-15), b-tag = 70%</i>	<i>2j1b</i>
<i>tllq</i>	$97.5 \pm 0.7$
<i>t̄t + tW</i>	$14.1 \pm 0.7$
<i>Z+jets</i>	$10.7 \pm 1.8$
Multiboson[ <i>LF</i> ]	$7.0 \pm 0.2$
Multiboson[ <i>HF</i> ] + <i>B</i>	$57.2 \pm 0.6$
Multiboson[ <i>HF</i> ] + <i>C</i>	$39.4 \pm 0.6$
<i>t̄tZ + tWZ</i>	$81.1 \pm 0.8$
<i>t̄tH + t̄tW + 3t</i>	$6.6 \pm 0.2$
Total	$313.6 \pm 5.7$
Data	369

Table 4.30: Event yields using *PLV(28-20-15)* selection for SR *2j1b*.

fraction of the fakes when compared to *2j1b* or *3j1b* singularly. However, a comparison between the inclusive SR and the exclusive SR (that is, the yields of *2j1b* and *3j1b* together) showed how the usage of the exclusive SR is recommended. This is due to the fact that the excluded regions (*4j1b*, *5j1b*, *6j1b*, *7j1b* and *8j1b*) has much more background than signal, especially for *t̄tZ* and *tWZ*. The signal/background ratios for the exclusive SR are the highest out of all the selections, for both *PLV* and *PLI* and for both a 20 and 15 GeV cut on the third lepton.

To sum up, for a *2j1b* or *3j1b* analysis, it is recommended to use the *PLVTight* or the *PLIImprovedTight* WP for both electrons and muons, with the requirements on the lepton *pTs* as  $p_T(\ell_1) > 28$  GeV,  $p_T(\ell_2) > 20$  GeV and  $p_T(\ell_3) > 15$  GeV, using the 70% *b*-tagging efficiency operating point. For a more inclusive analysis, it is recommended to require not more than 3 jets, of which only one *b*-tagged.

## 4.8 Data

Finally I decided to check the Data/MC agreement. I did that for all the selections but I am going to show the results only for *PLV (28-20-15 GeV)* with *b*-tagging at 70% efficiency for SR *2j1b*. The results are in Table 4.30.

Before analysing the results, it must be said that the uncertainties are only statistical. Therefore, the uncertainty on the total number of MC simulated events is underestimated, because I am not considering systematic uncertainties. That said, the Data/MC agreement is poor, with the MC events being 15% less than the Data events. This discrepancy was observed also in the previous analysis [29]. In that analysis, Control Regions (CR) were used in order to estimate the normalisation factors for the backgrounds, in particular Diboson, *t̄t* and *t̄tZ*. The CR defined were *nj0b* for Diboson ( $n = 2, 3$ ), *nj1b* ( $n = 2, 3$ ) with no OSSF lepton pair for *t̄t* and *nj2b* ( $n = 3, 4$ ) for *t̄tZ*. By analysing this CR it was observed that the normalisation of all the backgrounds was

Pre-Fit	SR 2j1b	Post-Fit	SR 2j1b
$tllq$	$81.1 \pm 3.3$	$tllq$	$78.9 \pm 11.3$
$t\bar{t} + tW$	$24.8 \pm 1.8$	$t\bar{t} + tW$	$23.8 \pm 5.0$
$Z + jets$	$10.2 \pm 1.5$	$Z + jets$	$28.0 \pm 13.1$
Multiboson[LF]	$22.7 \pm 1.7$	Multiboson[LF]	$19.7 \pm 7.9$
Multiboson[HF]	$101.3 \pm 43.1$	Multiboson[HF]	$101.3 \pm 21.6$
$t\bar{t}Z + tWZ$	$80.6 \pm 18.0$	$t\bar{t}Z + tWZ$	$95.5 \pm 11.4$
$t\bar{t}W + t\bar{t}H$	$6.3 \pm 1.0$	$t\bar{t}W + t\bar{t}H$	$6.5 \pm 1.0$
Total	$327 \pm 50.3$	Total	$353.8 \pm 15.6$
Data	359	Data	359

Table 4.31: Pre-fit (left) and post-fit (right) event yields in SR 2j1b from previous analysis [29], with Gradient WP for both electrons and muons.

different from the normalisation produced by the MC simulated events. In Table 4.31 the yields from the previous analysis [29] are presented, where the Gradient IWP was used for both electrons and muons and the event were selected with the selections in Table 4.3. After adjusting the normalisations using the information from the CRs, the data/MC agreement in the SRs is improved, with a discrepancy of less than 2%.

Since there was no time in this analysis for a fit using CRs, I decided to extract the normalisation factors from the previous analysis and I tested that on our analysis. Because we are using different cuts and Isolation WPs we do not expect to find an agreement within 2%, which is what we got in the past analysis, but this could give an idea of the real amount of total events we expect to have. Nevertheless, the scaling factors can be useful for a quick check between data and MC when there is no time for a CR study.

Sample	Scaling Factor
$tllq$	0.973
$t\bar{t} + tW$	0.96
$Z+jets$	2.74
Multiboson [LF]	0.87
Multiboson [HF]	1
$t\bar{t}Z + tWZ$	1.18
$t\bar{t}H + t\bar{t}W + 3t$	1.03

Table 4.32: Scaling factors for signal and backgrounds extracted from Table 4.31 for SR 2j1b.

The scaling factors for signal and backgrounds are presented in Table 4.32. The  $t\bar{t}Z + tWZ$  background has almost a 20% increase, which could be relevant because we have many events from that background.  $Z+jets$  also increases by a lot, but our selection (Table 4.30) has very few  $Z+jets$  events, so that should not make a lot of

difference.

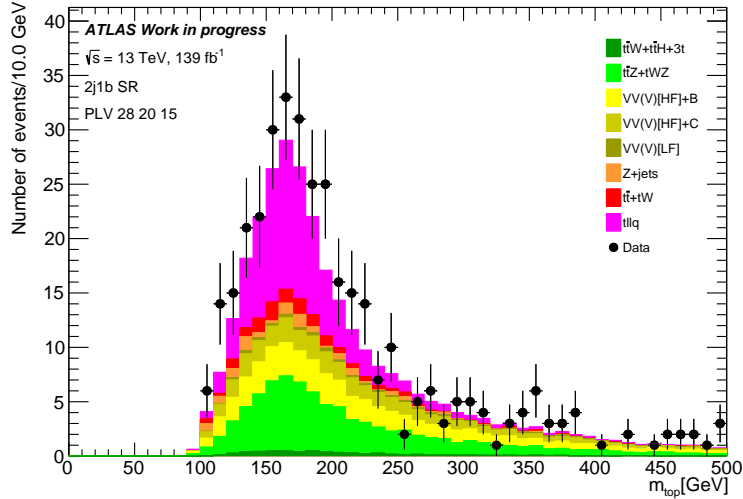
I applied those scaling factors to the yields in Table 4.30, and obtained the yields in Table 4.33. The uncertainties are only statistical, so they are underestimated. Our yields are  $2.9\sigma$  distant from data.

Figure 4.24 show the difference between the yields before applying the scaling factors (Figure 4.24(a)) and the yields after applying the scaling factors (Figure 4.24(b)). The latter shows a better data/MC agreement, as expected from Table 4.33. The  $Z+jets$  background increases as well as the  $t\bar{t}Z$  background.

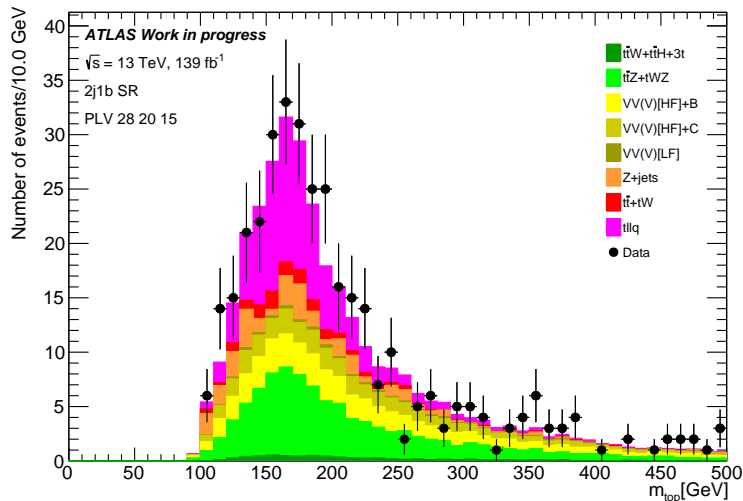
<i>PLV (28-20-15); btag = 70</i>	<i>SR 2j1b</i>
$tllq$	$94.9 \pm 0.7$
$t\bar{t} + tW$	$13.5 \pm 0.7$
$Z+jets$	$29.3 \pm 4.9$
Multiboson [LF]	$6.1 \pm 0.2$
Multiboson[HF] + $B$	$57.2 \pm 0.6$
Multiboson[LF] + $C$	$39.4 \pm 0.6$
$t\bar{t}Z + tWZ$	$95.7 \pm 0.9$
$t\bar{t}H + t\bar{t}W + 3t$	$6.8 \pm 0.2$
Total	$343.0 \pm 8.8$
Data	369

Table 4.33: Event yields using  $PLV(28-20-15)$  selection for SR  $2j1b$ , after the rescaling.

The results we get from both Table 4.33 and Figure 4.24(b) show that, as expected, data and MC are not compatible, because the total number of events is  $2.9\sigma$  apart from data. Nevertheless, the discrepancy between the data and the MC simulated events is 7.05%, which is better than what we had in Table 4.30. Therefore, we can say that the scaling factors work, even though they had been obtained in a different analysis with different selections, and those scaling factors could be used in the future for fast-checking of results.



(a) Without scaling factors



(b) With scaling factors

Figure 4.24: Comparison between un-scaled yields (top) and scaled yields (bottom) for the plot of reconstructed *top* mass.



# Chapter 5

## Summary and conclusions

The  $tZq$  is a weak process, observed by the ATLAS experiment at the LHC [29]. This process is extremely rare, because it involves the single *top* quark production in the t-channel associated with a  $Z$  boson and a second quark, which at the ATLAS experiment is either a down or an up quark. The measured cross section for this process is  $\sigma = 97 \pm 13(\text{stat.}) \pm 7(\text{syst.}) \text{ fb}$  [29].

The most interesting final state is the trilepton final state, which occurs when both the  $Z$  and  $W$  bosons decay leptonically. The trilepton channel is the one with the lowest branching ratio, but it is the purest channel because it can be best separated from the backgrounds. The final state has one opposite sign same flavour lepton pair from the  $Z$  boson decay, a lepton coming from the  $W$  boson decay, and two jets, of which one from the  $b$ -quark from the top quark decay and the other one is preferentially in the forward direction. Hadronically decaying  $\tau$  leptons are not considered, so the leptons are only electrons and muons. Two orthogonal SRs were defined, based on the number of jets in the final state. The event selection is described in Table 4.3.

The former analysis achieved a 15% uncertainty, dominated by statistics, on the cross section measurement. To improve the precision of the measurement, it is important to increase the signal acceptance while keeping the backgrounds under control. The purpose of my thesis is to refine the event selection by using the most recent object reconstruction algorithms available.

I have studied different Isolation Working Points in order to find the one that better optimised the signal acceptance. The Isolation analysis is important because our background is made, among the others, of  $Z+\text{jets}$  and  $t\bar{t}$  events. These processes pass the  $tZq$  event selection when a fake lepton is identified as a prompt one. Fake leptons are the leptons generated within a jet. The Isolation Working Points have different efficiencies for identifying prompt and non-prompt leptons. I have tested different Working Points for SR  $2j1b$  and  $3j1b$ , trying to find the one which gave a good signal acceptance and a strong fake background rejection. I have found that the **PLVTight** and **PLImprovedTight** WPs are the best ones, because they have the highest signal/background ratios and highest signal fraction.

In order to further increase the signal acceptance, I have also tested different cuts on the leptons transverse momentum. The result is that the *28-20-15* GeV cut is the most efficient, because it adds more signal than *28-20-20* GeV without adding too much background, which is what happens when we apply a 10 GeV cut on the third lepton.

Then I have tested different values of *b*-tagging efficiency. For this analysis I have split the Multiboson in three samples based on the flavour of the associated jets. This allowed me to check how many events we added for each flavour category changing the *b*-tagging efficiency. The increase in the *c*-jets component with a 77% *b*-tagging efficiency did not match the increase in the signal when compared to the 70%. Therefore, the 70% *b*-tagging efficiency is suggested. To sum up, the best working points for SR *2j1b* and *3j1b* are **PLVTight** and **PLImprovedTight** with a *28-20-20* GeV and *28-20-15* GeV cut on  $p_T(\ell)$ , *b*-tagging efficiency = 70%.

Finally I have tested this setup for an inclusive jet selection in order to see if an *nj1b* SR could be used instead of the other two for a better optimisation of the event selection. It turned out that the amount of  $t\bar{t}Z$  and  $tWZ$  backgrounds increased too much for  $n \geq 4$ , whereas the increase in the signal was not of the same amount. Therefore, the exclusive region is suggested over the inclusive region, and the exclusive region has better signal/background ratios than both signal regions taken separately.

In conclusion, for future analysis on the  $tZq$  process, to increase the signal acceptance and to reduce the statistical uncertainty on the cross-section measurement, my suggestion is to use the **PLVTight** Isolation Working Point for both electrons and muons with a *28-20-15* GeV cut on lepton  $p_T$  for SR *2j1b* and *3j1b* using a 70% *b*-tagging efficiency.

## Appendix A

# Description of Monte Carlo datasets

### Signal sample

The production of  $tZq$  events was modelled using the MADGRAPH5\_AMC@NLO v 2.3.3 [57] generator at NLO with the NNPDF3.0NLO [58] parton distribution function (PDF). The events were interfaced with PYTHIA8.230 [59] using the A14 tune [60] and the NNPDF2.3LO [58] PDF set.

The uncertainty due to initial-state radiation (ISR) was estimated by comparing the nominal  $tZq$  sample with two additional samples, which had the same settings as the nominal one, but employed the Var3c up and down variations of the A14 tune.

### Background samples

#### $t\bar{t}$

The production of  $t\bar{t}$  events was modelled using the POWHEGBox v2 [61–64] generator at NLO with the NNPDF3.0NLO [58] PDF set and the  $h_{damp}$  parameter<sup>1</sup> set to 1.5  $m_t$  [65]. The events were interfaced to PYTHIA8.320 [59] to model the parton shower, hadronisation, and underlying event, with parameters set according to the A14 tune [60] and using the NNPDF2.3LO set of PDFs [66]. The decays of bottom and charm hadrons were performed by EVTGEN v 1.6.0 [67].

#### $tW$

The associated production of top quarks with  $W$  bosons ( $tW$ ) was modelled by the POWHEGBox v2 [62–64, 68] generator at NLO in QCD using the five-flavour scheme

---

<sup>1</sup>The  $h_{damp}$  parameter is a resummation damping factor and one of the parameters that controls the matching of POWHEG matrix elements to the parton shower and thus effectively regulates the high- $p_T$  radiation against which the  $t\bar{t}$  system recoils.

and the NNPDF3.0NLO set of PDFs [58]. The diagram removal scheme [69] was used to remove interference and overlap with  $t\bar{t}$  production. The related uncertainty was estimated by comparison with an alternative sample generated using the diagram subtraction scheme [65, 69]. The events were interfaced to PYTHIA8.230 [59] using the A14 tune [60] and the NNPDF2.3LO set of PDFs [66].

### $t\bar{t}H$

The production of  $t\bar{t}H$  events was modelled using the POWHEGBOX v2 [61–64, 70] generator at NLO with the NNPDF3.0NLO [58] PDF set. The events were interfaced to PYTHIA8.230 [59] using the A14 tune [60] and the NNPDF2.3LO [58] PDF set. The decays of bottom and charm hadrons were performed by EVTGEN1.6.0 [67].

### $t\bar{t}W$ and $t\bar{t}Z$

The production of  $t\bar{t}W$  and  $t\bar{t}Z$  events was modelled using the MADGRAPH5\_AMC@NLO v2.3.3 [57] generator at NLO with the NNPDF3.0NLO [58] parton distribution function (PDF). The events were interfaced to PYTHIA8.210 [59] using the A14 tune [60] and the NNPDF2.3LO [58] PDF set. The decays of bottom and charm hadrons were simulated using the EVTGEN1.2.0 program [67].

The uncertainty due to initial-state radiation (ISR) was estimated by comparing the nominal event sample with two samples where the Var3c up/down variations of the A14 tune were employed.

### $tWZ$

The production of  $tWZ$  events was modelled using the MADGRAPH5\_AMC@NLO v2.3.3 [57] generator at NLO with the NNPDF3.0NLO [58] parton distribution function (PDF). The events were interfaced with PYTHIA8.212 [59] using the A14 tune [60] and the NNPDF2.3LO [58] PDF set. The decays of bottom and charm hadrons were simulated using the EVTGEN1.2.0 program [67].

### $Z+jets$

The production of  $V+jets$  was simulated with the SHERPA v2.2.1 [71] generator using next-to-leading-order (NLO) matrix elements (ME) for up to two partons, and leading-order (LO) matrix elements for up to four partons calculated with the Comix [72] and OPENLOOPS [73–75] libraries. They were matched with the SHERPA parton shower [76] using the MEPS@NLO prescription [77–80] using the set of tuned parameters developed by the SHERPA authors. The NNPDF3.0NNLO set of PDFs [58] was used and the samples were normalised to a next-to-next-to-leading-order (NNLO) prediction [81].

## Diboson

Samples of diboson final states ( $VV$ ) were simulated with the SHERPA v 2.2.1 (for 363356 and 363358) or v 2.2.2 (for 364250, 53-54) [71], including off-shell effects and Higgs boson contributions, where appropriate. Fully leptonic final states and semileptonic final states, where one boson decays leptonically and the other hadronically, were generated using matrix elements at NLO accuracy in QCD for up to one additional parton and at LO accuracy for up to three additional parton emissions. Samples for the loop-induced processes  $gg \rightarrow VV$  were generated using LO-accurate matrix elements for up to one additional parton emission for both the cases of fully leptonic and semileptonic final states. The matrix element calculations were matched and merged with the SHERPA parton shower based on Catani–Seymour dipole factorisation [72, 76] using the MEPS@NLO prescription [77–80]. The virtual QCD corrections were provided by the OPENLOOPS library [73–75]. The NNPDF3.0NNLO set of PDFs was used [58], along with the dedicated set of tuned parton-shower parameters developed by the SHERPA authors.

## Electroweak $VVjj$

Electroweak production of a diboson in association with two jets ( $VVjj$ ) was simulated with the SHERPA v2.2.2 [71] generator. The LO-accurate matrix elements were matched to a parton shower based on Catani–Seymour dipole factorisation [72, 76] using the MEPS@LO prescription [77–80]. Samples were generated using the NNPDF3.0NNLO PDF set [58], along with the dedicated set of tuned parton-shower parameters developed by the SHERPA authors.

## Triboson

The production of triboson ( $VVV$ ) events was simulated with the SHERPA v2.2.2 [71] generator using factorised gauge-boson decays. Matrix elements, accurate to NLO for the inclusive process and to LO for up to two additional parton emissions, were matched and merged with the SHERPA parton shower based on Catani–Seymour dipole factorisation [72, 76] using the MEPS@NLO prescription [77–80]. The virtual QCD corrections for matrix elements at NLO accuracy were provided by the OPENLOOPS library [73–75]. Samples were generated using the NNPDF3.0NNLO PDF set [58], along with the dedicated set of tuned parton-shower parameters developed by the SHERPA authors.



# Bibliography

- [1] P.A. Zyla et al. “Particle Data Group”. In: *Progress of Theoretical and Experimental Physics* 2020.8 (2020). 083C01. ISSN: 2050-3911. URL: <https://doi.org/10.1093/ptep/ptaa104>.
- [2] Peter W. Higgs. “Spontaneous Symmetry Breakdown without Massless Bosons”. In: *Phys. Rev.* 145 (4 1966), pp. 1156–1163. DOI: [10.1103/PhysRev.145.1156](https://doi.org/10.1103/PhysRev.145.1156). URL: <https://link.aps.org/doi/10.1103/PhysRev.145.1156>.
- [3] ATLAS Collaboration. “Observation of a new particle in the search for the Standard Model Higgs boson with the ATLAS detector at the LHC”. In: *Phys. Lett. B* 716 (2012), p. 1. DOI: [10.1016/j.physletb.2012.08.020](https://doi.org/10.1016/j.physletb.2012.08.020). arXiv: [1207.7214 \[hep-ex\]](https://arxiv.org/abs/1207.7214).
- [4] CMS Collaboration. “Observation of a new boson at a mass of 125 GeV with the CMS experiment at the LHC”. In: *Phys. Lett. B* 716 (2012), p. 30. DOI: [10.1016/j.physletb.2012.08.021](https://doi.org/10.1016/j.physletb.2012.08.021). arXiv: [1207.7235 \[hep-ex\]](https://arxiv.org/abs/1207.7235).
- [5] C. S. Wu et al. “Experimental Test of Parity Conservation in Beta Decay”. In: *Phys. Rev.* 105 (4 1957), pp. 1413–1415. DOI: [10.1103/PhysRev.105.1413](https://doi.org/10.1103/PhysRev.105.1413). URL: <https://link.aps.org/doi/10.1103/PhysRev.105.1413>.
- [6] A. Pich. “CP violation”. In: *ICTP Ser. Theor. Phys.* 10 (1994). Ed. by E. Gava et al., pp. 14–42. arXiv: [hep-ph/9312297](https://arxiv.org/abs/hep-ph/9312297).
- [7] Tim Gershon. “Overview of the Cabibbo–Kobayashi–Maskawa matrix”. In: *Pramana* 79.5 (2012), 1091–1108. ISSN: 0973-7111. DOI: [10.1007/s12043-012-0418-y](https://doi.org/10.1007/s12043-012-0418-y). URL: <http://dx.doi.org/10.1007/s12043-012-0418-y>.
- [8] Lincoln Wolfenstein. “Parametrization of the Kobayashi–Maskawa Matrix”. In: *Physical Review Letters* 51.21 (Nov. 1983), pp. 1945–1947. DOI: [10.1103/PhysRevLett.51.1945](https://doi.org/10.1103/PhysRevLett.51.1945).
- [9] Sigeo Hanawa. “Mathematical Formulation of the Gell-Mann-Nishijima Scheme for New Particles”. In: *Progress of Theoretical Physics* 17.4 (Apr. 1957), pp. 592–602. ISSN: 0033-068X. DOI: [10.1143/PTP.17.592](https://doi.org/10.1143/PTP.17.592). URL: <https://doi.org/10.1143/PTP.17.592>.

- [10] A J Macfarlane. “Dirac matrices and the Dirac matrix description of Lorentz transformations”. In: *Communications in Mathematical Physics (West Germany)* (). DOI: [10.1007/BF01773348](https://doi.org/10.1007/BF01773348). URL: <https://www.osti.gov/biblio/4537172>.
- [11] T M Yan. “The Parton Model”. In: *Annual Review of Nuclear Science* 26.1 (1976), pp. 199–238. DOI: [10.1146/annurev.ns.26.120176.001215](https://doi.org/10.1146/annurev.ns.26.120176.001215). eprint: <https://doi.org/10.1146/annurev.ns.26.120176.001215>. URL: <https://doi.org/10.1146/annurev.ns.26.120176.001215>.
- [12] Richard E. Taylor. “Inelastic electron - proton scattering in the deep continuum region”. In: *Conf. Proc. C* 690914 (1969), pp. 251–260. URL: <https://inspirehep.net/literature/54790>.
- [13] Richard P. Feynman. “The Behavior of Hadron Collisions at Extreme Energies”. In: *Special Relativity and Quantum Theory: A Collection of Papers on the Poincaré Group*. Ed. by M. E. Noz and Y. S. Kim. Dordrecht: Springer Netherlands, 1988, pp. 289–304. ISBN: 978-94-009-3051-3. DOI: [10.1007/978-94-009-3051-3\\_25](https://doi.org/10.1007/978-94-009-3051-3_25). URL: [https://doi.org/10.1007/978-94-009-3051-3\\_25](https://doi.org/10.1007/978-94-009-3051-3_25).
- [14] A. D. Martin et al. “Parton distributions for the LHC”. In: *Eur. Phys. J. C* 63 (2009), p. 189. DOI: [10.1140/epjc/s10052-009-1072-5](https://doi.org/10.1140/epjc/s10052-009-1072-5). arXiv: [0901.0002 \[hep-ph\]](https://arxiv.org/abs/0901.0002).
- [15] Y. Fukuda et al. “Evidence for Oscillation of Atmospheric Neutrinos”. In: *Physical Review Letters* 81.8 (1998), 1562–1567. ISSN: 1079-7114. DOI: [10.1103/physrevlett.81.1562](https://doi.org/10.1103/physrevlett.81.1562). URL: <http://dx.doi.org/10.1103/PhysRevLett.81.1562>.
- [16] D0 Collaboration. “Observation of the Top Quark”. In: *Physical Review Letters* 74.14 (1995), 2632–2637. ISSN: 1079-7114. DOI: [10.1103/physrevlett.74.2632](https://doi.org/10.1103/physrevlett.74.2632). URL: <http://dx.doi.org/10.1103/PhysRevLett.74.2632>.
- [17] CDF Collaboration. “Observation of Top Quark Production in  $p\bar{p}$  Collisions with the Collider Detector at Fermilab”. In: *Physical Review Letters* 74.14 (1995), 2626–2631. ISSN: 1079-7114. DOI: [10.1103/physrevlett.74.2626](https://doi.org/10.1103/physrevlett.74.2626). URL: <http://dx.doi.org/10.1103/PhysRevLett.74.2626>.
- [18] J.E. Augustin et al. “Discovery of a Narrow Resonance in  $e^+e^-$  Annihilation”. In: *Phys. Rev. Lett.* 33 (23 1974), pp. 1406–1408. DOI: [10.1103/PhysRevLett.33.1406](https://doi.org/10.1103/PhysRevLett.33.1406). URL: <https://link.aps.org/doi/10.1103/PhysRevLett.33.1406>.
- [19] Burton Richter. “From the Psi to Charm: The Experiments of 1975 and 1976”. In: *Rev. Mod. Phys.; (United States)* 196 (July 1977), pp. 1286–97. DOI: [10.1103/RevModPhys.49.251](https://doi.org/10.1103/RevModPhys.49.251). URL: <https://www.osti.gov/biblio/7216428>.
- [20] J. J. Aubert et al. “Experimental Observation of a Heavy Particle  $J$ ”. In: *Phys. Rev. Lett.* 33 (1974), pp. 1404–1406. DOI: [10.1103/PhysRevLett.33.1404](https://doi.org/10.1103/PhysRevLett.33.1404). URL: <https://inspirehep.net/literature/90773>.

- [21] S. W. Herb et al. “Observation of a Dimuon Resonance at 9.5-GeV in 400-GeV Proton-Nucleus Collisions”. In: *Phys. Rev. Lett.* 39 (1977), pp. 252–255. DOI: [10.1103/PhysRevLett.39.252](https://doi.org/10.1103/PhysRevLett.39.252). URL: <https://journals.aps.org/prl/abstract/10.1103/PhysRevLett.39.252>.
- [22] Leon M. Lederman. “The Upsilon Particle”. In: *Scientific American* 239.4 (1978), pp. 72–84. ISSN: 00368733, 19467087. URL: <http://www.jstor.org/stable/24955824>.
- [23] G Lüders. “On the equivalence of invariance under time reversal and under particle-antiparticle conjugation for relativistic field theories”. In: *Dan. Mat. Fys. Medd.* 28 (1954), pp. 1–17. URL: <http://cds.cern.ch/record/1071765>.
- [24] [https://twiki.cern.ch/twiki/pub/LHCPhysics/TopPairCrossSectionSqrtsHistory/tt\\_curve\\_toplhcgw\\_may21.pdf](https://twiki.cern.ch/twiki/pub/LHCPhysics/TopPairCrossSectionSqrtsHistory/tt_curve_toplhcgw_may21.pdf).
- [25] LHC Top Working Group. *NNLO+NNLL top-quark-pair cross sections*. <https://twiki.cern.ch/twiki/bin/view/LHCPhysics/TtbarNNLO>.
- [26] LHC Top Working Group. *NLO single-top channel cross sections*. <https://twiki.cern.ch/twiki/bin/view/LHCPhysics/SingleTopRefXsec>.
- [27] ATLAS collaboration. “Measurements of the inclusive and differential production cross sections of a top-quark-antiquark pair in association with a  $Z$  boson at  $\sqrt{s} = 13$  TeV with the ATLAS detector”. In: *arXiv preprint arXiv:2103.12603* (2021).
- [28] Olga Bessidskaia Bylund. *Modelling  $Wt$  and  $tWZ$  production at NLO for ATLAS analyses*. 2016. arXiv: [1612.00440 \[hep-ph\]](https://arxiv.org/abs/1612.00440).
- [29] ATLAS Collaboration. “Observation of the associated production of a top quark and a  $Z$  boson in  $pp$  collisions at  $\sqrt{s} = 13$  TeV with the ATLAS detector”. In: *JHEP* 07 (2020), p. 124. DOI: [10.1007/JHEP07\(2020\)124](https://doi.org/10.1007/JHEP07(2020)124). arXiv: [2002.07546 \[hep-ex\]](https://arxiv.org/abs/2002.07546).
- [30] Lyndon R Evans and Philip Bryant. “LHC Machine”. In: *JINST* 3 (2008), S08001. 164 p. DOI: [10.1088/1748-0221/3/08/S08001](https://doi.org/10.1088/1748-0221/3/08/S08001). URL: <http://cds.cern.ch/record/1129806>.
- [31] ATLAS Collaboration. “The ATLAS Experiment at the CERN Large Hadron Collider”. In: *JINST* 3 (2008), S08003. DOI: [10.1088/1748-0221/3/08/S08003](https://doi.org/10.1088/1748-0221/3/08/S08003).
- [32] CMS Collaboration. “The CMS experiment at the CERN LHC”. In: *JINST* 3 (2008), S08004. DOI: [10.1088/1748-0221/3/08/S08004](https://doi.org/10.1088/1748-0221/3/08/S08004).
- [33] ALICE Collaboration. “The ALICE experiment at the CERN LHC”. In: *JINST* 3.08 (2008), S08002–S08002. DOI: [10.1088/1748-0221/3/08/S08002](https://doi.org/10.1088/1748-0221/3/08/S08002). URL: <https://doi.org/10.1088/1748-0221/3/08/S08002>.
- [34] LHCb Collaboration. “The LHCb Detector at the LHC”. In: *JINST* 3.08 (2008), S08005–S08005. DOI: [10.1088/1748-0221/3/08/S08005](https://doi.org/10.1088/1748-0221/3/08/S08005). URL: <https://doi.org/10.1088/1748-0221/3/08/S08005>.

- [35] J. T. Boyd. *LHC Run-2 and Future Prospects*. 2020. arXiv: [2001.04370 \[hep-ex\]](https://arxiv.org/abs/2001.04370).
- [36] <https://home.cern/resources/faqs/facts-and-figures-about-lhc>.
- [37] *LuminosityPublicResultsRun2*. <https://twiki.cern.ch/twiki/bin/view/AtlasPublic/LuminosityPublicResultsRun2>.
- [38] <https://atlas.cern/discover/detector>.
- [39] Joao Pequenao and Paul Schaffner. “How ATLAS detects particles: diagram of particle paths in the detector”. 2013. URL: <https://cds.cern.ch/record/1505342>.
- [40] G. Avoni et al. “The new LUCID-2 detector for luminosity measurement and monitoring in ATLAS”. In: *JINST* 13.07 (2018), P07017–P07017. DOI: [10.1088/1748-0221/13/07/p07017](https://doi.org/10.1088/1748-0221/13/07/p07017). URL: <https://doi.org/10.1088/1748-0221/13/07/p07017>.
- [41] ATLAS Collaboration. “Performance of the ATLAS trigger system in 2015”. In: *Eur. Phys. J. C* 77 (2017), p. 317. DOI: [10.1140/epjc/s10052-017-4852-3](https://doi.org/10.1140/epjc/s10052-017-4852-3). arXiv: [1611.09661 \[hep-ex\]](https://arxiv.org/abs/1611.09661).
- [42] ATLAS Collaboration. *Trigger Menu in 2016*. ATL-DAQ-PUB-2017-001. 2017. URL: <https://cds.cern.ch/record/2242069>.
- [43] ATLAS Collaboration. *Performance of the ATLAS global transverse-momentum triggers at  $\sqrt{s} = 8$  TeV*. ATL-DAQ-PUB-2018-001. 2018. URL: <https://cds.cern.ch/record/2311730>.
- [44] ATLAS Collaboration. *Trigger Menu in 2018*. ATL-DAQ-PUB-2019-001. 2019. URL: <https://cds.cern.ch/record/2693402>.
- [45] ATLAS Collaboration. *Vertex Reconstruction Performance of the ATLAS Detector at  $\sqrt{s} = 13$  TeV*. ATL-PHYS-PUB-2015-026. 2015. URL: <https://cds.cern.ch/record/2037717>.
- [46] ATLAS Collaboration. *Electron identification measurements in ATLAS using  $\sqrt{s} = 13$  TeV data with 50 ns bunch spacing*. ATL-PHYS-PUB-2015-041. 2015. URL: <https://cds.cern.ch/record/2048202>.
- [47] ATLAS Collaboration. “Electron reconstruction and identification in the ATLAS experiment using the 2015 and 2016 LHC proton–proton collision data at  $\sqrt{s} = 13$  TeV”. In: *The European Physical Journal C* 79.8 (2019). ISSN: 1434-6052. DOI: [10.1140/epjc/s10052-019-7140-6](https://doi.org/10.1140/epjc/s10052-019-7140-6). URL: <http://dx.doi.org/10.1140/epjc/s10052-019-7140-6>.
- [48] ATLAS Collaboration. *Electron efficiency measurements with the ATLAS detector using the 2015 LHC proton–proton collision data*. ATLAS-CONF-2016-024. 2016. URL: <https://cds.cern.ch/record/2157687>.
- [49] ATLAS Collaboration. *Muon reconstruction performance in early  $\sqrt{s} = 13$  TeV data*. ATL-PHYS-PUB-2015-037. 2015. URL: <https://cds.cern.ch/record/2047831>.

- [50] Matteo Cacciari, Gavin P Salam, and Gregory Soyez. “The anti-ktjet clustering algorithm”. In: *Journal of High Energy Physics* 2008.04 (2008), 063–063. ISSN: 1029-8479. DOI: [10.1088/1126-6708/2008/04/063](https://doi.org/10.1088/1126-6708/2008/04/063). URL: <http://dx.doi.org/10.1088/1126-6708/2008/04/063>.
- [51] ATLAS Collaboration. *Optimisation of the ATLAS b-tagging performance for the 2016 LHC Run*. ATL-PHYS-PUB-2016-012. 2016. URL: <https://cds.cern.ch/record/2160731>.
- [52] ATLAS Collaboration. “ATLAS b-jet identification performance and efficiency measurement with  $t\bar{t}$  events in pp collisions at  $\sqrt{s} = 13$  TeV”. In: *The European Physical Journal C* 79.11 (2019). ISSN: 1434-6052. DOI: [10.1140/epjc/s10052-019-7450-8](https://doi.org/10.1140/epjc/s10052-019-7450-8). URL: <http://dx.doi.org/10.1140/epjc/s10052-019-7450-8>.
- [53] Glen Cowan. “Error analysis with weighted events”. In: (June 2014).
- [54] Fudong He. *PLIWP*. [https://gitlab.cern.ch/fuhe/plivwp/-/tree/master/plots/elec\\_endcap](https://gitlab.cern.ch/fuhe/plivwp/-/tree/master/plots/elec_endcap).
- [55] Fudong He. *PLIWP*. <https://gitlab.cern.ch/fuhe/plivwp/-/tree/master/plots/muon>.
- [56] ATLAS Collaboration. “Muon reconstruction and identification efficiency in ATLAS using the full Run 2  $pp$  collision data set at  $\sqrt{s} = 13$  TeV”. In: *Eur. Phys. J. C* 81.7 (2021), p. 578. DOI: [10.1140/epjc/s10052-021-09233-2](https://doi.org/10.1140/epjc/s10052-021-09233-2). arXiv: [2012.00578 \[hep-ex\]](https://arxiv.org/abs/2012.00578).
- [57] J. Alwall et al. “The automated computation of tree-level and next-to-leading order differential cross sections, and their matching to parton shower simulations”. In: *JHEP* 07 (2014), p. 079. DOI: [10.1007/JHEP07\(2014\)079](https://doi.org/10.1007/JHEP07(2014)079). arXiv: [1405.0301 \[hep-ph\]](https://arxiv.org/abs/1405.0301).
- [58] Richard D. Ball et al. “Parton distributions for the LHC run II”. In: *JHEP* 04 (2015), p. 040. DOI: [10.1007/JHEP04\(2015\)040](https://doi.org/10.1007/JHEP04(2015)040). arXiv: [1410.8849 \[hep-ph\]](https://arxiv.org/abs/1410.8849).
- [59] Torbjörn Sjöstrand et al. “An introduction to PYTHIA 8.2”. In: *Comput. Phys. Commun.* 191 (2015), p. 159. DOI: [10.1016/j.cpc.2015.01.024](https://doi.org/10.1016/j.cpc.2015.01.024). arXiv: [1410.3012 \[hep-ph\]](https://arxiv.org/abs/1410.3012).
- [60] ATLAS Collaboration. *ATLAS Pythia 8 tunes to 7 TeV data*. ATL-PHYS-PUB-2014-021. 2014. URL: <https://cds.cern.ch/record/1966419>.
- [61] Stefano Frixione, Paolo Nason, and Giovanni Ridolfi. “A positive-weight next-to-leading-order Monte Carlo for heavy flavour hadroproduction”. In: *JHEP* 09 (2007), p. 126. DOI: [10.1088/1126-6708/2007/09/126](https://doi.org/10.1088/1126-6708/2007/09/126). arXiv: [0707.3088 \[hep-ph\]](https://arxiv.org/abs/0707.3088).
- [62] Paolo Nason. “A new method for combining NLO QCD with shower Monte Carlo algorithms”. In: *JHEP* 11 (2004), p. 040. DOI: [10.1088/1126-6708/2004/11/040](https://doi.org/10.1088/1126-6708/2004/11/040). arXiv: [hep-ph/0409146](https://arxiv.org/abs/hep-ph/0409146).

- [63] Stefano Frixione, Paolo Nason, and Carlo Oleari. “Matching NLO QCD computations with parton shower simulations: the POWHEG method”. In: *JHEP* 11 (2007), p. 070. doi: [10.1088/1126-6708/2007/11/070](https://doi.org/10.1088/1126-6708/2007/11/070). arXiv: [0709.2092 \[hep-ph\]](https://arxiv.org/abs/0709.2092).
- [64] Simone Alioli et al. “A general framework for implementing NLO calculations in shower Monte Carlo programs: the POWHEG BOX”. In: *JHEP* 06 (2010), p. 043. doi: [10.1007/JHEP06\(2010\)043](https://doi.org/10.1007/JHEP06(2010)043). arXiv: [1002.2581 \[hep-ph\]](https://arxiv.org/abs/1002.2581).
- [65] ATLAS Collaboration. *Studies on top-quark Monte Carlo modelling for Top2016*. ATL-PHYS-PUB-2016-020. 2016. URL: <https://cds.cern.ch/record/2216168>.
- [66] Richard D. Ball et al. “Parton distributions with LHC data”. In: *Nucl. Phys. B* 867 (2013), p. 244. doi: [10.1016/j.nuclphysb.2012.10.003](https://doi.org/10.1016/j.nuclphysb.2012.10.003). arXiv: [1207.1303 \[hep-ph\]](https://arxiv.org/abs/1207.1303).
- [67] D. J. Lange. “The EvtGen particle decay simulation package”. In: *Nucl. Instrum. Meth. A* 462 (2001), p. 152. doi: [10.1016/S0168-9002\(01\)00089-4](https://doi.org/10.1016/S0168-9002(01)00089-4).
- [68] Emanuele Re. “Single-top  $Wt$ -channel production matched with parton showers using the POWHEG method”. In: *Eur. Phys. J. C* 71 (2011), p. 1547. doi: [10.1140/epjc/s10052-011-1547-z](https://doi.org/10.1140/epjc/s10052-011-1547-z). arXiv: [1009.2450 \[hep-ph\]](https://arxiv.org/abs/1009.2450).
- [69] Stefano Frixione et al. “Single-top hadroproduction in association with a  $W$  boson”. In: *JHEP* 07 (2008), p. 029. doi: [10.1088/1126-6708/2008/07/029](https://doi.org/10.1088/1126-6708/2008/07/029). arXiv: [0805.3067 \[hep-ph\]](https://arxiv.org/abs/0805.3067).
- [70] Heribertus B. Hartanto et al. “Higgs boson production in association with top quarks in the POWHEG BOX”. In: *Phys. Rev. D* 91.9 (2015), p. 094003. doi: [10.1103/PhysRevD.91.094003](https://doi.org/10.1103/PhysRevD.91.094003). arXiv: [1501.04498 \[hep-ph\]](https://arxiv.org/abs/1501.04498).
- [71] Enrico Bothmann et al. “Event generation with Sherpa 2.2”. In: *SciPost Phys.* 7.3 (2019), p. 034. doi: [10.21468/SciPostPhys.7.3.034](https://doi.org/10.21468/SciPostPhys.7.3.034). arXiv: [1905.09127 \[hep-ph\]](https://arxiv.org/abs/1905.09127).
- [72] Tanju Gleisberg and Stefan Höche. “Comix, a new matrix element generator”. In: *JHEP* 12 (2008), p. 039. doi: [10.1088/1126-6708/2008/12/039](https://doi.org/10.1088/1126-6708/2008/12/039). arXiv: [0808.3674 \[hep-ph\]](https://arxiv.org/abs/0808.3674).
- [73] Federico Buccioni et al. “OpenLoops 2”. In: *Eur. Phys. J. C* 79.10 (2019), p. 866. doi: [10.1140/epjc/s10052-019-7306-2](https://doi.org/10.1140/epjc/s10052-019-7306-2). arXiv: [1907.13071 \[hep-ph\]](https://arxiv.org/abs/1907.13071).
- [74] Fabio Cascioli, Philipp Maierhöfer, and Stefano Pozzorini. “Scattering Amplitudes with Open Loops”. In: *Phys. Rev. Lett.* 108 (2012), p. 111601. doi: [10.1103/PhysRevLett.108.111601](https://doi.org/10.1103/PhysRevLett.108.111601). arXiv: [1111.5206 \[hep-ph\]](https://arxiv.org/abs/1111.5206).
- [75] Ansgar Denner, Stefan Dittmaier, and Lars Hofer. “COLLIER: A fortran-based complex one-loop library in extended regularizations”. In: *Comput. Phys. Commun.* 212 (2017), pp. 220–238. doi: [10.1016/j.cpc.2016.10.013](https://doi.org/10.1016/j.cpc.2016.10.013). arXiv: [1604.06792 \[hep-ph\]](https://arxiv.org/abs/1604.06792).

- [76] Steffen Schumann and Frank Krauss. “A parton shower algorithm based on Catani–Seymour dipole factorisation”. In: *JHEP* 03 (2008), p. 038. doi: [10.1088/1126-6708/2008/03/038](https://doi.org/10.1088/1126-6708/2008/03/038). arXiv: [0709.1027 \[hep-ph\]](https://arxiv.org/abs/0709.1027).
- [77] Stefan Höche et al. “A critical appraisal of NLO+PS matching methods”. In: *JHEP* 09 (2012), p. 049. doi: [10.1007/JHEP09\(2012\)049](https://doi.org/10.1007/JHEP09(2012)049). arXiv: [1111.1220 \[hep-ph\]](https://arxiv.org/abs/1111.1220).
- [78] Stefan Höche et al. “QCD matrix elements + parton showers. The NLO case”. In: *JHEP* 04 (2013), p. 027. doi: [10.1007/JHEP04\(2013\)027](https://doi.org/10.1007/JHEP04(2013)027). arXiv: [1207.5030 \[hep-ph\]](https://arxiv.org/abs/1207.5030).
- [79] S. Catani et al. “QCD Matrix Elements + Parton Showers”. In: *JHEP* 11 (2001), p. 063. doi: [10.1088/1126-6708/2001/11/063](https://doi.org/10.1088/1126-6708/2001/11/063). arXiv: [hep-ph/0109231](https://arxiv.org/abs/hep-ph/0109231).
- [80] Stefan Höche et al. “QCD matrix elements and truncated showers”. In: *JHEP* 05 (2009), p. 053. doi: [10.1088/1126-6708/2009/05/053](https://doi.org/10.1088/1126-6708/2009/05/053). arXiv: [0903.1219 \[hep-ph\]](https://arxiv.org/abs/0903.1219).
- [81] Charalampos Anastasiou et al. “High precision QCD at hadron colliders: Electroweak gauge boson rapidity distributions at next-to-next-to leading order”. In: *Phys. Rev. D* 69 (2004), p. 094008. doi: [10.1103/PhysRevD.69.094008](https://doi.org/10.1103/PhysRevD.69.094008). arXiv: [hep-ph/0312266](https://arxiv.org/abs/hep-ph/0312266).